Structure-guided vaccine, antibody and drug discovery

Zhaoqian Wang

A dissertation

submitted in partial fulfillment of the

requirements for the degree of

Doctor of Philosophy

University of Washington

2022

Reading Committee:

David Veesler, Chair

Charles Asbury

Neil King

Program Authorized to Offer Degree:

Biochemistry

University of Washington

Abstract

Structure-guided vaccine, antibody and drug discovery

Zhaoqian Wang

Chair of the Supervisory Committee:

David Veesler

Department of Biochemistry

The current pandemic, COVID19, will remain engraved in our history. However, if not the rapid response for vaccine and antibody development has been made from the outset, this wound might be even deeper and more anguished. Advances in mRNA vaccine delivery and pre-fusion spike stabilization were the cornerstones of this success. And this footstone cannot be made without the structure information we gathered in the past several years. Here, I will show how important and necessary the structure information is for facilitating and even initiating vaccine, antibody and drug development. To illustrate this argument, I am going to cover several examples across coronavirus, henipavirus and orthopoxvirus structure studies using CryoEM and CryoET

techniques complemented with biochemical and biophysical assays, such as ELISA, BLI and pseudovirus neutralization. The results from these studies are great examples of how structure information can reshape our understanding of diverse biological systems. And for the virology field, these new understandings are so valuable for potential pandemic preparation. If the disaster reemerges, we will never be more prepared by that time.

TABLE OF CONTENTS

LIST OF FIGURES

ACKNOWLEDGEMENT

Chapter 1. INTRODUCTION 1

1.1 Coronavirus 2
1.2 Henipavirus 3
1.3 Orthopoxvirus 5
1.4 Single particle Cryo-EM 6
1.5 Cryo-ET 7
1.6 Subtomogram average 8

Chapter 2. Structures of MERS-CoV spike glyco- protein in complex with sialoside attachment receptors 10

2.1 Background 10
2.2 A sialoside-binding site in the MERS-CoV S glycoprotein 14
2.3 The sialoside binding site is required for S-mediated viral attachment and entry 16
2.4 Discussion 17
2.5 Figures & Tables 20

Chapter 3. Architecture and antigenicity of the Nipah virus attachment glycoprotein 28

3.1 Abstract 28
3.2 Architecture of the NiV G tetramer 29
3.3 nAH1.3-mediated broad neutralization of NiV and HeV 31
3.4 Synergistic neutralization of NiV and HeV by a mAb cocktail 33
3.5 The NiV G head domain is the main target of vaccine-elicited serum neutralization 35
3.6 Discussion 36
3.7 Figures & Tables 38

Chapter 4. Potent monoclonal antibody–mediated neutralization of a divergent Hendra virus variant 57

4.1 Background 57
4.2 HeV-g2 and HeV Share a Conserved Receptor Tropism 58
4.3 Broadly Neutralizing HNV G-Specific mAbs Inhibit HeV-g2 60
4.4 The hAH1.3 Neutralizing mAb Defines a HeV/HeV-g2 G Antigenic Site 61
4.5 Structure-Guided Formulation of a Tetravalent mAb Mixture 62
4.6 Discussion 63
4.7 Figures & Tables 65

Chapter 5. Core wall structure and organization of Vaccinia virus **80**
5.1 Background 80
5.2 Architecture and organization of Vaccinia MV 82
5.3 Structure determination of Vaccinia outer core wall layer 83
5.4 Discussion 84
5.5 Figures & Tables 86

Chapter 6. Ultrastructure of Cedar virus nucleoprotein **90**
6.1 Background 90
6.2 In situ ultrastructure and morphology of Cedar virus 91
6.3 Structure and organization of Cedar virus nucleoprotein 92
6.4 Discussion 92
6.5 Figures & Tables 94

Chapter 7. Conclusion and future directions **97**

Reference **100**

LIST OF FIGURES

Chapter 2

Figure 2.1 Cryo-EM identification of a sialoside-binding site in the MERS-CoV S glycoprotein. 20

Figure 2.2 CryoEM analysis of the MERS-CoV S glycoprotein in complex with Neu5Ac at 2.7 Å resolution. 22

Figure 2.3 MERS-CoV S and HCoV-OC43 S glycoproteins interact with sialosides, using distinct binding grooves. 23

Figure 2.4 The ligand-binding site is required for MERS-CoV S-mediated attachment to sialosides and entry into human airway epithelial cells. 25

Figure 2.5 SDS-PAGE and Western blot analyses. 27

Chapter 3

Figure 3.2 Architecture of the NiV G homotetramer. 41

Figure 3.3 Comparison of NiV G and other paramyxovirus attachment glycoproteins. 43

Figure 3.4 Characterization of the inhibitory and biophysical properties of the nAH1.3 mAb. 44

Figure 3.5 Structural basis for nAH1.3-mediated broad neutralization of NiV and HeV. 46

Figure 3.6 Deep-sequencing of chimeric rCedV-NiV-B-GFP and rCedV-HeV-GFP reveals G protein mutations that permit escape from nAH1.3 or m102.4 mAbs. 48

Figure 3.7 A HNV G head-directed mAb cocktail with synergistic neutralizing activity. 50

Figure 3.8 EM characterization of the NiVG/m102.4/nAH1.3 complex and polyclonal epitope mapping. 52

Figure 3.9 Evaluation of neutralization synergy and depletion study. 54

Figure 3.10 The NiV G receptor binding head domain is immunodominant and accounts for most of the neutralizing activity elicited by vaccination. 55

Chapter 4

Figure 4.1 Sequence conservation between HeV and HeV-g2 G and F glycoproteins. 65

Figure 4.2 HeV and HeV-g2 share a conserved receptor tropism. 66

Figure 4.3 Biolayer interferometry evaluation of receptor binding. 67

Figure 4.4 Assessment of ephrin receptor tropism. 69

Figure 4.5 Broadly neutralizing HNV G-specific mAbs inhibit HeV-g2. 70

Figure 4.6 Enzyme-linked immunosorbent assays of G-directed mAb binding. 72

Figure 4.7 hAH1.3 cross-reacts with and neutralizes HeV and HeV-g2. 73

Figure 4.8 Competition biolayer interferometry analysis of binding of the hAH1.3 Fab and EB2 to the immobilized HeV G head domain. 75

Figure 4.9 Close-up view of the hAH1.3 epitope and representative electron density. 76

Figure 4.10 G-targeted tetravalent mAb mixture and vaccine-elicited antibodies broadly neutralize HeV-g2. 78

Chapter 5

Figure 5.1 Architecture and organization of Vaccinia MV revealed by Cryo-ET 86

Figure 5.2 Molecular detail of Vaccinia MV core wall determined by subtomogram average 88

Figure 5.3 Structure prediction of key core wall proteins 89

Chapter 6

Figure 6.1 Architecture and organization of Cedar virus revealed by Cryo-ET 94

Figure 6.2 Molecular detail of Cedar virus nucleoprotein determined by subtomogram average 96

ACKNOWLEDGEMENT

THANKS TO EVERYONE

WHO I MET AND ACQUAINTED

ON THE PATH OF MY LIFE

Chapter 1. INTRODUCTION

From the arising of structure biology, it helped diverse biological fields in various perspectives. Regardless of the approach considered, traditional crystallography, current cryo-electron microscopy (Cryo-EM) or newly emerged machine learning-based structure prediction, every technique has provided tremendous information and solved enormous biological problems. In the last two decades, the development and progression speed of electron microscopy (EM) has been stunning. The number of volume maps obtained using cryoEM is growing exponentially, and the highest resolution map generated by single particle Cryo-EM has almost caught up with X-ray crystallography. Among all the improvements, the most remarkable one has to be the time usage for solving one structure, which has been reduced from years to only weeks. One great example of this will be SARS-CoV2 spike protein, where two groups solved this structure independently only a few weeks after the release of the viral genome sequence. This is a mark that single particle Cryo-EM has become a streamlined and practical tool used daily by a wide researcher community. Such “efficiency revolution” not just happened to single particle Cryo-EM, but is also currently ongoing in the cryo-tomography (Cryo-ET) field. The data collection speed has been improved from hours per tomograph to tens of minutes. The data processing time took years less than a decade ago, and only takes a month or two nowadays. The reduction of the application threshold of EM, not only accelerated our understanding of diverse biological systems, but also fundamentally changed our observation method to these

systems, which allow us to receive the information that we simply cannot achieve using traditional observation techniques.

Here, I will cover five short stories across MERS coronavirus spike protein, Nipah Virus attachment protein, Hendra Virus attachment protein receptor binding domain, Vaccinia virus and Cedar virus which I studied using single particle Cryo-EM, Cryo-ET and subtomogram average techniques. Before we dive into structure biology, let's have some background information about all these different viruses and techniques.

1.1 Coronavirus

Due to the current pandemic, coronavirus (CoV) might become the most famous or infamous virus to almost everyone. But this is not the first time that coronavirus damages human society. Just in the last two decades, both severe acute respiratory syndrome coronavirus (SARS-CoV) (*1*, *2*) and Middle-East respiratory syndrome coronavirus (*3*) (MERS-CoV) spilled over and caused deadly pneumonia in humans, where SARS-CoV took more than 700 lifes and MERS-CoV caused at least 800 deaths.

Coronaviruses are enveloped RNA viruses composed of spike protein (S), membrane protein (M), envelope protein (E) and cytoplasmic nucleocapsid protein (N), where embecoviruses also contain hemagglutinin esterase (HE). Among all the CoV proteins, spike protein is the main transmembrane glycoprotein that is responsible for the immune response due to its involvement in the vira-host fusion process, the most important step for viral infection. S protein forms homotrimers protruding from the viral surface (*4*) that can be divided into two functional subunits, which are host cell receptor

binding related S_1 subunit and fusion related S_2 subunit. For many CoVs, protease cleavage between S_1 and S_2 is crucial for fusion event to happen, and the second cleavage within S_2 (S_2' site) is necessary for S protein to change conformation from pre-fusion state to post-fusion state, which allows the viral-host membrane merger to happen (*5*).

While S_2 is important for fusion, most of the antigenicity of S protein comes from S_1 subunit, since the receptor recognition is necessary for viral infection. Different CoVs utilize S_1 subunit differently. OC43 and HKU1 for example both use domain A (S^A) of S_1 subunit to interact with host cell surface acetylated sialosides to enable host entry, while MERS-CoV uses S^A to interact with non-acetylated sialosides as initial attachment process followed by entry receptor dipeptidyl-peptidase 4 (DPP4) interaction with domain B (S^B), and both SARS-CoV and SARS-CoV2 interact with host cell receptor angiotensin-converting enzyme 2 (ACE2) directly with S^B [*5–7*].

1.2 Henipavirus

Nipah virus (NiV) and Hendra virus (HeV) are bat-borne zoonotic pathogens of the Henipavirus (HNV) genus causing encephalitis and respiratory symptoms in humans, with fatality rates between 50 and 95%. Over the past two decades, NiV has spilled over into humans almost annually in Bangladesh (Bangladesh strain, NiV-B) and has also caused outbreaks in India (NiV-B) and the Philippines (Malaysia strain, NiV-M). The detection of cross-reactive HNV antibodies (Abs) in humans and Pteropus bats in Africa underscored that 2 billion people worldwide live in regions threatened by HNV spillovers. Moreover, the recent discovery of a previously unknown HeV genotype is an

urgent reminder of the HNV zoonotic threat. To date, no approved vaccines or therapeutics for use in people exist against HNV infections (*8*, *9*).

HNVs are enveloped RNA viruses whose entry into host cells requires fusion of the viral membrane and the host plasma membrane through the concerted action of an attachment (G) glycoprotein and a fusion (F) glycoprotein. The NiV and HeV entry receptors at the surface of host cells are the transmembrane protein tyrosine kinases ephrin-B2 or ephrin-B3. G and F have been proposed to undergo a cascade of conformational changes to promote membrane fusion upon receptor engagement. HNV G and F are the targets of the humoral immune response, and serum neutralizing Abs are a correlate of protection in animals experimentally infected with NiV or HeV. The cross-reactive NiV and HeV G-specific m102.4 monoclonal antibody (mAb) has been administered on an emergency compassionate use basis to 15 individuals with high-risk exposure to HeV or NiV infection and recently completed a phase 1 clinical trial in Australia (*8*–*10*).

A soluble HeV G tetrameric ectodomain immunogen (HeV sG) elicits high titers of cross-reactive neutralizing Abs and protects against both NiV and HeV challenge in preclinical studies (*11*–*17*). A vaccine using HeV sG is commercially available for use in horses in Australia (Equivac HeV, Zoetis Inc.), and a formulation suitable for human use has recently entered phase 1 clinical trials (NCT04199169). Although crystal structures of the isolated NiV and HeV G head domains were previously determined, no structural information is available for any HNV G tetramer, hindering both our understanding of immunity directed toward G and the rational design of improved vaccine candidates (*8*, *9*).

Besides these deadly HNV strains, this family also contains the bat-borne Cedar virus (CedV) and Ghanaian virus (GhV) together with more distantly related Mojiang virus (MojV), Langya virus (LayV), Gamak virus (GAKV) and Daeryong virus (DARV).

1.3 Orthopoxvirus

All the members of the orthopoxvirus family are enveloped single stranded DNA viruses with very large genomes that can be more than 170 kbp and encode over 200 polypeptides (*18*). Orthopoxviruses have a very sophisticated viral life cycle. Virus starts to assemble within cytoplasmic viral factories to form crescent-shaped membranes. The resulting membrane fragments then enclose granular material from the virosomes, and form the first step virion known as immature virions (IVs). The maturation continues and forms a soap bar like structure where the envelope surrounds a broad bean-shaped electron dense core structure (also called core wall) that contains viral DNA (*19*), named intracellular mature virions (IMV). From this point, the virus can either be directly released from the host cell as mature virions (MV), or sent to the trans-golgi to be wrapped by another layer of membrane and become enveloped virions (EV).

While both virion types are pathogenic, they have slightly different infection pathways. The EV will attach to the host cell receptor through the viral attachment complex (AC) on the outer envelope, and the dissolution of the envelope will happen after the docking process finishes, followed by the release of inner MV. On the other hand, the directly released MV will skip the attachment step and directly go through the fusion process through the entry fusion complex (EFC) (*20*). Though current studies have shown that both the AC and EFC are potent antigenic targets, the structure

information is limited on both complexes (*21*). Meanwhile, the structure and organization of the core wall also remains a mystery. Thus gathering structure information about AC, EFC and core wall will be beneficial for vaccine and drug development.

1.4 Single particle Cryo-EM

After the Nobel Prize was awarded to cryogenic electron microscopy (Cryo-EM) in 2017, this technique has come to light for a more broad biological audience as well as the public. However, Cryo-EM is actually not a “new” technique and can be traced back to the 1960-70s (*22*). Nevertheless, due to the radiation damage caused by the electron beam while lower beam intensity would lead to lower signal, this method had very limited usage at that time. This dilemma was resolved until the 1980s, when new cryogen, liquid propane and liquid ethane, were found to be able to create thin and vitrified ice, which, unlike the normal ice we find in our daily life, forms a solid water layer without a crystal packing (*23*, *24*). From then on, the Cryo-EM field spent almost 40 years on scope development, sample preparation improvement as well as data collection and analysis progress, and finally achieved what we called “resolution revolution”, which refers to the advance in structure resolution from worse than 40Å to atomic resolution (~1Å) (*25*). The number of protein structures solved by Cryo-EM is growing exponentially due to the bypassing of the need to grow crystals for X-ray crystallography. Also, together with the computational power progression as well as camera development in the last couple of years, the field is currently undergoing an “efficiency revolution”. That the structure determination has been reduced from years of work to only several months. Among all the examples, every SARS-CoV2 spike protein

structure that has been determined during the current pandemic could be the best instance.

Single particle Cryo-EM is currently the most commonly used approach in the Cryo-EM field. In single particle analysis, purified proteins or protein complexes are rapidly plunge-frozen into liquid ethane at -180˚C to yield vitreous ice, which preserves the samples' native state. Transmission electron microscopy (TEM) is then used to collect numerous 2D snapshots of the target proteins. As the proteins are suspended within the ice, they adopt random orientations. Thus these images show the sample at various angles, and can be recombined into a high-resolution 3D reconstruction of the sample through the process of so-called back projection. However, due to the intrinsically low signal to noise ratio of TEM, tens to hundreds of thousands of 2D snapshots are averaged together in order to boost the signal, thereby averaging out the noise. The resulting atomic 3D reconstructed electron volume map allows us to build detailed and accurate molecular models into it.

1.5 Cryo-ET

TEM tomography has traditionally been used for revealing cellular ultrastructural morphologies using plastic-embedded stained samples and to study changes in cells and tissues during disease. In the last decades, the breakthrough advances in microscopes, stages, direct electron detectors, energy filters, phase plates, and data processing software in combination with ongoing development of advanced sample preparation techniques of frozen hydrated cells and other specimens have been instrumental to allow for molecular-level views, some with near-atomic resolution, such

as the immature HIV-1 capsid (*26*, *27*). On the other hand, tomography is a commonly used technique that provides 3D information of an object and has been used in many biological fields. For instance, computed tomography (CT) and magnetic resonance imaging (MRI) used in medicine are all similar in concept to Cryo-ET, where a two dimensional set of rotational images is collected from a 3D object, thus the back projection of these 2D images is able to restore the original spatial information (*27*).

Due to the nature of the electron beam, where the mean free path is highly limited by sample thickness due to inelastic collision, Cryo-ET focuses on cell organelle and molecule level rather than full tissue or organ (*28*, *29*). In fact, at this moment Cryo-ET is the only method that can achieve subnanometer level resolution information of macromolecules at native, or so called in situ, environment. This information is so precious, since it bridges the gap between macromolecules' ultrastructural features to molecular level details.

1.6 Subtomogram average

In the same concept as single particle Cryo-EM, for subtomogram average, instead of using 2D snapshots as in single particle Cryo-EM, subvolumes from the tomogram that contains targeted macromolecules will be aligned and averaged together based on identity and similarity in order to boost the signal and reach higher resolution. Unlike the single particle approach, since the particles are already in 3D, no back projection is needed for subtomogram average. Nevertheless, because of the sample thickness, which can reach up to 500 nm, the signal to noise ratio is even worse. Thus, the averaging step is crucial for subtomogram average approach to reduce the noise

influence. Highly dependent on the number of copies of a molecule that can be defined, the resulting resolution of electron volume maps can range from ~30Å to near atomic resolution (~3Å).

Chapter 2. Structures of MERS-CoV spike glyco-protein in complex with sialoside attachment receptors

This chapter highlights the ability of single particle Cryo-EM on small molecule discovery. Just half a decade ago, no one would really connect Cryo-EM with small molecules due to the resolution limitation. This early 2019 work is an example that Cryo-EM already possesses the capability for small molecule screening in complex with target protein, and thus can be used for drug discovery. To illustrate this concept, here I describe a single particle Cryo-EM structure of MERS-CoV spike in complex with 309 Da Sialic acid, Neu5Ac, at 2.5Å local resolution.

On the biological side, this structure revealed the binding site of Sialic acid, which is involved in the initial viral attachment process of MERS-CoV, thus directly relates to viral infection and neutralization. This structure together with many other Sialic acid alternatives bond spike protein structures in the resulting paper, gives us the hints for potential viral attachment inhibitor drug design as well as indicates a very important neutralizing epitope for vaccine and antibody drug development.

2.1 Background

The Middle East respiratory syndrome coronavirus (MERS-CoV) was discovered in 2012 on the Arabian Peninsula as the causative agent of acute respiratory distress (and renal failure), with an unusually high fatality rate of ~35% (*3*). The vast majority of the 2,482 confirmed cases were reported in the Middle East, although the virus was introduced into 27 countries. A total of 203 new MERS-CoV cases were reported in

2019 and there is currently no vaccine or cure for MERS. Zoonotic MERS-CoV transmission from dromedary camels (the host reservoir for this virus) along with human-to-human transmission are the two known modes of infection (*30*, *31*). Emergence of (zoonotic) coronaviruses has already and likely continue to occur in the future, given the large reservoir in bats and birds, underscoring the importance of studying these pathogens (*32*–*35*).

MERS-CoV is an enveloped Nidovirus decorated with homotrimers of the spike (S) glycoprotein that mediates entry into host cells. S is the major antigen present at the viral surface and is the target of neutralizing antibodies during infection as well as the focus of vaccine design. Recent Cryo-EM structures of MERS-CoV and related coronavirus S ectodomain trimers provided snapshots of this key protein in prefusion (*36*–*43*) and postfusion conformations (*44*), receptor-bound states (*6*, *45*, *46*) and in complex with neutralizing antibodies (*47*, *48*). MERS-CoV S is composed of an N-terminal S1 subunit, which is folded as four domains (A–D) and mediates attachment to dipeptidyl-peptidase 4 (DPP4, the host receptor) (*49*), and a C-terminal S2 subunit that merges the viral and cellular membranes to initiate infection. MERS-CoV S is cleaved at the junction between the S1 and S2 subunits either during viral biogenesis or upon encounter of target cells (*50*–*53*). A second cleavage site, designated S2′, is found upstream of the fusion peptide in the S2 subunit and is processed at the onset of membrane fusion. Both cleavage sites participate in enhancing viral entry and modulating host range and cell tropism (*50*, *51*, *54*).

Sialic acids (derivatives of neuraminic acid) are ubiquitous carbohydrates found as terminal residues on glycoproteins and glycolipids decorating the surface of

eukaryotic cells. Neuraminic acid modifications, along with the formation of specific glycosidic linkages, result in a wide chemical variety of sialoglycoconjugates across cell types, tissues and animal species (*55*). As a result, differential sialoside recognition can profoundly impact the zoonotic transmission, tropism and virulence of many viruses. For example, a few amino acid substitutions in influenza virus hemagglutinins account for the preference switch from avian enteric tract to human respiratory tract sialylated receptors (*56*–*58*).

MERS-CoV primarily infects human lung epithelial cells upon interacting with DPP4 (*49*). Crystal structures of the MERS-CoV S domain B in complex with the DPP4 ectodomain (*7*, *59*), along with cryo-EM structures of the MERS-CoV S ectodomain trimer (*43*, *47*, *48*), have furthered our understanding of the mechanism of DPP4 engagement. In addition to attachment to DPP4, we recently showed that MERS-CoV infection of human airway epithelial cells involves low-affinity interactions with sialosides, using the S glycoprotein domain A, as depletion of sialic acid from the cell surface dampened viral entry (*60*). A binding preference was found for α2,3-linked over α2,6-linked sialosides, and these interactions were hindered by 9-O-acetylation or 5-N-glycolylation of the terminal neuraminic acid (*60*). Furthermore, we found that MERS-CoV S sialylated receptors are abundant in the camel nasal respiratory epithelium and the human lung alveoli, which coincides with DPP4 expression and the sites of MERS-CoV replication in these mammals (*60*, *61*). As sialoside modifications, linkages and distribution vary among and within host species, the selectivity of MERS-CoV S for certain sialoside glycotopes may provide a determinant of host and tissue tropism of this zoonotic pathogen. These findings provided a plausible rationale

for explaining that equine DPP4 could support MERS-CoV infection of cultured cells, although horses were found to be resistant to experimental MERS-CoV infection (despite the presence of DPP4 in their respiratory tract) (*62*–*64*). Although sialoside attachment appears to be a key step modulating MERS-CoV infection, the location of the sialoside-binding site, the interactions involved in ligand recognition and the molecular basis for receptor specificity remain unknown. This information is crucial for understanding viral tropism and infectivity, assessing the zoonotic potential of MERS-CoV and related coronaviruses, and providing a blueprint for the design of coronavirus inhibitors.

To understand the structural basis of MERS-CoV attachment to and specificity for host sialosides, we determined cryo-EM structures of the S glycoprotein ectodomain trimer in complex with 5-N-acetyl neuraminic acid (Neu5Ac) at 2.7Å resolution globally. We demonstrate that the receptor binds in a groove located at the surface of domain A that is distinct from the 9-O-acetyl sialoside-engagement site identified for HCoV-OC43 and related β-1 coronavirus S glycoproteins (*46*, *65*). We further show that the residues involved in Neu5Ac recognition are conserved across MERS-CoV isolates and essential for MERS-CoV S-mediated hemagglutination of human erythrocytes and entry into human airway epithelial cells. Our data rationalize MERS-CoV S attachment to neuraminic acids that are not 9-O-acetylated or 5-N-glycolylated. This study provides a structural framework for understanding MERS-CoV S sialoglycan receptor engagement, illuminates host range and cell tropism, and identifies a site of vulnerability accessible to neutralizing antibodies and small-molecule inhibitors.

2.2 A sialoside-binding site in the MERS-CoV S glycoprotein

To identify the MERS-CoV S sialoside-recognition site, we determined a cryo-EM structure of the MERS-CoV S 2P stabilized ectodomain trimer incubated with 100 mM Neu5Ac at 2.7 Å resolution (Figure 2.1 A-B, Figure 2.2 A–G and Table 1) (*48*). The presence of the sialoside stabilized a large fraction of MERS-CoV S trimers in the closed state, with all three DPP4-binding B domains adopting a down conformation, obeying three-fold symmetry. We did not detect major conformational changes compared to closed protomers of the LCA60 Fab-bound MERS-CoV S structure (Cα r.m.s. deviation (r.m.s.d.) of 1.35 Å for 1,145 aligned residues) (*47*). The resolution estimate of our map is supported by the detection of ordered water molecules interacting with the S glycoprotein (Figure 2.2 F-G) and by the observation of folic acid bound to S, as previously identified using X-ray crystallography and mass spectrometry of isolated domain A (*48*, *66*). The density is equally well resolved for the ligand and the surrounding S amino acid residues, allowing unambiguous identification of the binding site and docking of Neu5Ac in the map (Figure 2.2 D). The ligand interacts with a groove located at the periphery of domain A that is distinct from the HCoV-OC43 S 9-O-acetyl sialoside-binding site19 (Figure 2.1 B-F and 2.3 A-C) (*46*). The absence of N-linked glycans in the immediate vicinity of the binding groove probably facilitates unobstructed engagement of sialoglycoconjugates at the surface of target cells (Figure 2.3 A). The ligand-binding site is located ~50 and ~75 Å away from the DPP4-binding site of a neighboring B domain in the closed or open state, respectively (Figure 2.1 B).

The ligand C1 carboxylate electrostatically interacts with the Ser133 side chain hydroxyl, and the 5-nitrogen atom is hydrogen-bonded to the Ile132 backbone carbonyl

(Figure 2.1 D-F). The Neu5Ac hydroxyl group at position 8 is hydrogen-bonded to the Arg307 side chain guanidium whereas the hydroxyl group at position 9 interacts with the Arg307 guanidium as well as the Ala92 backbone amide and carbonyl oxygen via hydrogen bonding (Figure 2.1 D-F). The ligand N-acetyl methyl inserts into a hydrophobic depression defined by residues Phe39, Phe101, Ile131 and Ile132 whereas the N-acetyl carbonyl oxygen is hydrogen-bonded to the Gln36 side chain amide (Figure 2.1 D-F). The sialoside buries 280 $Å^2$ of its surface upon MERS-CoV S engagement, corresponding to 61% of the ligand total accessible surface area, with most interactions occurring on the same side of the ligand. Bioinformatics analysis of MERS-CoV isolates shows that the residues contacting the sialoside or participating in the formation of the binding groove are conserved. Specifically, Gln36, Phe39, Phe101, Ile132 and R307 are strictly conserved in the 284 MERS-CoV isolates sequenced so far. The H91Y substitution is observed in four MERS-CoV isolates (human/Korea/Seoul/168–1–2015 GB, ALB08311; human/Korea/Seoul/168-2-2015 GB, ALB08322; human/KOR/Seoul/014-2015 GB, ANC28634.1; human/Riyadh_1337/KSA/2014 GB, AMW90853.1), the S133N or S133R substitutions are present in two isolates (human/England/4/2013 GB, AJD81440.1 and Hu/Quaseem-KSA-18012872/2018 GB, QBF80608.1, respectively) and the Q304K substitution is observed in 1 isolate (camel/UAE/D1164.11/2014 GB, AJG44080.1).

2.3 The sialoside binding site is required for S-mediated viral attachment and entry

To evaluate the importance of the interactions identified by cryo-EM for sialoside recognition, we substituted with alanine individual MERS-CoV S amino acid residues interacting with Neu5Ac and assessed the effect on domain A-mediated hemagglutination of human erythrocytes. As previously described, the wild-type MERS-CoV S domain A fused to human immunoglobulin Fc only promoted hemagglutination of human erythrocytes when multimerized on lumazine synthase nanoparticles, indicative of enhancement of low-affinity interactions via avidity (Figure 2.4 A and 2.5 A) (*60*). Complete inhibition of hemagglutination was observed, however, for each binding site mutant tested, that is, F39A, H91A, I132A, S133A and R307A (Figure 2.4 A and 2.5 A). These results validated the structural observations by demonstrating that recognition of Neu5Ac via these residues is necessary for MERS-CoV S-mediated attachment to sialosides.

To further assess the functional relevance of the identified interactions, we interrogated the impact of individual domain A substitutions on MERS-CoV S-mediated entry into target cells. We used the murine leukemia virus platform with a luciferase reporter for quantifying entry of particles pseudotyped with either wild-type or mutant MERS-CoV S into human airway Calu-3 cells (*67*). The S133A and R307A substitutions abrogated entry of pseudotyped particles due to disruption of the aforementioned electrostatic interactions involving the Neu5Ac C1 carboxylate and glycerol side chain, respectively (Figure 2.4 B and 2.5 B). The F39A and H91A mutants showed reduced infectivity of the pseudotyped particles by more than 90%, probably due to disruption of

the ligand-binding groove and loss of favorable van der Waals or electrostatic interactions (Figure 2.4 B and 2.5 B). These findings demonstrate the key role of the identified residues for interacting with Neu5Ac in the context of a full-length, membrane-embedded MERS-CoV S glycoprotein and show that attachment to sialoside receptors using the binding site identified by cryo-EM is essential for promoting MERS-CoV S-mediated entry into human airway Calu-3 cells. Furthermore, as sialidase treatment of Calu-3 cells or mutations of the S sialoside-recognition site abrogated MERS-CoV S-mediated entry, it is likely that sialoside attachment either precedes DPP4 engagement or occurs simultaneously (*60*).

2.4 Discussion

We show here that sialosides bind to MERS-CoV S using a site distinct from the one observed for HCoV-OC43 S in complex with 9-O-acetyl sialylated receptors (*46*, *65*), despite the fact that the bound ligands are only separated by a few ångstroms from each other when superimposing the two structures. Although the β-sandwich architecture of domain A is conserved among all coronaviruses, distinct variable loops are grafted onto it, and neither the MERS-CoV S nor the HCoV-OC43 S sialoside-binding site is conserved in the infectious bronchitis virus S glycoprotein (*38*), which is known to engage α2,3-sialosides at the surface of avian host cells (*68*). These findings suggest coronavirus S glycoproteins have independently evolved the ability to recognize sialosides using domain A, similar to their ability to engage different proteinaceous receptors via modifications of domain B. Our results therefore set coronavirus S glycoproteins apart from influenza virus A hemagglutinins, which

recognize the Neu5Ac moiety through a largely conserved binding site (*56*, *57*). We hypothesize that coronaviruses that utilize both an entry receptor and an attachment receptor for infection, such as MERS-CoV or transmissible gastroenteritis virus, have more evolutionary freedom with respect to their ability to attach to sialoglycans than viruses only using an entry receptor. This could have led to the independent loss and/or acquisition of a sialoside-recognition function as an adaptation to new hosts upon cross-species transmission of distinct viruses. The ability to interact with sialoglycoconjugates might be a recent MERS-CoV S acquisition, as neither HKU4 S1 nor HKU5 S1 could hemagglutinate human erythrocytes (*60*). This modular evolutionary plasticity underlies coronavirus cross-species transmission, switching of host cell types and viral fitness.

We previously suggested that MERS-CoV S interacts with sialoside receptors through lower-affinity interactions than influenza A/California/04/2009 hemagglutinin (containing the T200A and E227A substitutions), as multimerization with a lumazine synthase nanoparticle was required to detect binding of a dimeric MERS-CoV S domain A-Fc construct but not of a dimeric hemagglutinin ectodomain-Fc construct (*60*). Because influenza A virus utilizes neuraminidase to promote the release of progeny virions from host cells, off-target cells or decoys, the enhanced affinity for sialosides is balanced with a receptor-destroying enzyme. Similarly, HCoV-OC43 possesses a hemagglutinin esterase with receptor-destroying activity to achieve the same function (*69*). Because MERS-CoV does not encode an equivalent enzyme, the binding dynamic of viral particles to sialoside receptors is entirely based on the energetics of these reversible interactions (*60*). The strong dependence on interactions with sialosides for

MERS-CoV entry into human airway Calu-3 cells is therefore probably a result of the high concentration of sialylated receptors (*60*), favoring virus adsorption through avidity and potentially increasing the likelihood of binding to DPP4, leading to viral entry. Similar roles have been proposed for carcinoembryonic antigen-related cell adhesion molecule 5 and binding immunoglobulin protein (*70*, *71*).

Although MERS-CoV S is densely decorated with N-linked glycans, the sialoside-recognition site is unobstructed, a possible requirement for receptor engagement. This finding is in marked contrast with the conformational masking and/or glycan shielding of the domain B entry receptor-binding motifs observed for several coronavirus S glycoproteins, including MERS-CoV S (*6*, *41*, *43*, *47*, *48*). We recently identified an antibody-blocking domain A-mediated hemagglutination of erythrocytes with in vitro neutralizing activity of MERS-CoV S pseudovirions and partial in vivo prophylactic protection of mice challenged with a lethal dose of MERS-CoV (*72*). These findings, along with our mutagenesis data, indicate that the sialoside-binding groove identified here represents a key site of vulnerability to inhibitors of MERS-CoV infection that could be targeted for the future development of therapeutics.

2.5 Figures & Tables

Figure 2.1 Cryo-EM identification of a sialoside-binding site in the MERS-CoV S glycoprotein.

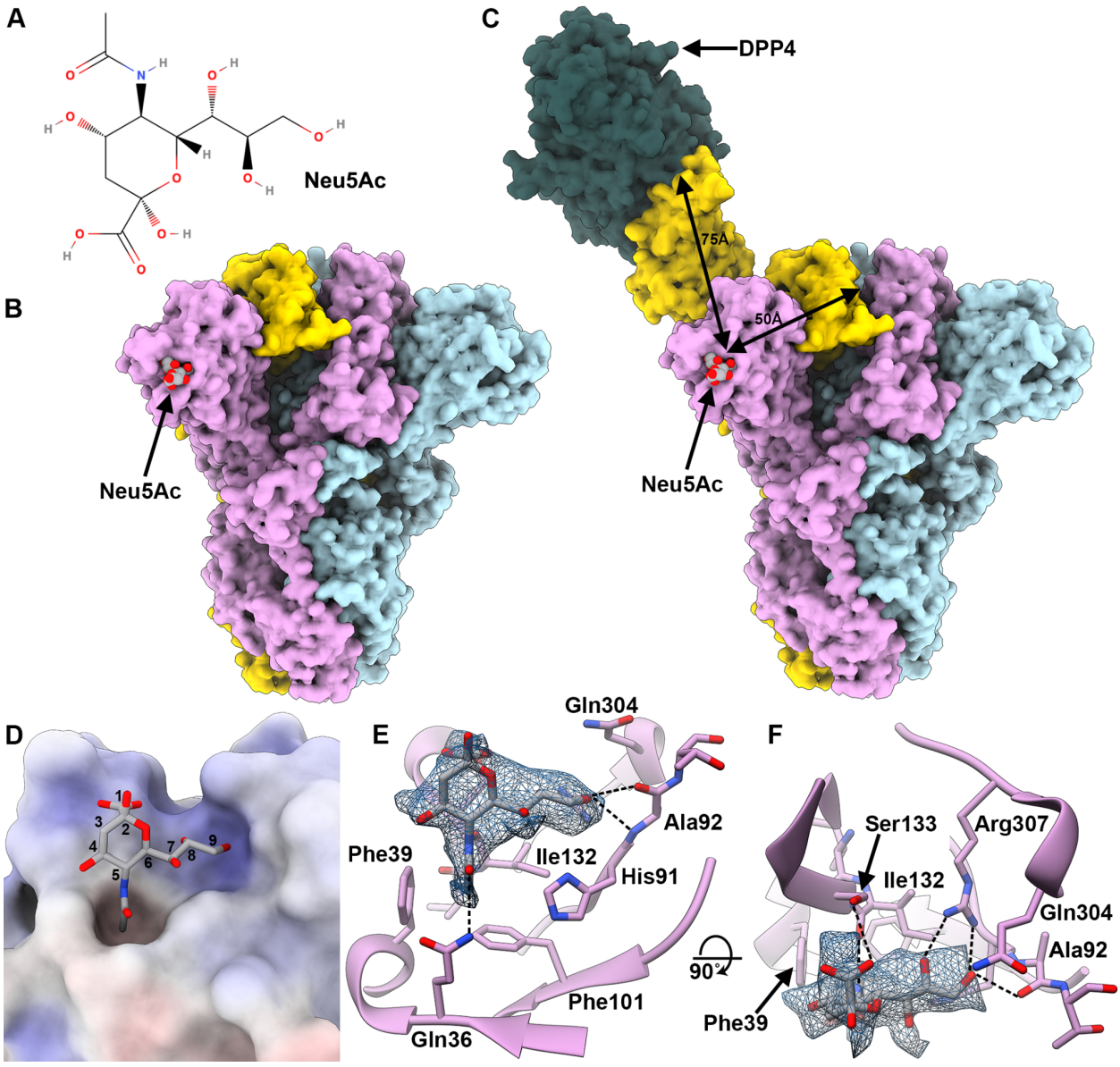

(**A**) Neu5Ac. (**B**) Molecular surface representation of the MERS-CoV S ectodomain trimer, with each protomer in a different color. The Neu5Ac ligands are rendered as spheres. (**C**) Spatial relationships between the attachment (sialoside) and entry (DDP4) receptor-binding sites are illustrated using a composite model obtained

from the cryo-EM structure shown in a, the cryo-EM structure of MERS-CoV S bound to the LCA60 neutralizing antibody Fab fragment (PDB 6NB3) and a crystal structure of the MERS-CoV S domain B bound to DPP4 (PDB 4KR0). The sialoside-binding site is located ~50 and ~75 Å away from the DPP4-binding site of a neighboring B domain in the closed or open state, respectively. (**D**) Surface representation of the ligand-binding site colored by electrostatic potential from −12 (red) to +10 (blue) kBT/ec. Neu5Ac is shown in stick representation. (**E-F**) Two orthogonal views of the sialoside-binding site rendered as a ribbon diagram with the side chains of key surrounding residues shown as sticks. Neu5Ac is rendered as sticks and the corresponding region of cryo-EM density is shown as a blue mesh contoured at 5.5σ. Dashed lines show selected electrostatic interactions formed between MERS-CoV S amino acid residues and the ligand. In all panels, nitrogen and oxygen atoms are colored blue and red, respectively, while carbon atoms are colored gray (Neu5Ac) or pink (MERS-CoV S). Glycans in MERS-CoV S have been omitted for clarity.

Figure 2.2 CryoEM analysis of the MERS-CoV S glycoprotein in complex with Neu5Ac at 2.7 Å resolution.

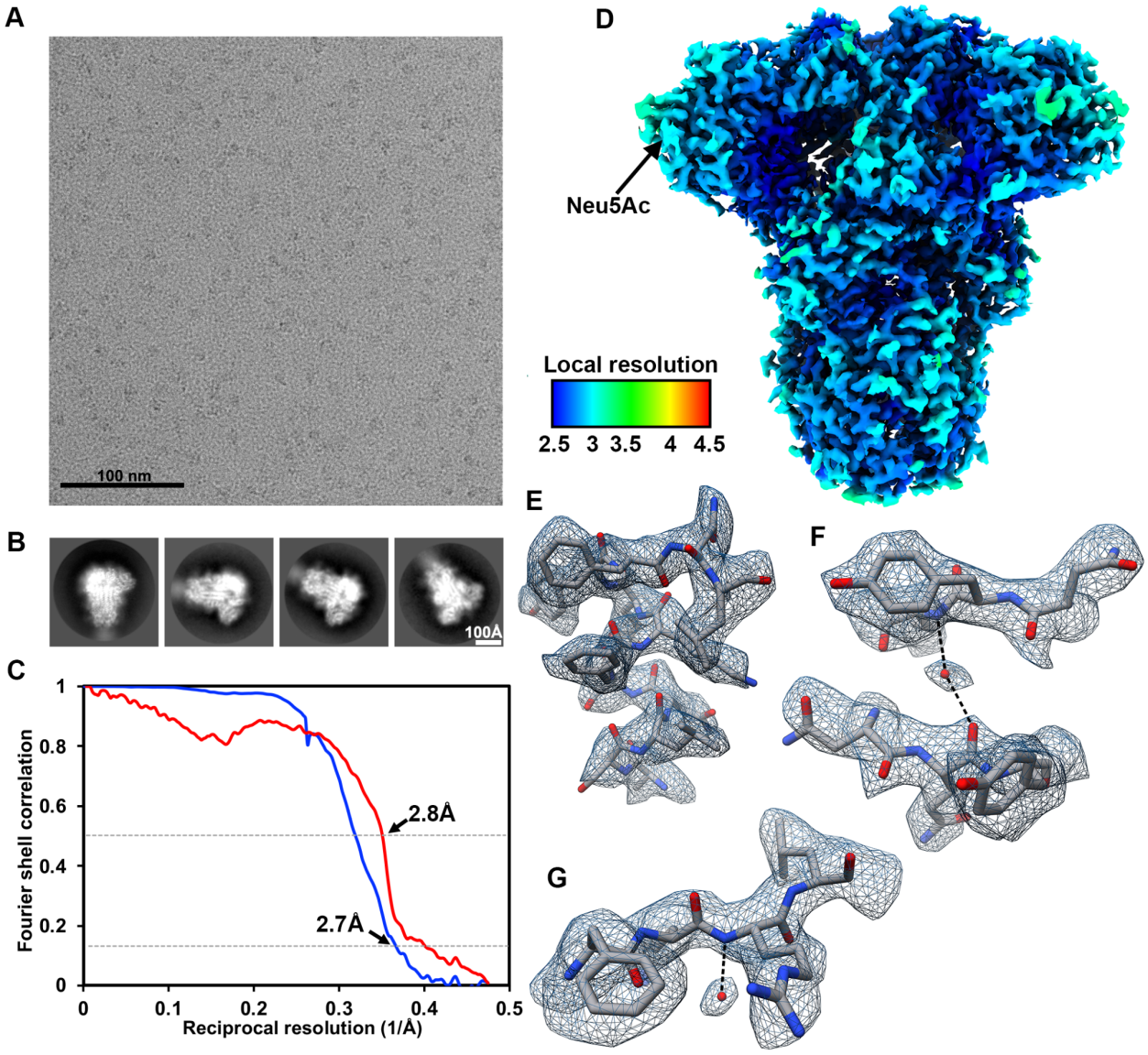

(**A-B**) Representative electron micrograph (**A**) and class averages (**B**) for the Neu5Ac-bound MERS-CoV S structure. (**C**) Gold-standard (blue) and map/model (red) Fourier shell correlation curves. The 0.143 and 0.5 cutoffs are indicated by horizontal dashed lines. (**D**) Local resolution map calculated using cryoSPARC. The Neu5Ac ligand is estimated to be resolved at 3Å resolution. (**E-G**) Representative cryoEM densities shown as blue mesh with the corresponding atomic model rendered as sticks colored gray, blue and red for carbon, nitrogen and oxygen atoms, respectively. Dashed bonds indicate hydrogen bonds with ordered water molecules.

Figure 2.3 MERS-CoV S and HCoV-OC43 S glycoproteins interact with sialosides, using distinct binding grooves.

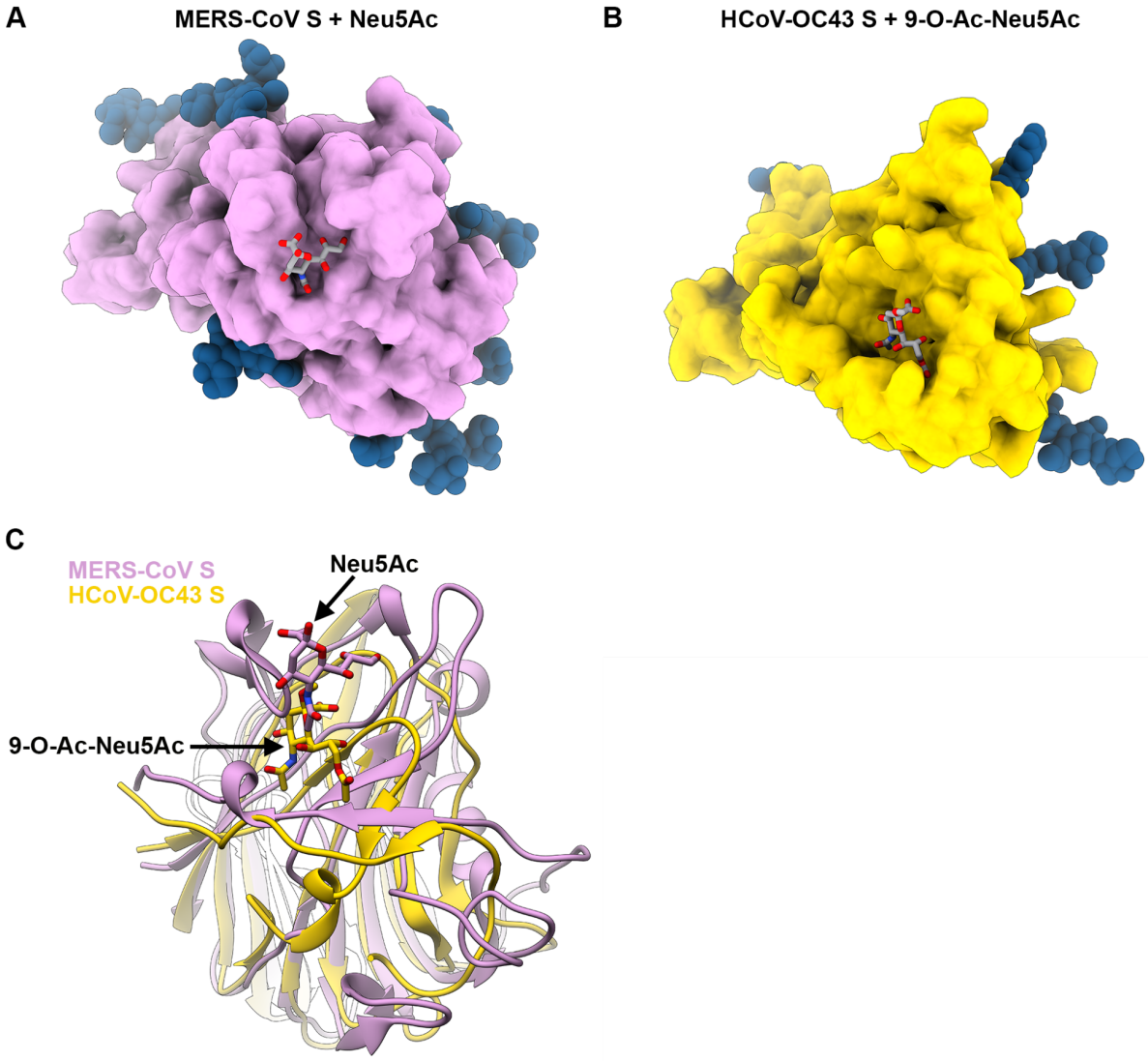

(**A-B**) Molecular surface representation of the MERS-CoV S (**A**) and HCoV-OC43 S (**B**) A domains bound to Neu5Ac and 5-N-acetyl,9-O-acetyl neuraminic acid α-methyl glycoside (9-O-Ac-Neu5Ac, PDB 6NZK), respectively, and oriented identically. The sialosides are rendered as sticks with carbon, nitrogen and oxygen atoms colored gray, blue and red, respectively. N-linked glycans observed in the cryo-EM reconstructions are rendered as dark blue spheres. (**C**) Ribbon diagrams of superimposed MERS-CoV S (pink) and HCoV-OC43 S (gold) A domains with bound sialosides. The sialosides are

rendered as sticks with carbon, nitrogen and oxygen atoms colored pink (MERS-CoV S) or gold (HCoV-OC43 S), blue and red, respectively.

Figure 2.4 The ligand-binding site is required for MERS-CoV S-mediated attachment to sialosides and entry into human airway epithelial cells.

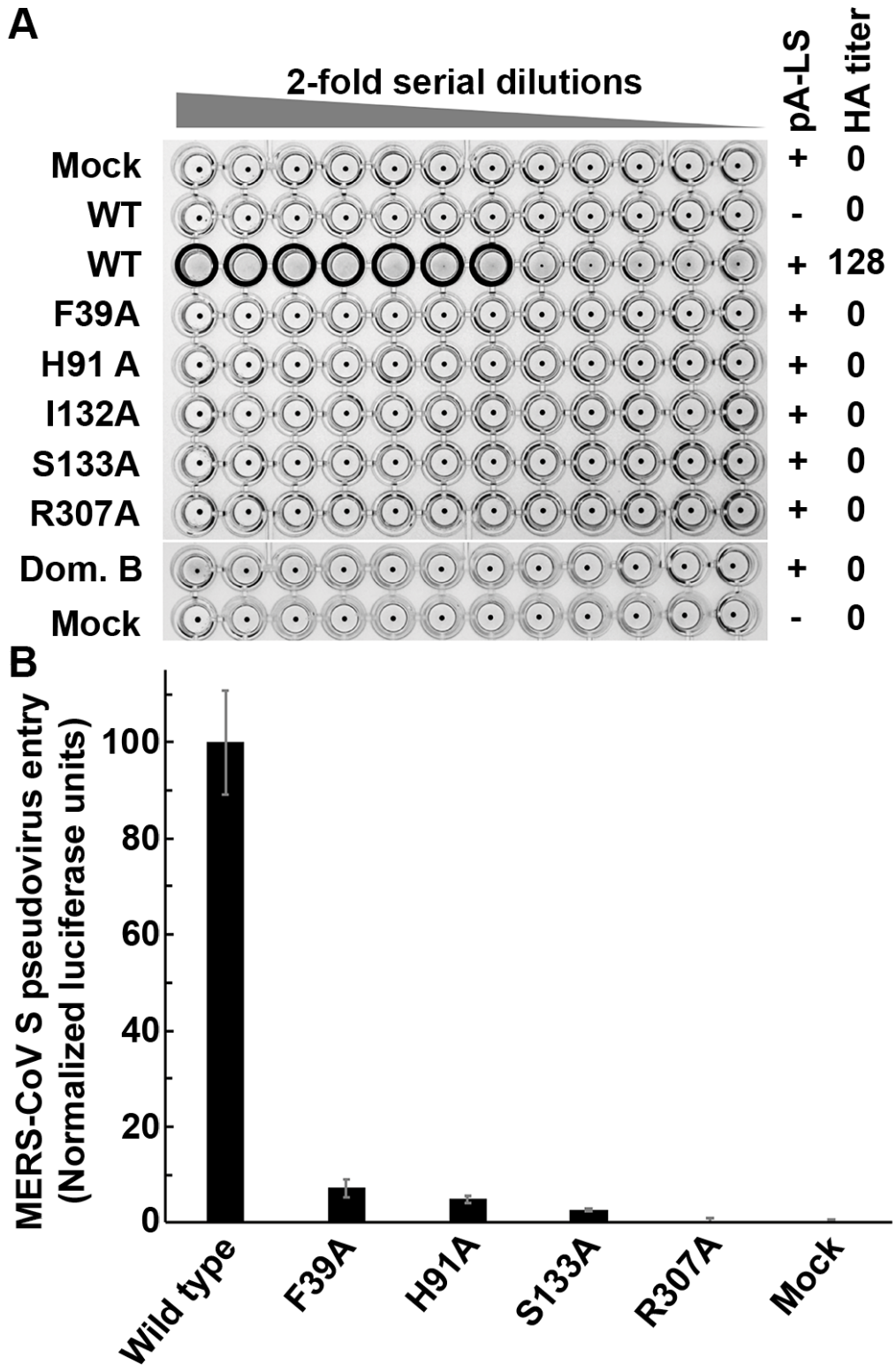

(**A**) Hemagglutination assay using MERS-CoV S wild type (WT) or mutants. Wells positive for hemagglutination (HA) are encircled. F39A, H91A, I132A, S133A or R307A substitutions completely abrogated domain A-Fc-mediated hemagglutination of human erythrocytes. Mock-treated erythrocytes, absence of the protein A-fused lumazine synthase (pA-LS) or replacement of domain A with domain B (Dom. B) were used as negative controls. The assays were performed four times and a representative experiment is shown. (**B**) MERS-CoV S F39A, H91A, S133A or R307A substitutions inhibited entry of pseudotyped murine leukemia viral particles into human airway Calu-3 cells. Data are normalized relative to wild type and shown as mean and s.d. of n = 3 pseudovirus experiments (technical replicates).

Figure 2.5 SDS-PAGE and Western blot analyses.

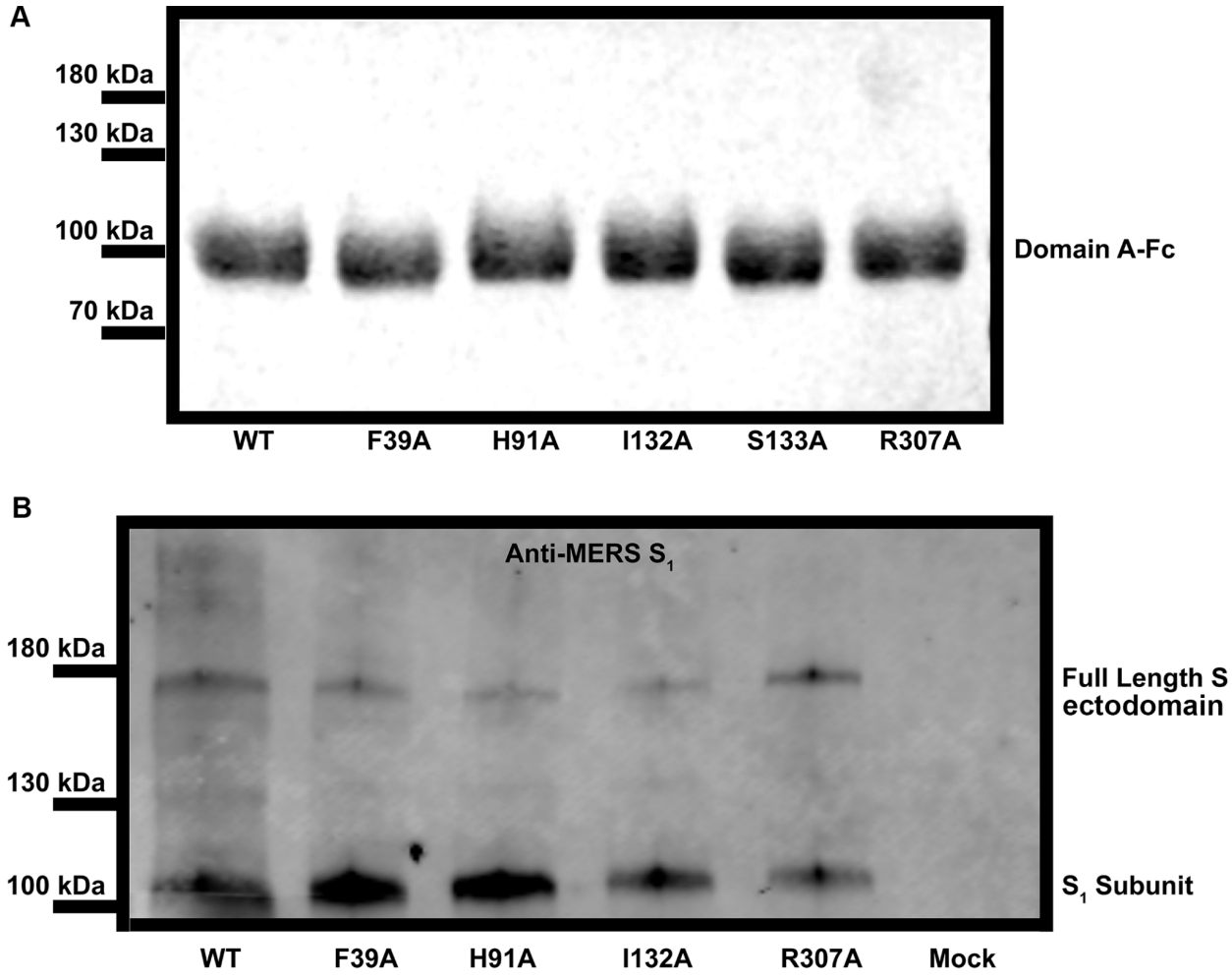

(**A**) SDS-PAGE analysis of purified wild type or mutants MERS-CoV S domain A fused to human immunoglobulin Fc. Two micrograms of each protein were loaded. (**B**) Western-blot analysis of murine leukemia viral particles pseudotyped with wild type or mutants MERS-CoV S using an anti-MERS-CoV S1 polyclonal antibody. Uncropped blot image is available as source data.

Chapter 3. Architecture and antigenicity of the Nipah virus attachment glycoprotein

This chapter highlights the ability of single particle Cryo-EM on solving heterogeneous structures. Until now, rigidness and symmetry continue to be the key for solving high resolution structure, and a heterogeneous dataset will always lead to nothing but artificial noise. Here, I demonstrate that the current single particle Cryo-EM data processing pipeline is able to overcome such limitations by describing a zero-symmetric homotetramers structure of Nipah virus attachment protein, NiVG, at 3.2-3.5Å as well as multi-classes negative stain EM maps from single multicomplex dataset of G protein in complex with polyclonal antibody Fab fragments.

On the biological side, this is the first attachment protein full ectodomain structure of not only the henipavirus family but also the whole paramyxovirus superfamily. This structure also revealed a very important broadly neutralizing epitope for both Nipah and Hendra virus, and allowed us to propose a synergistic mAb cocktail. Meantime, the structures of G protein in complex with polyclonal Fab fragments narrow down the potent antigenic site, which is further validated by depletion experiments. Together, this study provides a blueprint for henipavirus vaccine development.

3.1 Abstract

Nipah virus (NiV) and Hendra virus (HeV) are zoonotic henipaviruses (HNVs) responsible for outbreaks of encephalitis and respiratory illness. The entry of HNVs into host cells requires the attachment (G) and fusion (F) glycoproteins, which are the main

targets of antibody responses. To understand viral infection and host immunity, we determined a cryo–electron microscopy structure of the NiV G homotetrameric ectodomain in complex with the nAH1.3 broadly neutralizing antibody Fab fragment. We show that a cocktail of two nonoverlapping G-specific antibodies neutralizes NiV and HeV synergistically and limits the emergence of escape mutants. Analysis of polyclonal serum antibody responses elicited by vaccination of macaques with NiV G indicates that the receptor binding head domain is immunodominant. These results pave the way for implementing multipronged therapeutic strategies against these deadly pathogens.

3.2 Architecture of the NiV G tetramer

To unveil the three-dimensional (3D) organization of the HNV G protein and provide a blueprint for vaccine design, we determined a cryo–electron microscopy (cryo-EM) structure of the NiV G ectodomain homotetramer bound to the mouse nAH1.3 neutralizing antibody Fab fragment at 3.5-Å overall resolution (Figure 3.1) (*73*). We used local refinement to account for the flexibility of the viral membrane proximal region relative to the distal region, yielding reconstructions at 3.5-Å and 3.2-Å resolution, respectively, allowing us to build a (composite) model of the NiV G ectodomain tetramer (Figure 3.2 A-C, 3.1 and table S1). The final model comprises nearly the entire NiV sG ectodomain from residues 96 to 602 along with the nAH1.3 Fab variable domains. NiV G forms a 200-Å-long and 120-Å-wide intertwined homotetramer. At the core is an N-terminal four-helix bundle (the stalk) followed by an interlaced β sandwich (the neck) that connects to a C-terminal β propeller head domain on each protomer (Figure 3.2

A-C). The NiV G tetramer is stabilized by interprotomer disulfide bonds formed in the neck and stalk (Figure 3.2 D).

NiV G residues 96 to 147 form a pseudo–two-fold symmetric helical bundle, which is presumably extended at its N-terminal end toward the viral membrane in which the tetramer is anchored (residues 70 to 95 are weakly resolved in the cryo-EM map and were not modeled) (Figure 3.2 A-C). The interlaced β sandwich neck domain is formed by apposition of two four-stranded mixed β sheets, packed against each other through hydrophobic contacts, comprising residues 153 to 163 from each of the four protomers (Figure 3.2 D). The neck is covalently cross-linked through formation of two antiparallel interprotomer disulfide bonds between residues C158 and C162 of chains A and D and two antiparallel disulfide bonds between residues C158 and C162 of chains B and C. The neck is decorated with four N-linked glycans protruding from residue N159 on each protomer, partially shielding this domain on both sides of the β sandwich (Figure 3.2 D). Each of the four C-terminal head domains form a six-bladed β propeller decorated with five N-linked oligosaccharides at positions N306, N378, N417, N481, and N529, which are all resolved in the cryo-EM map (Figure 3.2 A-C). Two head domains are connected to the neck through flexible linkers folding back toward the viral membrane, with the β propellers docked on either side of the stalk (Figure 3.2 B-C). The other two head domains form a head-to-tail dimer positioned distal to the viral membrane and are connected to the neck through linkers that adopt distinct folds (Figure 3.2 B-C). As a result, the NiV G tetramer is assembled from four identical polypeptides adopting three distinct folding patterns (Figure 3.2 E). Interactions between the two distal head domains maintain their approximately antiparallel orientation,

whereas contacts between each proximal head and the NiV G stalk lead to their pseudo–two-fold symmetrical arrangement. Only one of the four head domains orients its receptor binding site toward the host cell surface, whereas the other three sites point toward the viral membrane (Figure 3.2 F), suggesting that conformational dynamics would allow reorienting the head domains for receptor engagement. Although the cryo-EM map does not resolve the topology of the two stalk C146 disulfide bonds unambiguously, previous biochemical data suggest that they form across pairs of protomers that are not covalently cross-linked in the neck (*74*, *75*). The overall NiV G architecture described here adopts a distinctive two-heads-up and two-heads-down conformation that is different from structures of any other paramyxovirus attachment glycoproteins. In comparison, Newcastle disease virus hemagglutinin-neuraminidase (HN) ectodomain adopts a four-heads-down conformation, whereas parainfluenza virus 5 HN exhibits a distinct two-heads-up and two-heads-down conformation with the receptor binding sites oriented differently than for NiV G (Figure 3.3) (*76*, *77*).

3.3 nAH1.3-mediated broad neutralization of NiV and HeV

The nAH1.3 mAb was previously shown to potently neutralize NiV-M, NiV-B, and HeV in vitro (*73*). Using a green fluorescent protein (GFP)–encoding, replication-competent Cedar (henipa)virus (rCedV) chimeras in which the native glycoproteins are substituted with the NiV-B (rCedV-NiV-B-GFP) or the HeV (rCedV-HeV-GFP) F and G glycoproteins (*78*), we determined nAH1.3 half-maximum inhibitory concentrations (IC50) of 33 and 32 ng/ml, respectively (Figure 3.4 A). This neutralization potency is comparable to the human mAb m102.4, for which we

determined IC50 values of 17 and 58 ng/ml against rCedV-NiV-B-GFP and rCedV-HeV-GFP, respectively (Figure 3.4 B). Our cryo-EM structure reveals that one nAH1.3 Fab fragment is bound to each NiV G head domain (Figure 3.2 B-C and 3.5 A). nAH1.3 heavy and light chains interact with an antigenic site located on the side of the β propeller that is opposite to the ephrin-B2 or ephrin-B3 binding site (Figure 3.5 A). As a result, nAH1.3 does not compete with receptor binding to the NiV G ectodomain (Figure 3.5 B), unlike m102.4, which forms interactions mimicking receptor interactions (*79*). nAH1.3 buries ~1000 Å2 of its paratope upon binding through shape complementarity and hydrogen bonding involving complementarity-determining regions (CDRs) H1, H3, L1, and L2, explaining its high-affinity binding to NiV G (Figure 3.5 C-D and 3.4 C). nAH1.3 is conformation dependent and recognizes a discontinuous epitope, spanning residues 172, 182 to 191, 358, 448 to 451, 468 to 478, 515 to 518, and 570 and 571, which is in close proximity to the oligosaccharide at position N481 (Figure 3.2 A and 3.5 A). Twenty-one out of 26 epitope residues are strictly conserved across NiV G and HeV G, and three residues are conservatively substituted from NiV G to HeV G [Asn187→Gln (N187Q), N478Q, and I517L]. Only two residues are nonconservatively substituted (L470D and K571V), and these map to the periphery of the epitope (Figure 3.5 E). Our structural data suggest that none of the five substitutions would affect nAH1.3 recognition, as confirmed by the similar neutralization potencies determined against rCedV-NiV-B-GFP and rCedV-HeV-GFP (Figure 3.4 A). However, no cross-reactivity was detected with more-divergent HNV sG ectodomain tetramers from CedV, Ghana virus (GhV), and Mojiang virus (MojV) (Figure 3.4 D-E). Given that mAb nAH1.3 does not appear to affect the overall NiV G conformation or bind to the ephrin

virus entry receptor binding site, we propose that the mAb inhibits HNV entry into cells by interfering with its F fusion triggering mechanism, as supported by membrane fusion assays (*80*).

To validate our structural data, we passaged chimeric rCedV-NiV-B-GFP and rCedV-HeV-GFP in the presence of a subneutralizing concentration of nAH1.3. Deep sequencing revealed the selection of a clone harboring the I520T mutation (T1559C nucleotide substitution) introducing an N-linked glycosylation site at position N518 of NiV G. This is within the epitope recognized by nAH1.3 and likely abrogates mAb binding and neutralization via steric hindrance (Figure 3.5 F and 3.6 A). For HeV G, we identified an escape mutant harboring the T117A and N186D mutations. The latter substitution resides within the epitope and likely disrupts interactions with the nAH1.3 light chain (Figure 3.5 D, F and 3.6 B). Previously identified Q450K and R516K nAH1.3 escape mutations further validate our structure, as both residues form extensive interactions with the Fab heavy chain (Figure 3.5 F) (*73*). Moreover, passaging of rCedV-HeV-GFP in the presence of m102.4 led to the emergence of a single amino acid mutation in HeV G (D582N) (Figure 3.6 C), which is identical to the one previously identified using authentic HeV and NiV, validating the use of the chimeras as a surrogate system for pathogenic HNVs (*73*).

3.4 Synergistic neutralization of NiV and HeV by a mAb cocktail

mAb cocktails have successfully been used to prevent or treat infections with RNA viruses (*81*). For instance, although the individual Regeneron 10933 (casirivimab) and 10987 (imdevimab) mAbs against severe acute respiratory syndrome coronavirus 2

(SARS-CoV-2) are affected by a range of residue substitutions detected in clinical isolates, their combined cocktail proved more resilient to escape mutations (*82*, *83*). Because experimental passaging of NiV and HeV with low concentrations of neutralizing mAbs can favor the emergence of neutralization escape mutants, we tested a cocktail of m102.4 and nAH1.3, which recognize epitopes located on opposite sides of the β propeller (Figure 3.7 A). Analysis of the negatively stained complex between NiV G and the nAH1.3 and m102.4 Fabs by single particle analysis confirmed formation of a ternary complex (Figure 3.8 A-C), allowing the determination of a 3D reconstruction with three nAH1.3 and three m102.4 Fabs bound to a NiV G tetramer (Figure 3.8 C). We subsequently used biolayer interferometry to confirm that both mAbs can recognize the NiV G ectodomain immobilized at the surface of biosensors irrespective of their order of addition (Figure 3.7 B). We then carried out virus neutralization assays using rCedV-NiV-B-GFP or rCedV-HeV-GFP to examine whether these mAbs had synergistic virus-neutralizing activity (*78*). Using a concentration matrix of each mAb, we found that combining m102.4 and nAH1.3 led to synergistic neutralization of the two rCedV chimeras (Figure 3.7 C-D and 3.9 A-B). Passaging chimeric rCedV-HeV-GFP in the presence of the cocktail of nAH1.3 and m102.4 led to the emergence of the T117A, N186D, and T507I triple mutant, with T507I mapping to the m102.4 epitope and N186D to the nAH1.3 epitope, as described above (Figure 3.5 D, F and 3.6 D). These findings support the potential use of a cocktail of these two noncompeting G glycoprotein–directed neutralizing mAbs as a therapeutic against these two deadly HNVs owing to their synergy and the higher barrier for resistance due to the requirement for multiple mutations to escape neutralization.

3.5 The NiV G head domain is the main target of vaccine-elicited serum neutralization

We next investigated the nature and fine specificity of polyclonal Ab responses against the NiV G and HeV G glycoproteins using sera from two rhesus macaques that were immunized three times (4 weeks apart) with 200 μg of an alum-adjuvanted equimolar mixture of the purified NiV-B and NiV-M sG tetramers (Figure 3.10 A). The two immunizations elicited potent serum neutralizing activity at day 84, with geometric mean neutralization titers of 1/8434 and 1/992 against rCedV-NiV-B-GFP and rCedV-HeV-GFP, respectively (Figure 3.10 B). Using a competition enzyme-linked immunosorbent assay (ELISA) with the nAH1.3 (*73*), m102.4 (*84*), and HENV-32 mAbs (*85*), we showed that vaccine-elicited Abs target at least three distinct antigenic sites at the surface of the NiV G head domain with comparable magnitudes, illustrating the diversity of polyclonal Ab responses elicited by vaccination (Figure 3.10 C-E). To directly visualize the epitopes recognized by serum Abs, we used single particle electron microscopy analysis of negatively stained complexes formed between NiV G and purified polyclonal Fab fragments [obtained from immunoglobulin G (IgG) cleavage] after size-exclusion chromatography (*86*–*88*). 3D classification of the data led to the identification of at least three distinct classes of head-binding Abs and one class of stalk-specific Ab (Figure 3.10 F-J and 3.8 D-F). Overall, Ab responses are almost exclusively directed to the NiV G head domain, despite using the full ectodomain tetramer for immunization, underscoring an apparent focusing of Ab responses on the receptor binding domain (Figure 3.10 F-J and 3.8 D-F).

To understand the quantitative contribution of the different NiV G domains to serum neutralizing activity induced by vaccination, we depleted polyclonal Abs using either the purified isolated NiV G head domain or the tetrameric NiV G ectodomain. Neutralizing Ab titers for each of the two rhesus macaques were respectively reduced by a factor of 9 and 19 against rCedV-NiV-B-GFP (Figure 3.10 K and 3.9 C-F) and by a factor of 9 and 93 against rCedV-HeV-GFP (Figure 3.10 L and 3.9 G-H) after depletion of NiV G head-specific Abs. Serum Ab depletion using the NiV G ectodomain tetramer resulted in a respective dampening of neutralizing activity by a factor of 11 and 13 against rCedV-NiV-B-GFP (Figure 3.10 K and 3.9 I-L) and by a factor of 69 and 2.5 against rCedV-HeV-GFP (Figure 3.10 L and 3.9 M-N). Collectively, these data indicate that the NiV G head domain is immunodominant and the target of most serum neutralizing activity elicited by NiV G vaccination in rhesus macaques.

3.6 Discussion

Our structure of the NiV G ectodomain tetramer reveals the ultrastructural organization of this key target of the immune system, informs the mechanism of HNV entry into host cells, and provides a blueprint for engineering next-generation vaccine candidates with improved stability and immunogenicity, as was achieved for respiratory syncytial virus and SARS-CoV-2 (*5*, *48*, *89*–*95*). The discovery that the NiV and HeV G head domain is the target of most neutralizing activity in the serum of rhesus macaques vaccinated with tetrameric NiV G ectodomains motivates the development of vaccines focusing Ab responses on this domain of vulnerability. Presenting the head antigen as an ordered array through multivalent display holds the promise of enhancing

immunogenicity, as recently described for SARS-CoV-2 (*92*, *96*, *97*), and would allow presentation of a mosaic of HNV head domains with the goal of inducing neutralizing Ab responses with maximal breadth (*87*, *97*–*99*). Finally, the enhanced expression yield, stability, and homogeneity of the NiV G head domain compared with HeV sG would improve scalability of the manufacturing process of such a vaccine (*78*).

3.7 Figures & Tables

Figure 3.1 Cryo-EM data collection and processing of NiV G in complex with the nAH1.3 Fab fragment.

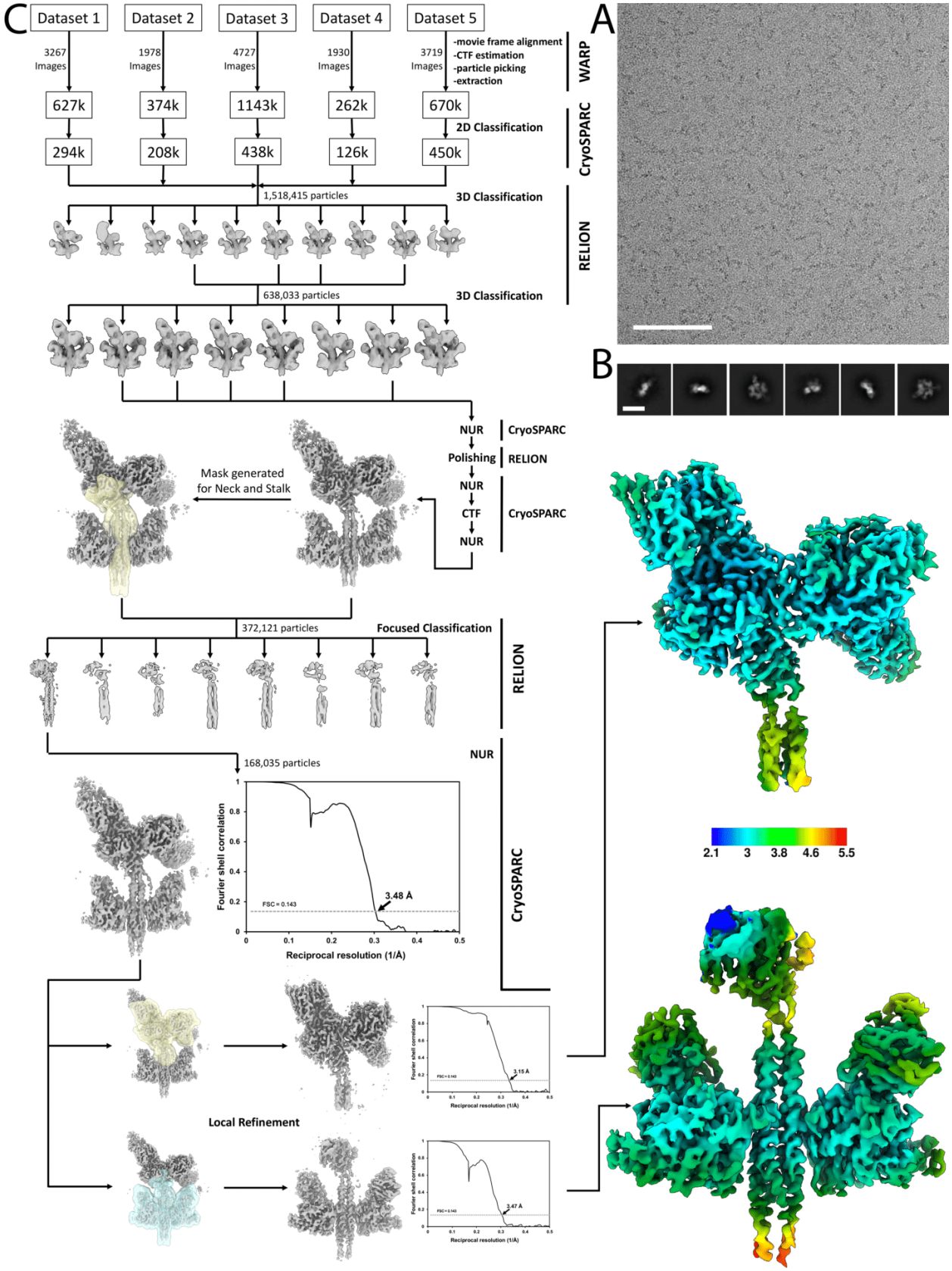
C
Dataset 1
Dataset 2
Dataset 3
Dataset 4
Dataset 5
3267 Images
1978 Images
4727 Images
1930 Images
3719 Images
-movie frame alignment
-CTF estimation
-particle picking
-extraction
WARP
627k
374k
1143k
262k
670k
2D Classification
294k
208k
438k
126k
450k
CryoSPARC
1,518,415 particles
3D Classification
RELION
638,033 particles
3D Classification
NUR
CryoSPARC
Polishing
RELION
NUR
CTF
CryoSPARC
NUR
Mask generated for Neck and Stalk
372,121 particles
Focused Classification
RELION
168,035 particles
NUR
CryoSPARC
Fourier shell correlation
FSC = 0.143
3.48 Å
Reciprocal resolution (1/Å)
Local Refinement
3.15 Å
3.47 Å
A
B
2.1
3
3.8
4.6
5.5

(**A**) Representative micrograph low-pass filtered at 10Å. Scale bar: 500Å (**B**) Representative 2D class averages. Scale bar: 100Å (**C**) CryoEM data processing flow chart including local resolution maps computed using cryoSPARC.

Figure 3.2 Architecture of the NiV G homotetramer.

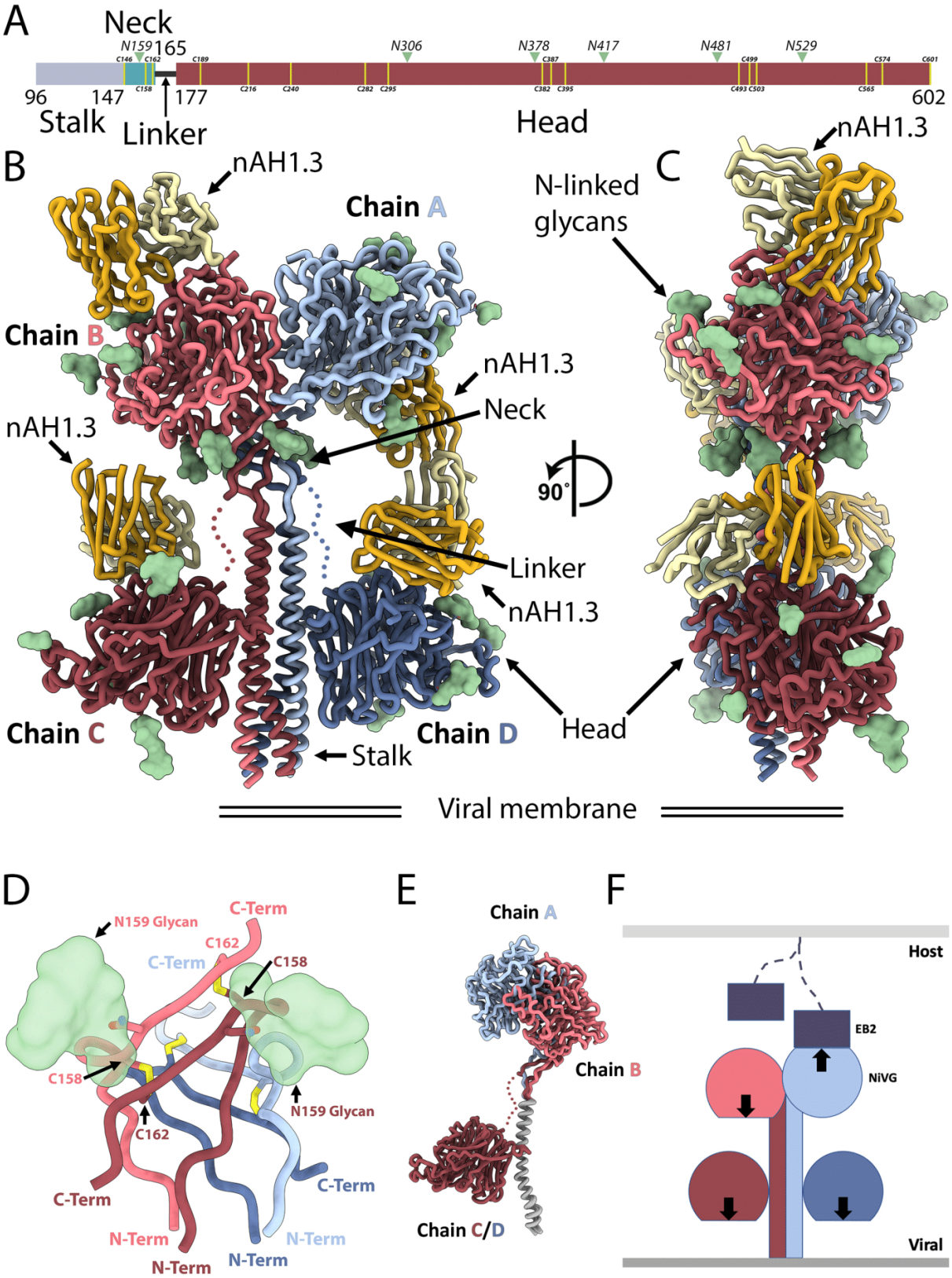

(**A**) Linear representation of the NiV G ectodomain (as resolved in the cryo-EM map), which contains an N-terminal stalk (residues 96 to 147), a neck domain (residues 148 to 165), a linker region (residues 166 to 177), and a C-terminal head domain (residues 178 to 602). Green arrowheads indicate N-linked glycosylation sites. Yellow lines refer to cysteine residues. (**B** and **C**) Ribbon diagram of the NiV G ectodomain bound to the broadly neutralizing nAH1.3 Fab fragment in two orthogonal orientations. Each of the four NiV G protomers is shown in a different color, and resolved N-linked glycans are rendered as green surfaces. The nAH1.3 heavy and light chains are colored gold and yellow, respectively, and only the variable domains were modeled in density. The linkers connecting the neck to the two proximal head domains are shown as dotted lines owing to weaker density in the cryo-EM reconstruction. (**D**) Zoomed-in view of the interlaced β sandwich neck domain showing the four antiparallel interprotomer disulfide bonds between residues C158 and C162 and the glycan at position N159 protruding from the two chains shown in the foreground. (**E**) Superimposition of NiV G protomers based on the stalk highlighting that the same polypeptide chain adopts three distinct folds in the homotetrameric assembly. (**F**) Schematic representation of the NiV G homotetramer showing that only one out of four head domains orients its receptor binding site (arrow) toward the host cell membrane (light gray), whereas the other three sites point toward the viral membrane (dark gray). EB2, ephrin-B2.

Figure 3.3 Comparison of NiV G and other paramyxovirus attachment glycoproteins.

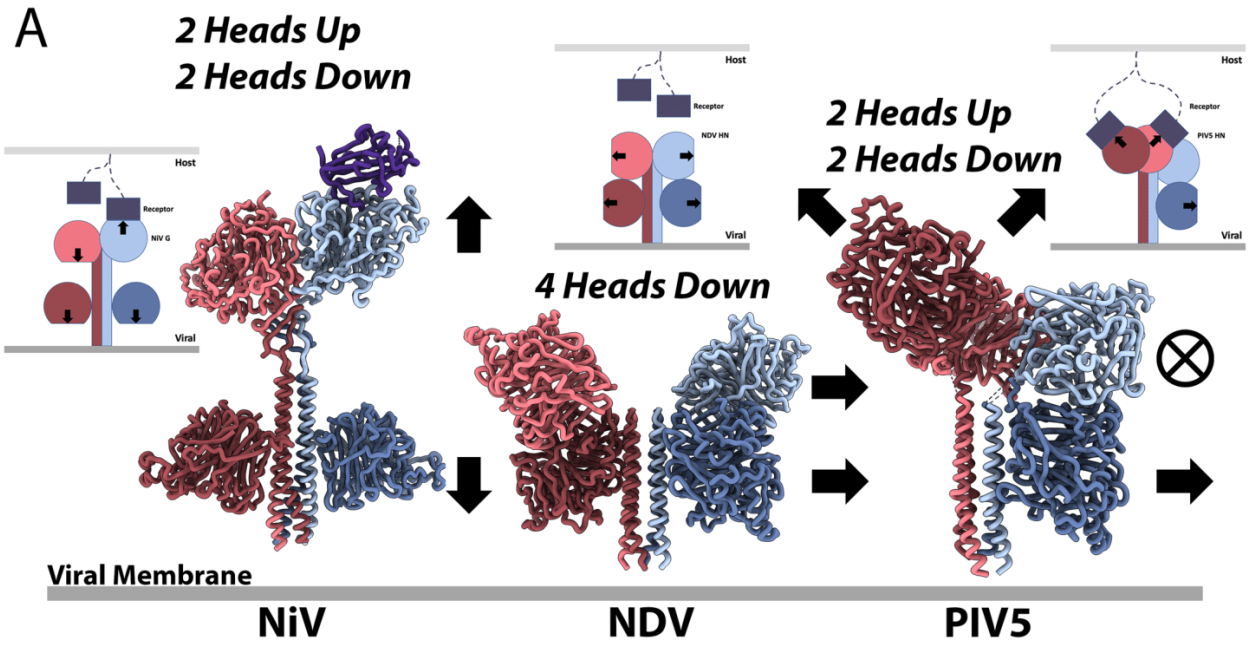

(**A**) NiV G adopts a two heads up and two heads down conformation, which is different from parainfluenza virus 5 (PIV5) HN “2 heads up 2 heads down” state (PDB 4JF7) and of Newcastle disease virus (NDV) HN “4 heads down” state (PDB 3T1E). The cartoon diagram shows the orientation of the head domains (semicircles) with an arrow indicating the receptorbinding site. The stalk is represented as a thin rod and the receptor is represented as a purple thick rectangle.

Figure 3.4 Characterization of the inhibitory and biophysical properties of the nAH1.3 mAb.

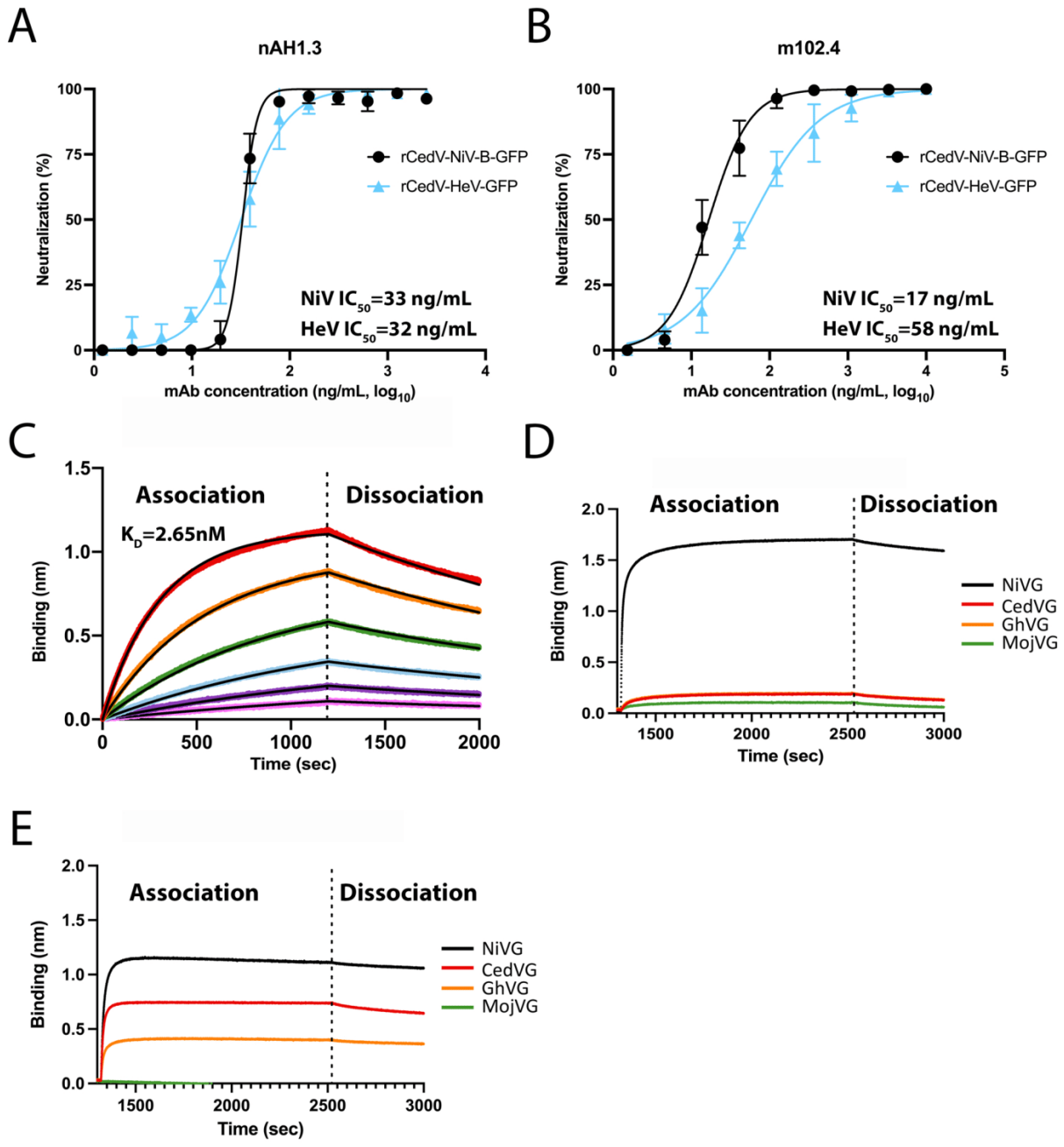

(**A-B**) nAH1.3-mediated neutralization (**A**) and m102.4-mediated neutralization (**B**) of rCedV-NiVB-GFP (black) and rCedV-HeV-GFP (blue) in Vero 76 cells. (**C**) Binding of the nAH1.3 Fab fragment to the immobilized NiV G head domain. nAH1.3 concentrations used were 20 nM (red), 10 nM (orange), 5 nM (green), 2.5 nM (blue),

1.25 nM (purple) and 0.625 nM (pink). Black traces show the fit to the data using a 1:1 global model and the vertical dashed line corresponds to the transition between association and dissociation phases. We determined an equilibrium dissociation constant (KD) of 2.65 nM. (**D-E**) Biolayer interferometry analysis of binding of the nAH1.3 IgG and ephrin-B2 to the immobilized HNV G proteins. Amine-coupled NiV G (black), CedV G (red), GhV G (orange), or MojV G (green) biosensor probes were dipped into 600 nM nAH1.3 IgG (**D**) or 600 nM human ephrin-B2 monomer (**E**).

Figure 3.5 Structural basis for nAH1.3-mediated broad neutralization of NiV and HeV.

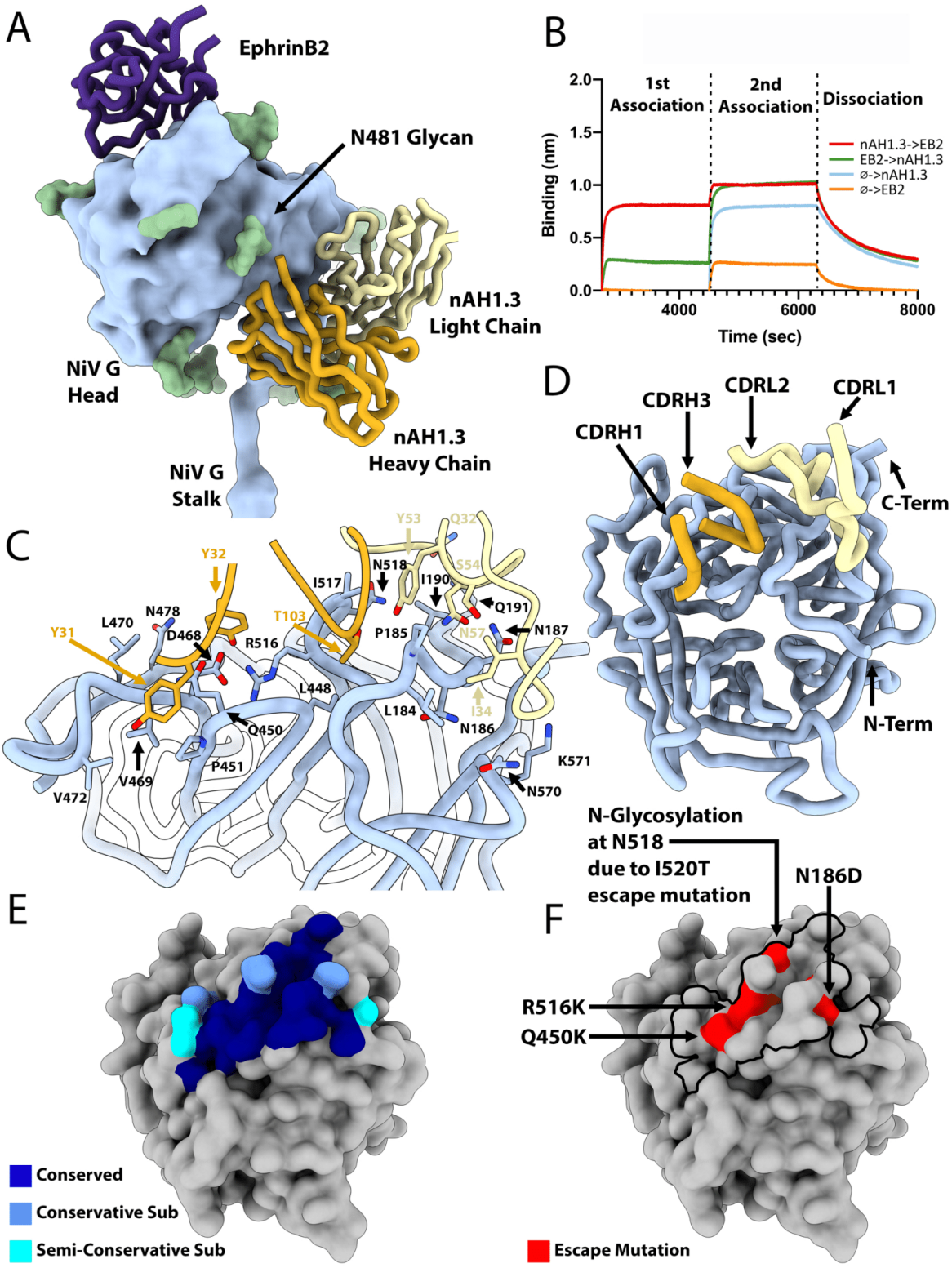

(**A**) Superimposition of the NiV G head domain (blue surface) bound to nAH1.3 (heavy and light chains, colored gold and yellow, respectively) or to ephrin-B2 [purple; Protein Data Bank (PDB) ID 2VSM] showing that they bind to opposite sides of the β propeller. (**B**) Biolayer interferometry analysis of binding of the nAH1.3 Fab and EB2 to immobilized NiV G ectodomain showing absence of competition irrespective of their order of addition. Each NiV G loaded anti-penta-His biosensor probe was sequentially dipped in a solution containing 25 nM nAH1.3 Fab (red) and then 50 nM EB2 plus 25 nM nAH1.3 Fab (red) or 50 nM EB2 and then 25 nM of nAH1.3 Fab plus 50 nM EB2 (green). Controls with only nAH1.3 Fab (blue) or EB2 (orange) are shown for comparison. (**C**) Zoomed-in view of the interface between NiV G and nAH1.3 with selected side chains shown as sticks. Single-letter abbreviations for the amino acid residues are as follows: A, Ala; C, Cys; D, Asp; E, Glu; F, Phe; G, Gly; H, His; I, Ile; K, Lys; L, Leu; M, Met; N, Asn; P, Pro; Q, Gln; R, Arg; S, Ser; T, Thr; V, Val; W, Trp; and Y, Tyr. (**D**) Ribbon diagram of a NiV G head domain (blue) with the interacting nAH1.3 heavy and light chains CDRs (CDRH and CDRL) rendered in gold and yellow, respectively. (**E**) Molecular surface representation of the NiV G head showing the nAH1.3 footprint colored by residue conservation between NiV G and HeV G. Conservative sub, conservative substitution; semi-conservative sub, semi-conservative substitution. (**F**) Molecular surface representation of the NiV G head showing the nAH1.3 escape mutations identified here (I520T introducing an N-linked glycosylation site at position N518; N186D comes from HeV G escape mutant) and Q450K and R516K [previously described].

Figure 3.6 Deep-sequencing of chimeric rCedV-NiV-B-GFP and rCedV-HeV-GFP reveals G protein mutations that permit escape from nAH1.3 or m102.4 mAbs.

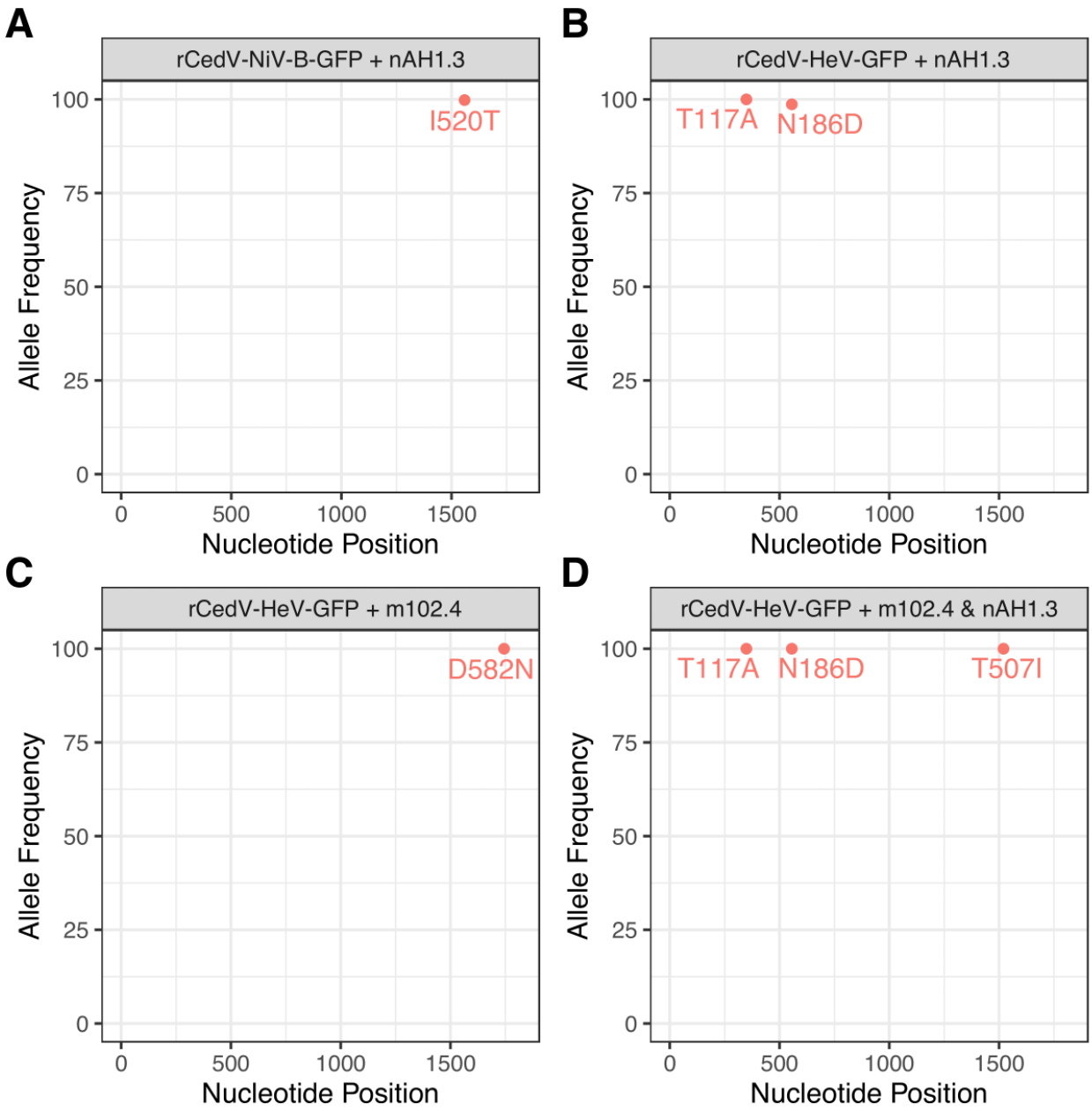

(**A**) rCedV-NiV-B-GFP was passaged in the presence of nAH1.3 until the virus was no longer neutralized by the mAb. Deep sequencing of this virus revealed a single mutation, I520T, in the NiV G protein allowing the chimeric virus to evade neutralization by nAH1.3. (**B-D**) rCedV-HeV-GFP was passaged in the presence of nAH1.3 (**B**), m102.4 (**C**), or a combination of nAH1.3 and m102.4 (**D**) until the virus was no longer

neutralized by the mAb(s). Deep sequencing of this virus revealed two mutations, T117A and N186D, in the HeV G protein allowing the chimeric virus to evade neutralization by nAH1.3. A single G protein mutation, D582N, allowed rCedV-HeV-GFP to escape neutralization by m102.4. Three G protein mutations, T117A, N186D, and T507I, permitted the chimeric virus to evade neutralization from the nAH1.3 and m102.4 mAb cocktail.

Figure 3.7 A HNV G head-directed mAb cocktail with synergistic neutralizing activity.

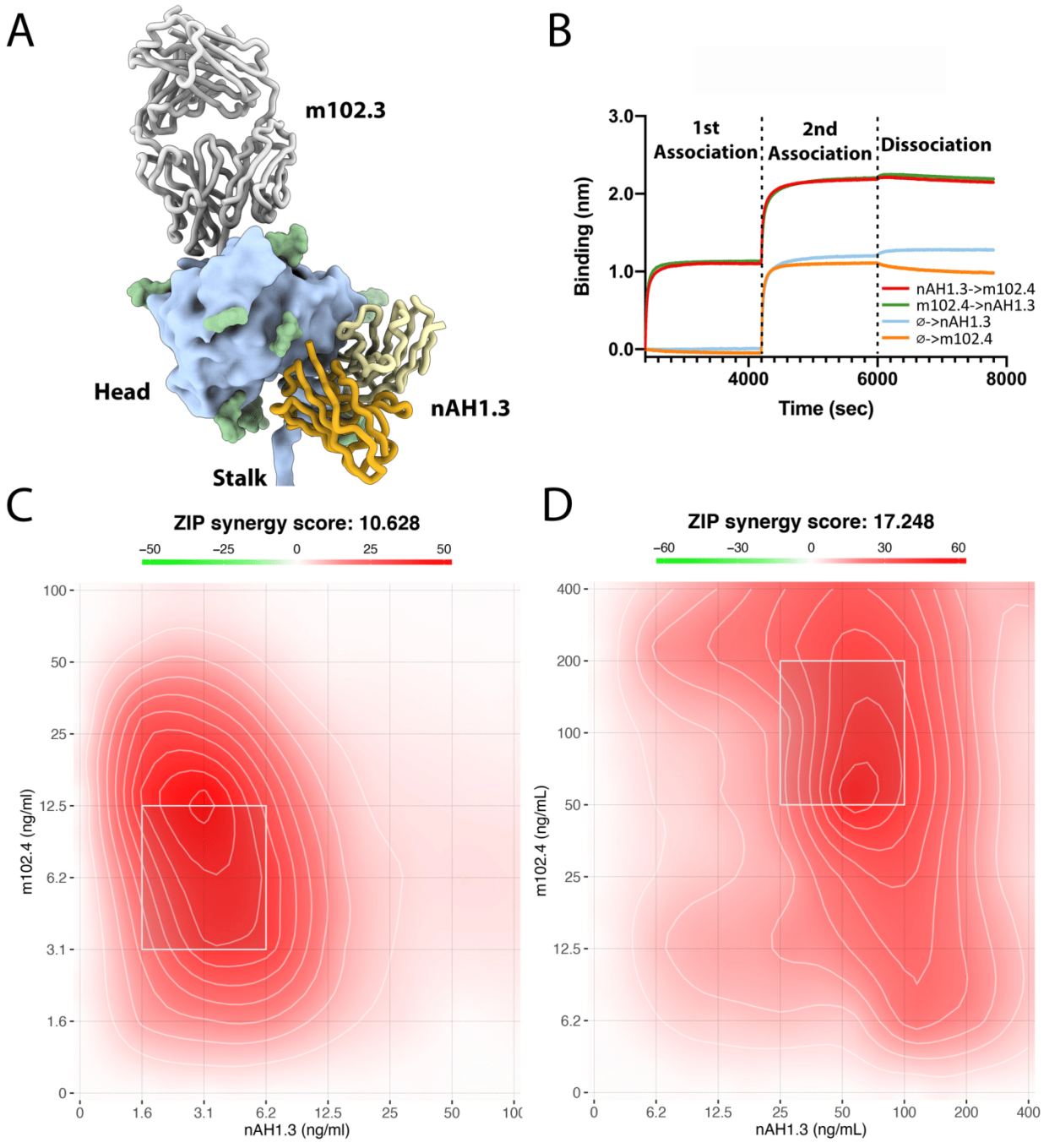

(**A**) Superimposition of the NiV G head domain (blue surface) bound to nAH1.3 (heavy and light chains colored gold and yellow, respectively) or to the m102.3 Fab (heavy and light chains colored dark and light gray, respectively; PDB ID 6CMI) showing

that they bind to opposite sides of the β propeller. m102.3 is closely related to the m102.4 mAb. (**B**) Biolayer interferometry analysis of binding of the nAH1.3 and m102.4 IgGs to the immobilized NiV G ectodomain showing absence of competition irrespective of the order of addition. Each NiV G loaded anti-penta-His biosensor probe was sequentially dipped in a solution containing 100 nM nAH1.3 IgG (red) and then 100 nM m102.4 IgG plus 100 nM nAH1.3 IgG (red) or 100 nM m102.4 IgG and then 100 nM of nAH1.3 IgG plus 100 nM m102.4 IgG (green). Controls with only nAH1.3 IgG (blue) or m102.4 IgG (orange) are shown for comparison. (**C** and **D**) Synergy maps for neutralization of replication-competent rCedV-NiV-B-GFP (**C**) and rCedV-HeV-GFP (**D**) by varying concentrations of the m102.4 and nAH1.3 mAb cocktail analyzed with SynergyFinder. ZIP synergy score >10 indicates a strong synergistic relationship. The white box indicates the most synergistic region on each plot.

Figure 3.8 EM characterization of the NiVG/m102.4/nAH1.3 complex and polyclonal epitope mapping.

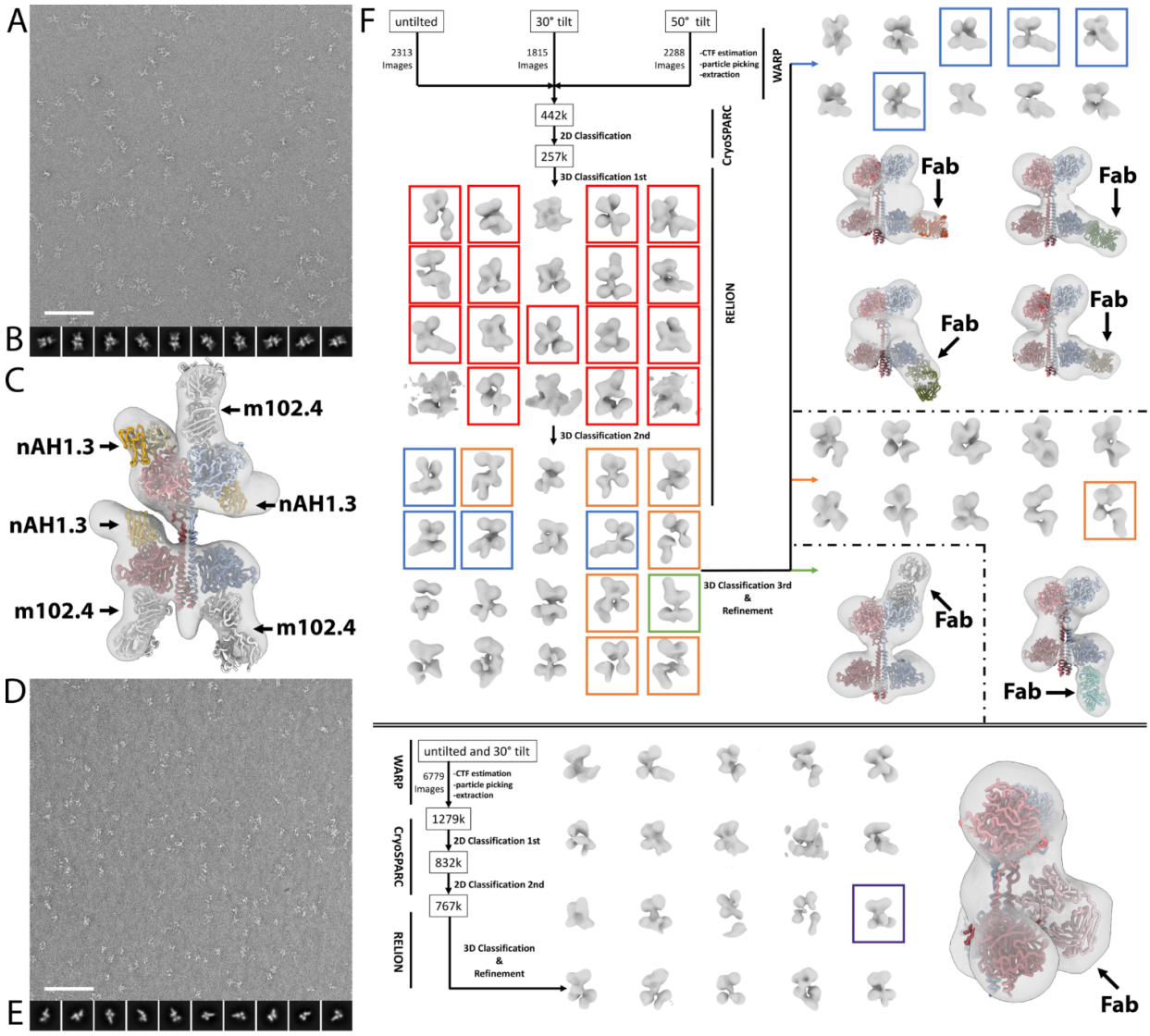

(**A-C**) Representative micrograph (**A**), 2D class averages (**B**) and 3D reconstruction (**C**) of the negatively stained complex between NiV G and the m102.4 and nAH1.3 Fab fragments. Scale bar: 1000Å. The map with the fitted model shows three nAH1.3 Fab (gold/yellow) and three m102.4 Fabs (grey) bound to NiV G (red/blue). (**D-F**) Representative micrograph (**D**), 2D class averages (**E**) and data processing flow chart (**F**) of the dataset of NiV G bound to purified polyclonal serum Fab fragments elicited by vaccination of rhesus macaques with an equimolar mixture of NiV G Bangladesh and Malaysia. The double bar separates the datasets obtained with Fabs purified from NHP 171269 (top) and from NHP 180227 (bottom). The latter data set

allowed identification of a stalk-directed Fab. Selected 3D classes from the first 3D classification of the NHP 171269 dataset have been highlighted with red boxes. Selected 3D classes from the second 3D classification of the NHP 171269 dataset have been assigned to three groups labeled by blue, orange and green boxes. The stalk binding class from the NHP 180227 dataset is highlighted with a purple box. The remaining classes from the NHP 180227 dataset were similar to those of the NHP 171269 dataset. Scale bar: 1000Å.

Figure 3.9 Evaluation of neutralization synergy and depletion study.

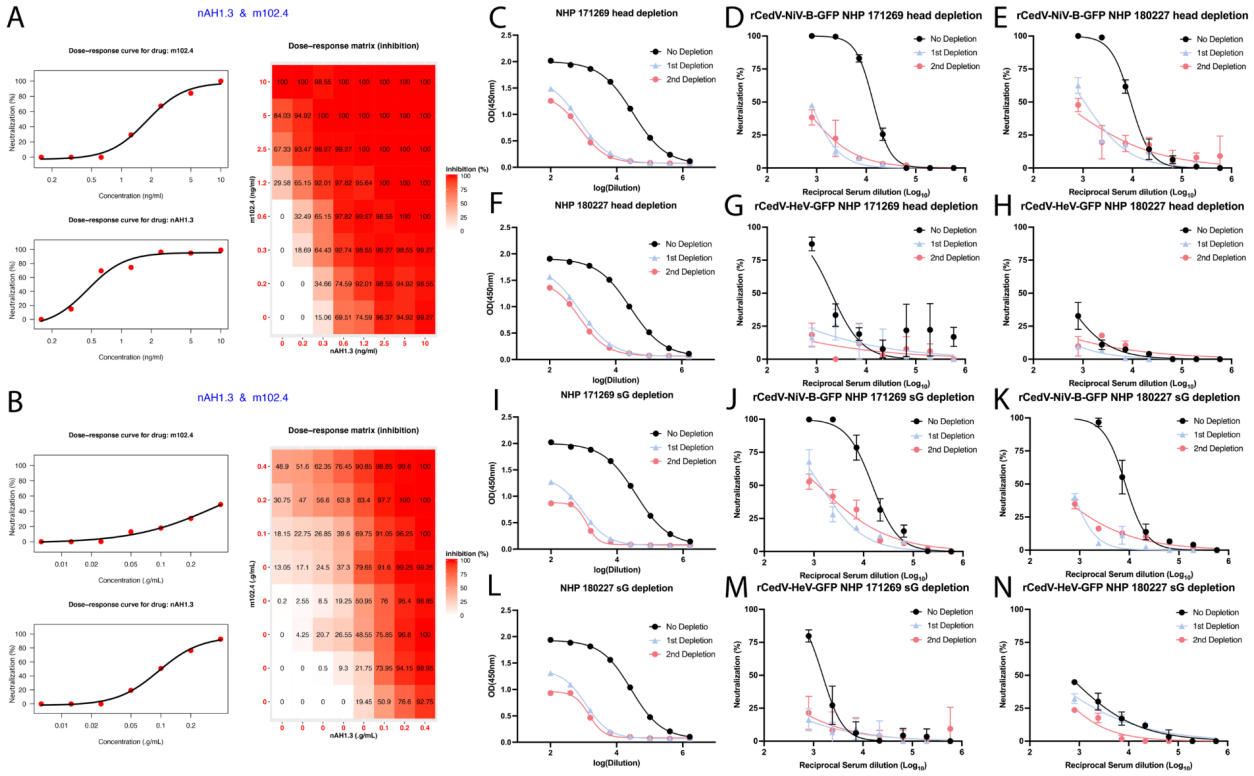

(**A**) Neutralization synergy of m102.4 and nAH1.3 against rCedV-NiV-B-GFP. (**B**) Neutralization synergy of m102.4 and nAH1.3 against rCedV-HeV-GFP. (**C**, **F**, **I**, **L**) Binding of various dilutions of rhesus macaque vaccine-elicited polyclonal Abs to the immobilized NiV sG ectodomain after head or ectodomain depletion analyzed by ELISA. (**D-E**) Evaluation of serum neutralizing activity against rCedV-NiVB-GFP before and after depletion of head-targeting Abs. (**G-H**) Evaluation of serum neutralizing activity against rCedV-HeV-GFP before and after depletion of head-targeting Abs. (**J-K**) Evaluation of serum neutralizing activity against rCedV-NiV-B-GFP before and after depletion of sG-targeting Abs. (**M-N**) Evaluation of serum neutralizing activity against rCedV-HeV-GFP before and after depletion of sG-targeting Abs.

Figure 3.10 The NiV G receptor binding head domain is immunodominant and accounts for most of the neutralizing activity elicited by vaccination.

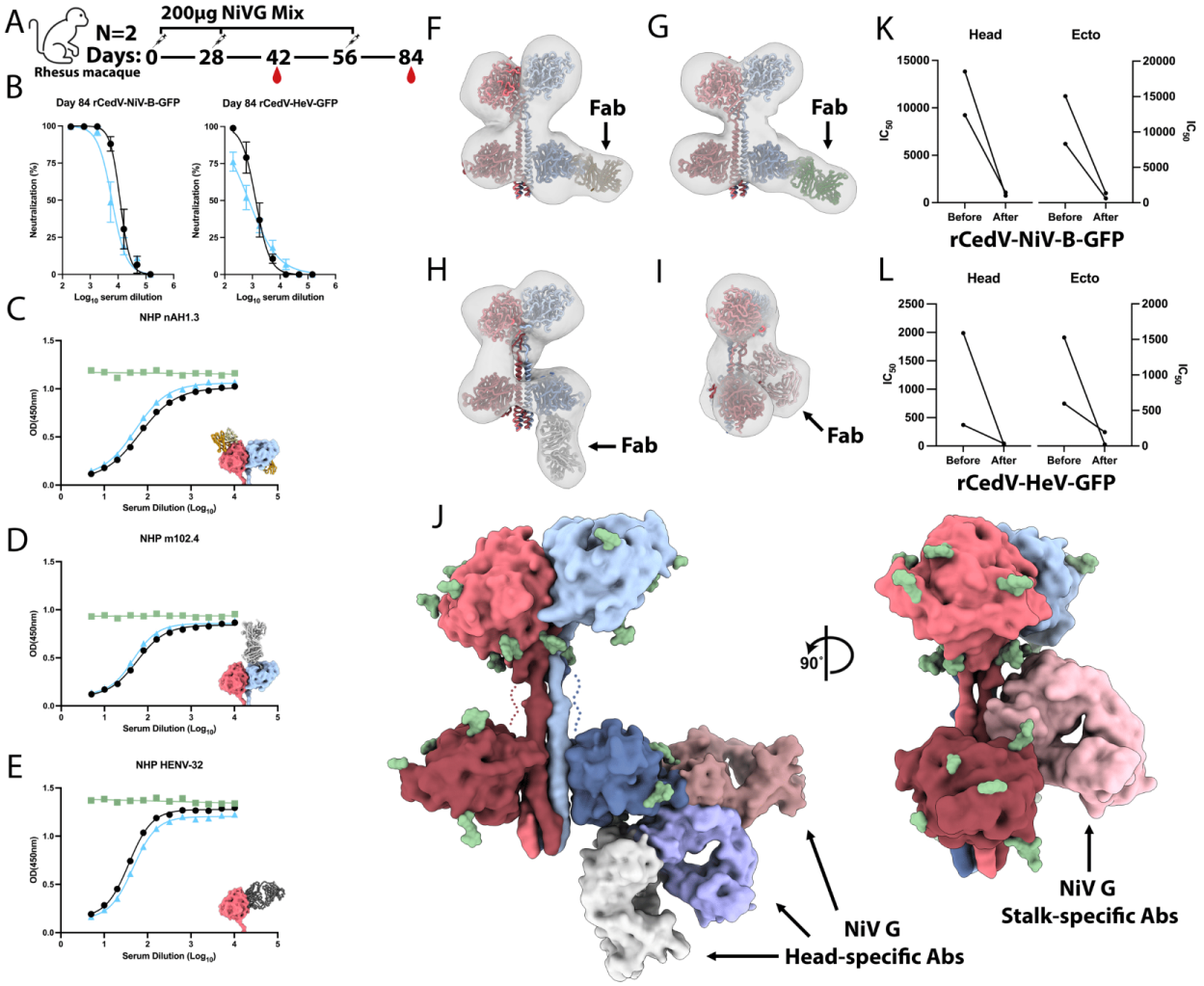

(**A**) Study design for vaccination of rhesus macaques, where two rhesus macaques have been immunized three times (4 weeks apart) with 200 µg of an alum-adjuvanted equimolar mixture of the purified NiV-B and NiV-M sG tetramers. Blood was collected on days 42 and 84 after immunization. (**B**) Serum neutralizing Ab titers against rCedV-NiV-B-GFP and rCedV-HeV-GFP measured on day 84. The curves for each animal are shown in black or blue. (**C** to **E**) Competition ELISAs showing binding of biotinylated nAH1.3 (**C**), m102.4 (**D**), and HENV-32 (**E**) mAbs to the immobilized NiV G ectodomain in the presence of various dilutions of vaccine-elicited rhesus macaque sera (obtained on day 84). The curves for each animal are shown in black or blue, whereas binding of the mAb in the absence of sera is shown in green (control). (**F-I**) Representative electron microscopy reconstructions (gray surfaces) of negatively

stained complexes formed between purified polyclonal serum Fab fragments and NiV G fitted with atomic models for visualization of antigenic sites targeted. (**J**) Surface representation of the NiV G tetramer with three head domain–specific Fabs bound (left) and a stalk-directed Fab bound (right), highlighting antigenic sites detected in vaccine-elicited polyclonal serum Abs. (**K** and **L**) Neutralizing Ab titers against rCedV-NiV-B-GFP (**K**) and rCedV-HeV-GFP (**L**) before and after depletion with the NiV G head domain (Head) or the ectodomain tetramer (Ecto).

Chapter 4. Potent monoclonal antibody–mediated neutralization of a divergent Hendra virus variant

This chapter highlights how structure information generated by single particle Cryo-EM can facilitate antibody drug discovery. Structure biology has been considered as the last molecular validation sole for a really long time. Here I present one polyclonal antibody cocktail discovery work, which shows how structure information is able to initiate application studies.

On the biological side, I proposed the concept of orthogonal epitopes, which are not only non-overlapping spatially but also independent in neutralizing mechanisms. To prove the concept, we suggested a tetravalent antibody cocktail and validated both by binding and neutralization experiments.

4.1 Background

A novel Hendra virus variant (HeV-g2) was detected in Australia in horses that succumbed to fatal HeV illness and in two species of flying foxes suffering vasculitis (*100*, *101*). Despite frequent HeV testing in horses in areas with known viral circulation in wildlife, this new HeV-g2 escaped routine PCR-based testing due to much lower sequence conservation than ever detected compared with prototypic HeV. Furthermore, HeV-g2 was detected in regions of Australia previously thought to be at low risk of HeV cross-species transmission (*100*, *101*). HeV-g2 F and G share 95.60 and 92.85% amino acid sequence identity with their counterparts in prototypic HeV, respectively.

Given the marked genetic divergence of HeV-g2 relative to HeV, it is unknown whether this newly discovered virus will share similar receptor usage and antigenic properties relative to prototypic HeV. Here, we set out to investigate the ability of HeV-g2 to utilize EB2 and EB3 as receptors for entry into cells and the likelihood that postexposure therapies and vaccines in development will be effective against this new variant. We show that several HNV F- and G-specific mAbs cross-react with HeV-g2 glycoproteins and inhibit entry into target cells. We identify and characterize a mAb cross-neutralizing HeV and HeV-g2, designated hAH1.3, and determined its structure bound to the HeV G head domain, revealing recognition of an antigenic site distinct from those targeted by all other known HNV G-reactive mAbs. These data delineate a path forward to deploy mAb mixtures with a high barrier to the emergence of escape mutants.

4.2 HeV-g2 and HeV Share a Conserved Receptor Tropism

Comparison of the HeV and HeV-g2 G sequences revealed that there are 33 residue substitutions between the two variants, most of them clustering within the receptor-binding G head domain (Figure 4.1). To understand the effect of these substitutions on receptor usage, we evaluated binding of purified monomeric HeV and HeV-g2 G head domains to immobilized EB2 and EB3 genetically fused to the human immunoglobulin 1 (IgG1) Fc fragment using biolayer interferometry (BLI). Despite the four residue differences between human EB2 (hEB2) and Pteropus alecto EB2 (PaEB2), both G head domain variants bound indistinguishably with monovalent binding affinities in the 0.5 to 1 nM range (Figure 4.2 A, B, D, E and 4.3 A-D). The strictly

conserved EB3 bound with comparable affinities to HeV and HeV-g2 G head domains, though affinities for EB3 were much lower than for EB2 (Figure 4.2 A, C, F, G and 4.3 E-H). These findings suggest that HeV-g2 recognizes each of the two known human receptor subtypes with similar efficiency to HeV, consistent with the strict conservation of the receptor-binding interface. Furthermore, the small number of (largely conservative) mutations found between hEB2 and PaEB2 and the strict conservation of hEB3 and PaEB3 (Figure 4.3) concur with the undistinguishable binding properties observed here across orthologs, supporting the role of flying foxes as reservoir hosts for both variants of HeV (and NiV).

To investigate the ability of HeV-g2 to utilize hEB2 and hEB3 for cell entry, we generated a green fluorescent protein (GFP)–encoding, replication-competent, Cedar (henipa)virus (rCedV) chimera in which the native glycoproteins are substituted with the HeV-g2 F and G glycoproteins (rCedV-HeV-g2-GFP). Stable expression of hEB2 (HeLa-USU-EB2) or hEB3 (HeLa-USU-EB3) rendered HeLa-USU cells susceptible to rCedV-HeV-g2-GFP, as was the case for the rCedV-HeV-GFP positive control which harbors the prototypical HeV F and G glycoproteins (Figure 4.2 H-I and 4.4) (*102*–*105*). We did not observe any significant differences in the percentage of GFP foci upon rCedV-HeV-g2-GFP infection of HeLa-USU-EB2 (91%) or HeLa-USU-EB3 (98%) cells compared with rCedV-HeV-GFP (set to 100%). No evidence of infection was observed in HeLa cells infected with either rCedV-HeV-g2-GFP or rCedV-HeV-GFP (Figure 4.4). Therefore, HeV-g2 retains the same receptor tropism as HeV and is expected to have a similar tissue tropism upon infection of humans and other animals.

4.3 Broadly Neutralizing HNV G-Specific mAbs Inhibit HeV-g2

Several G-targeted neutralizing mAbs have been described and shown to protect against lethal HeV and NiV challenge in a postexposure setting (*8*, *73*, *78*, *79*, *85*, *106*, *107*). Here, we investigated whether three potent and noncompeting neutralizing mAbs, m102.4, HENV-32, and nAH1.3, can cross-react with HeV-g2 G and neutralize rCedV-HeV-g2-GFP. Only 1 out of 33 residues that are mutated between HeV-g2 and prototypic HeV maps to an epitope recognized by one of these mAbs: The conservative R201K substitution is found within the HENV-32 binding site and recapitulates the NiV G K201 residue, explaining that HENV-32 broadly neutralizes NiV, HeV, and HeV-g2 (Figure 4.5 A-C) (*85*). Indeed, we found that m102.4 and HENV-32 bound to each variant indistinguishably whereas nAH1.3 recognized the two variants with roughly comparable efficiencies by BLI (Figure 4.5 D-F). Enzyme-linked immunosorbent assays (ELISAs) also indicated that each mAb has comparable affinity for the HeV and HeV-g2 G head domains, including the neutralizing mAbs HENV-103 and HENV-117 (Figure 4.6) (*78*). The neutralization potency of m102.4, HENV-32, and nAH1.3 was comparable against each of the two viruses (rCedV-HeV-g2-GFP and rCedV-HeV-GFP) with nAH1.3 exhibiting an order of magnitude greater neutralizing activity than the other two mAbs (Figure 4.5 G-I). These data show that broadly neutralizing HNV mAbs recognizing three distinct G head domain antigenic sites are potent inhibitors of the recently described HeV-g2 variant.

4.4 The hAH1.3 Neutralizing mAb Defines a HeV/HeV-g2 G Antigenic Site

The mouse hAH1.3 mAb was previously reported to potently neutralize HeV but not NiV (*73*). We determined a crystal structure of the hAH1.3 Fab fragment in complex with the HeV G head domain at 2.75-Å resolution (SI Appendix, Table S4). hAH1.3 interacts with an antigenic site located opposite of the head–head dimerization interface and thus of the HENV-32 epitope, which is also distinct from the receptor binding site or the nAH1.3 epitope (Figure 4.7 A) (*8*, *85*, *108*, *109*). As a result, hAH1.3 does not compete with the hEB2 receptor for binding to the HeV G head domain (as opposed to m102.4) and is unlikely to disturb the G head–head dimerization interface (in contrast to HENV-32) (Figure 4.7 A and 4.8). hAH1.3 binding does not induce major conformational changes of the HeV G head domain. All six hAH1.3 complementary determining regions participate in the paratope through shape complementarity and hydrogen bonding burying an excess of 1,000 Å2 at the interface with HeV G and involving contacts with the HeV G polypeptide and N-linked oligosaccharides at positions N378, N481, and N529 (Figure 4.7 B and 4.9). The sole residue substitution in the hAH1.3 epitope ($H_{HeV}386N_{HeV\text{-}g2}$) does not prevent cross-reactivity with both HeV and HeV-g2 head domains, as observed using BLI (Figure 4.7 C-D and 4.1, Table S2). Accordingly, hAH1.3 inhibited with comparable potencies rCedV-HeV-GFP (50% inhibitory concentration [IC50]: 25.47 ng/mL) and rCedV-HeV-g2-GFP (IC50: 22.07 ng/mL) (Figure 4.7 E). Although the structure suggests that the effect of individual NiV G substitutions within the hAH1.3 epitope relative to HeV G (I385T, H386K, K388Q, and

S483T) is expected to be moderate, the additive effect of all four mutations likely explains the lack of hAH1.3 cross-reactivity with NiV (Figure 4.7 C, F and 4.1).

4.5 Structure-Guided Formulation of a Tetravalent mAb Mixture

Superimposition of the m102.4-, HENV-32–, nAH1.3-, and hAH1.3-bound G structures indicated that the four mAbs target entirely distinct, nonoverlapping antigenic sites on HNV G (Figure 4.10 A). Using BLI, we confirmed that all four mAbs can simultaneously recognize the HeV or HeV-g2 G head domain immobilized at the surface of biosensors upon sequential incubation with combinations of these mAbs (Figure 4.10 B). Furthermore, an equimolar mixture of all four mAbs mediated potent, concentration-dependent inhibition of both rCedV-HeV-GFP and rCedV-HeV-g2-GFP (Figure 4.10 C). Given that HENV-32 recognizes an antigenic site buried at the interface between G protomers and based on steric considerations, it is possible that binding of the four-mAb mixture would disrupt G tetramers, as observed with some coronavirus mAbs, possibly contributing to neutralization. These data delineate a path forward for deploying multivalent mAb combinations for postexposure treatment that would pose a higher barrier to the emergence of escape mutants than individual constituting mAbs (*8*).

To further evaluate the possible effects of the HeV-g2 G amino acid sequence variation on its antigenic landscape, we measured the neutralizing activity of rhesus macaque polyclonal sera elicited by immunization with equimolar concentrations of NiV-Malaysia sG and NiV-Bangladesh sG (*8*). We determined serum neutralizing activities of 1/578 and 1/894 against rCedV-HeV-GFP and rCedV-HeV-g2-GFP,

respectively, for one animal, and of 1/242 and 1/714 against rCedV-HeV-GFP and rCedV-HeV-g2-GFP, respectively, for the second animal (Figure 4.10 D-F). In both cases, the sera are slightly more potent against HeV-g2 than HeV (vaccine-mismatched) but less than NiV (vaccine-matched), for which the neutralizing activity was 1/11,785 and 1/6,036 (*8*). The comparable vaccine-elicited neutralizing antibody responses against HeV-g2 and HeV indicate that the changes in HeV-g2 G do not dampen polyclonal serum neutralizing activity.

4.6 Discussion

Since its discovery in 1994, 65 spillovers of HeV to domestic horses have been detected in Australia with sporadic human exposure and disease. A new HeV variant, termed HeV-g2, was recently described from two independent discoveries: one from a retrospectively diagnosed horse succumbing to henipaviral disease in 2015, which enabled a second fatal equine case to be diagnosed in October 2021, and the other from a long-term effort to monitor and survey the flying fox population in different states of Australia (*100*). The HeV-g2 genome differs from that of the prototypic HeV sufficiently to have failed detection by real-time RT-PCR–based disease surveillance in horses and viral reservoir surveillance of flying foxes. The identification of HeV-g2 extends the known HNV genetic diversity and also highlights the broad geographical range of potential HeV spillover.

We show here that HeV-g2 retains the same receptor tropism as prototypic HeV and utilizes EB2 and EB3 as bona fide entry receptors. Moreover, a panel of nine mAbs targeting several epitopes on the HeV G glycoprotein cross-reacts and retains potent

neutralizing activities against HeV-g2. We describe a mAb, designated hAH1.3, cross-reacting with HeV and HeV-g2 G by targeting an antigenic site which is conserved among HeV variants but not NiV. As the epitopes of the hAH1.3, m102.4, HENV-32, and nAH1.3 neutralizing mAbs are distinct, we formulated a tetravalent mAb mixture potently neutralizing HeV and HeV-g2 which is expected to have a much higher barrier for the emergence of escape mutants relative to individual constituting mAbs (*8*). Our data support the clinical development of multivalent mAb mixtures for postexposure therapy as such countermeasures are expected to retain broad neutralizing activity against known and unknown NiV and HeV variants. NiV sG subunit vaccine-elicited neutralizing antibody responses are equivalently potent against HeV and HeV-g2, indicating that this newly emerged HeV-g2 variant does not erode cross-neutralizing polyclonal antibody responses more than HeV. We expect these findings to hold true in horses vaccinated with Equivac HeV and in humans, as the only HNV vaccine in clinical development is based on HeV sG which elicits better cross-protective titers than NiV sG against heterotypic challenge in animals (*13*). Collectively, our data provide a comprehensive assessment of available countermeasures against this newly described HeV-g2 variant and delineate multiple strategies for pandemic preparedness.

4.7 Figures & Tables

Figure 4.1 Sequence conservation between HeV and HeV-g2 G and F glycoproteins.

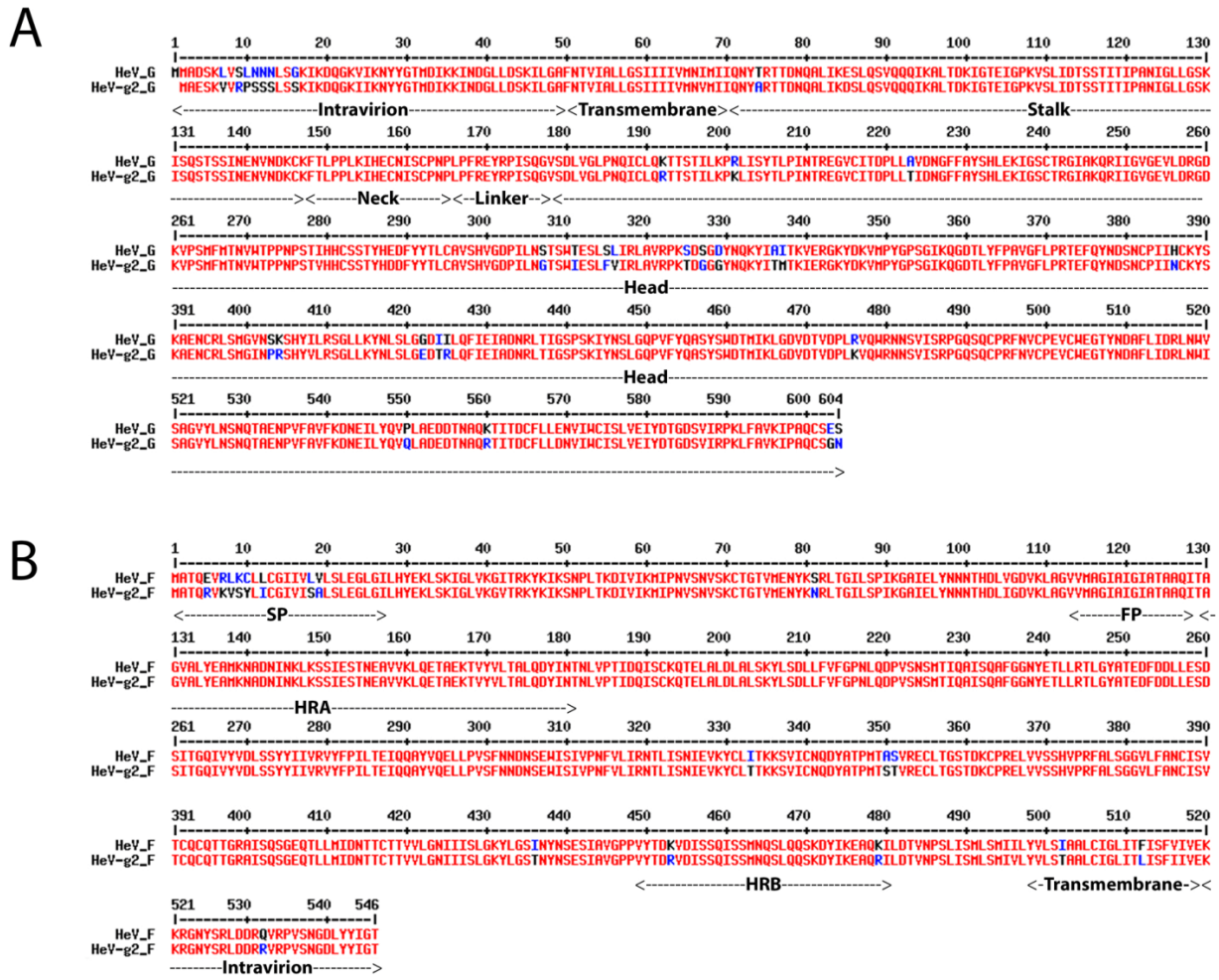

(**A**) Sequence alignment between HeV and HeV-g2 G glycoproteins. (**B**) Sequence alignment between HeV and HeV-g2 F glycoproteins. SP, signal peptide; FP, fusion peptide; HRA/B, heptad repeats A/B.

Figure 4.2 HeV and HeV-g2 share a conserved receptor tropism.

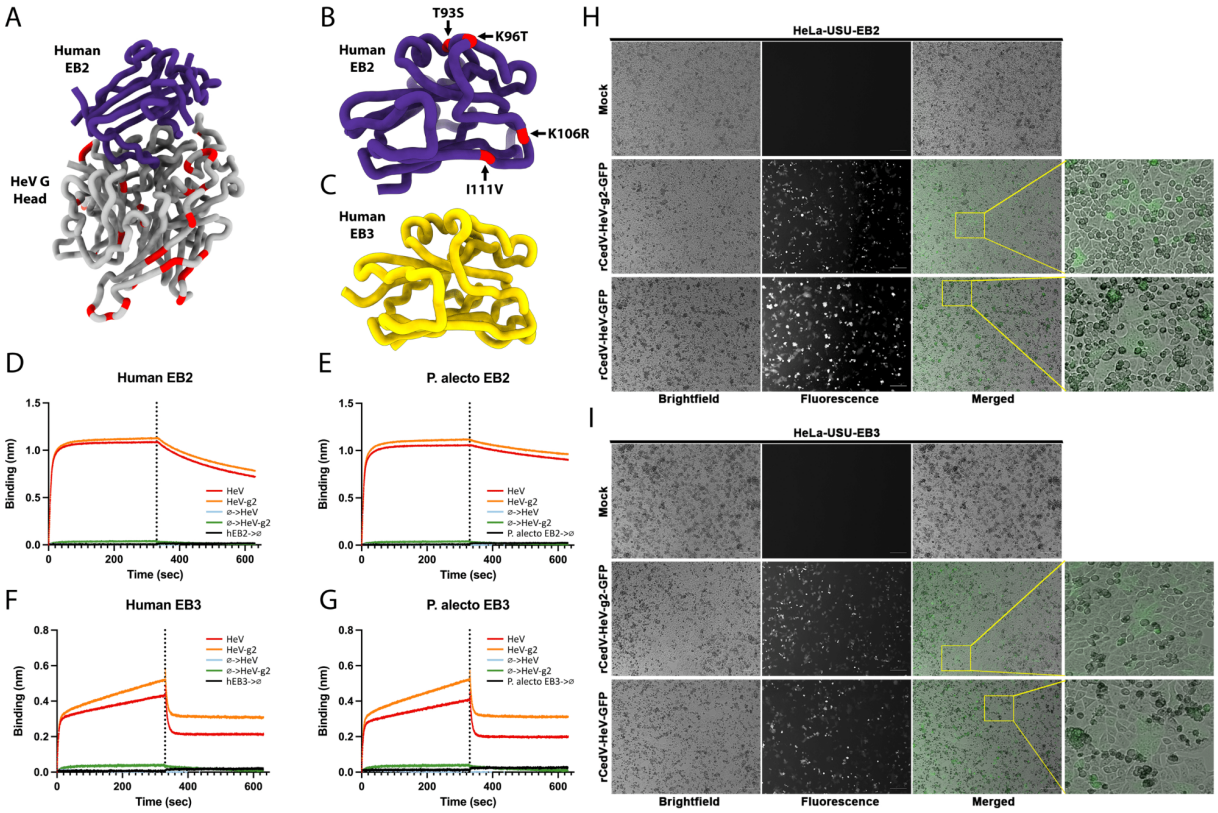

(**A**) Ribbon diagram of a HeV G head domain (gray) in complex with human EB2 (purple). Residues mutated between the HeV G and HeV-g2 G head domains are colored red. The rendering was made using PDB ID code 6PDL. (**B** and **C**) Ribbon diagram of human EB2 (**B**; PDB ID code 6PDL) and EB3 (**C**; PDB ID code 3D12). Residues that differ between human and P. alecto orthologs are colored red. (**D-G**) BLI binding analysis of 200 nm HeV (red) or HeV-g2 (orange) G head domain to immobilized human EB2-Fc (**D**), P. alecto EB2-Fc (**E**), human EB3-Fc (**F**), or P. alecto EB3-Fc (**G**). All ephrin-Fc fusions were immobilized on AHC biosensors. (**H** and **I**) EB2 and EB3 are entry receptors for rCedV-HeV-g2-GFP. (Scale bars, 50 μm.) (**H** and **I**, Insets) Zoomed-in regions within the yellow boxes. Bright-field, fluorescence, and merged images are shown (Left to Right).

Figure 4.3 Biolayer interferometry evaluation of receptor binding.

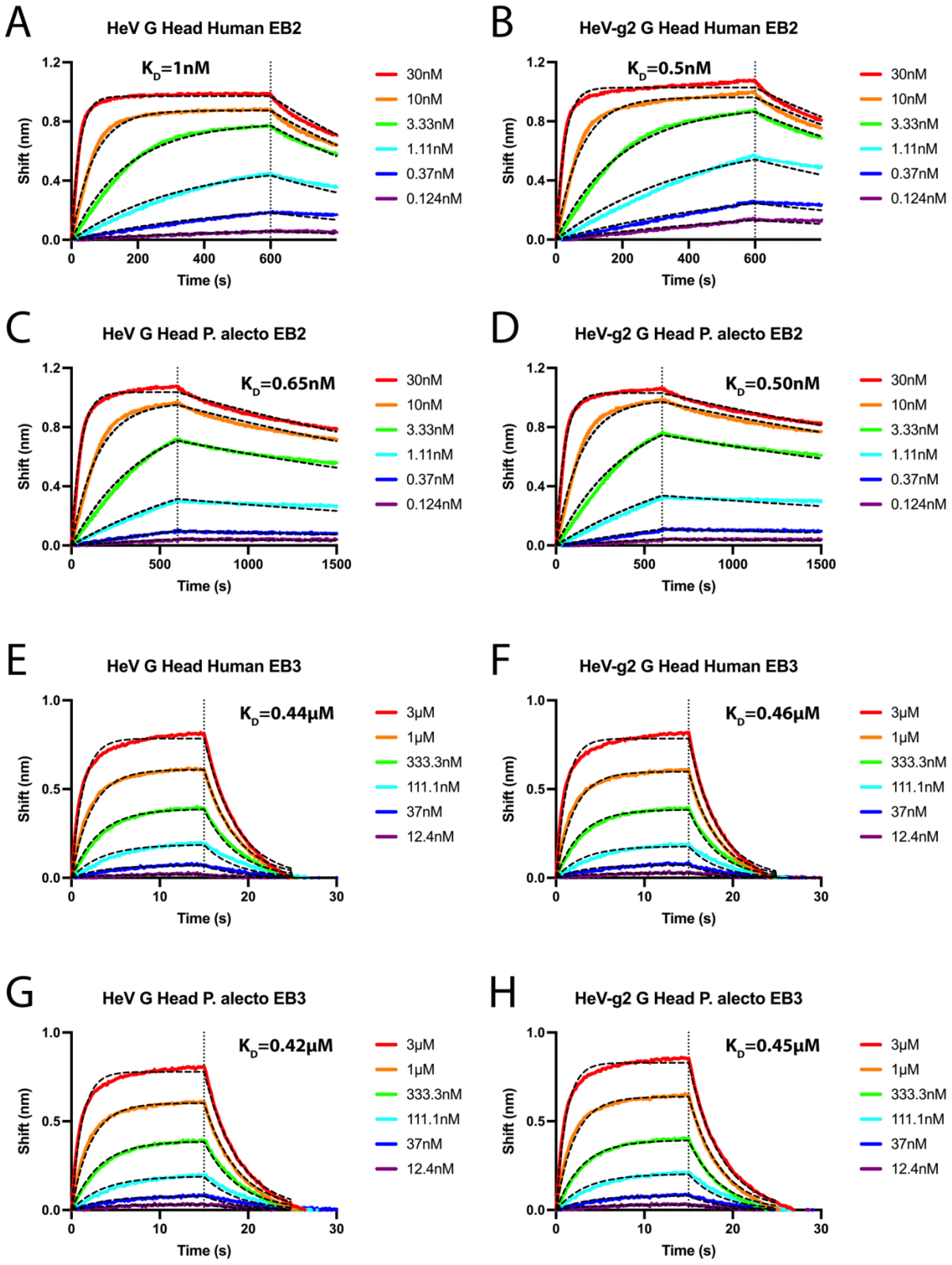

(**A-D**) Biolayer interferometry analysis of binding of the HeV/HeV-g2 G head domain to immobilized human/P. alecto EB2-Fc. (**E-H**) Biolayer interferometry analysis of binding of HeV/HeV-g2 G Head domain to immobilized 4 human/P. alecto EB3-Fc. Black traces show the fit to the data using a 1:1 global model. The vertical dashed line corresponds to the transition between association and dissociation phases.

Figure 4.4 Assessment of ephrin receptor tropism.

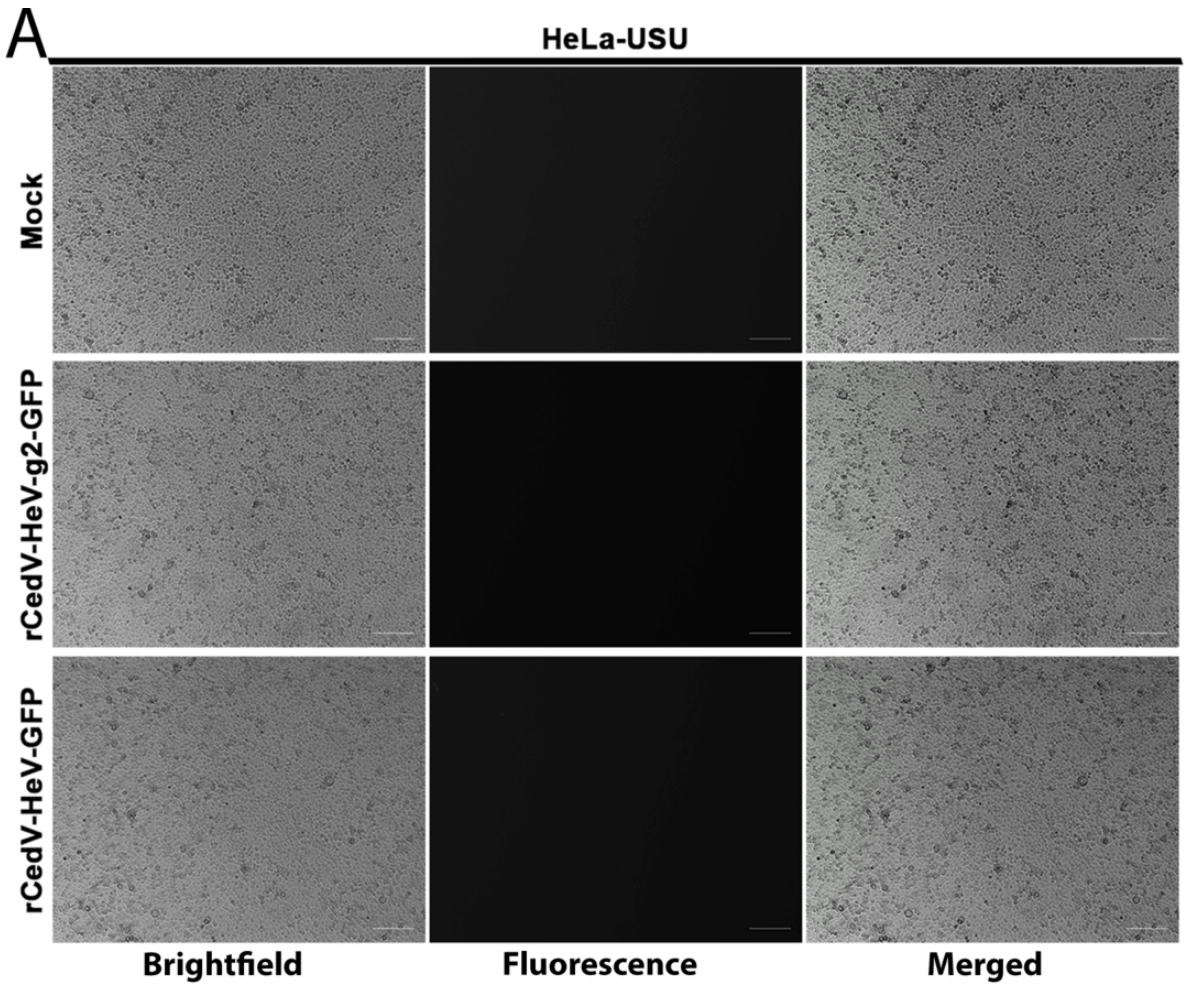

(**A**) The HeLa-USU cell line does not express EB2 or EB3, and is thus not permissive to rCedV-HeV-GFP or rCedV-HeV-g2-GFP entry. Brightfield, fluorescence and merged images are shown (left to right).

Figure 4.5 Broadly neutralizing HNV G-specific mAbs inhibit HeV-g2.

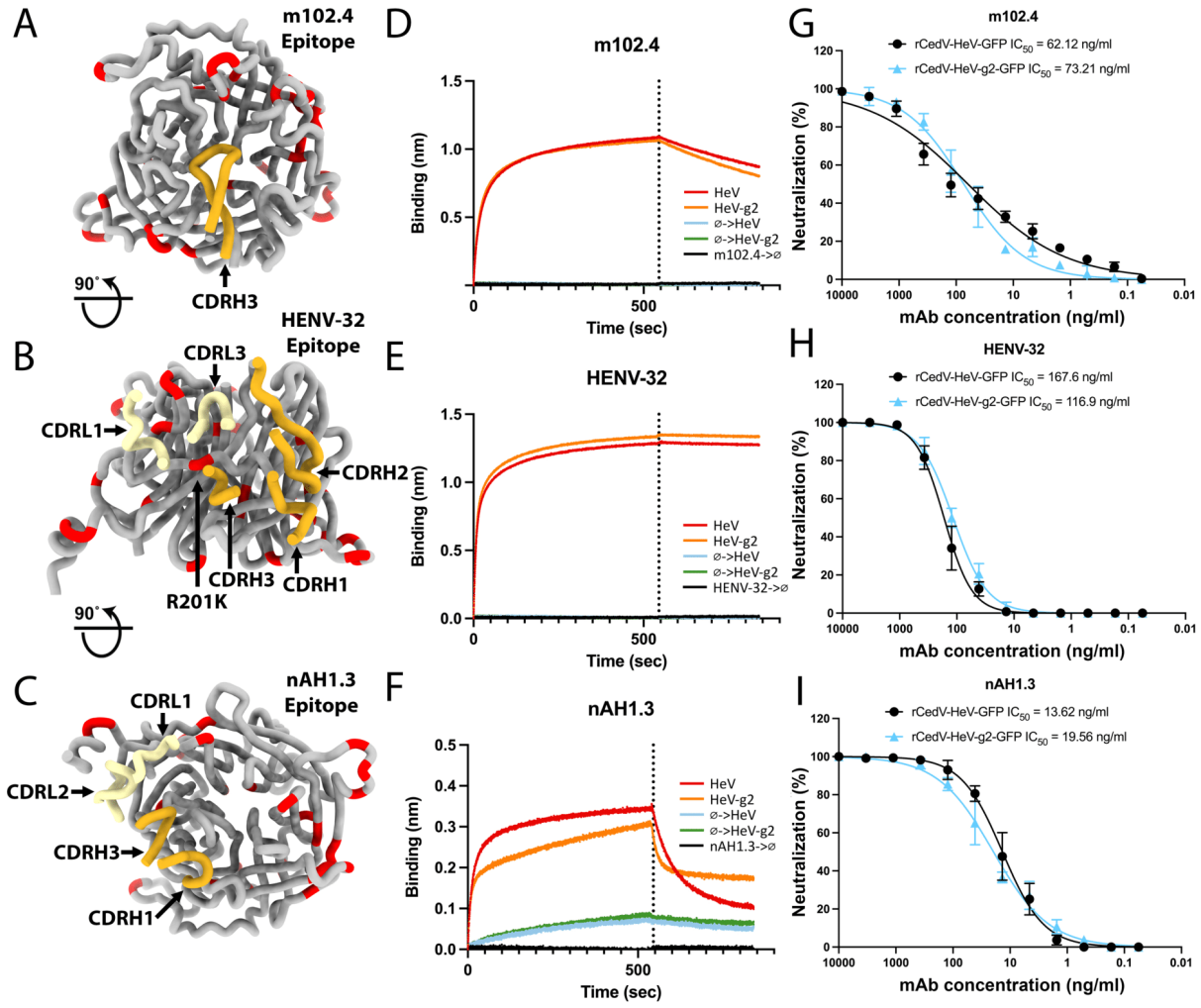

(**A-C**) Ribbon diagram of the HeV G head domain (gray) with the interacting heavy- and light-chain complementarity-determining regions (CDRs) of m102.3 (parent mAb of m102.4; PDB ID code 6CMI) (**A**), HENV-32 (PDB ID code 6VY4) (**B**), and nAH1.3 (PDB ID code 7TXZ) (**C**) rendered in gold and yellow, respectively. Residues that are mutated in HeV-g2 G relative to HeV G are colored red. (**D-F**) BLI binding analysis of 100 nm HeV (red) or HeV-g2 (orange) G head domain to m102.4 (**D**), HENV-32 (**E**), or nAH1.3 (**F**) IgG immobilized at the surface of AHC biosensors. (**G-I**) m102.4- (**G**), HENV-32– (**H**), and nAH1.3-mediated (**I**) neutralization of rCedV-HeV-GFP (black) or rCedV-HeV-g2-GFP (blue). The limit of detection for the neutralization assay was 50 fluorescent foci. The differences of IC_{50} values for each mAb between rCedV-HeV-GFP and rCedV-HeV-g2-GFP were not statistically significant (Student's t test) with P values of 0.447, 0.609, and 0.117 for m102.4, HENV-32, and nAH1.3, respectively. Error bars: SD. Moreover, we observed Pearson correlations of 0.9819,

0.9942, and 0.9909 for the m102.4, HENV-32, and nAH1.3 IC_{50} values, respectively, between rCedV-HeV-GFP and rCedV-HeV-g2-GFP with P values smaller than 0.0001.

Figure 4.6 Enzyme-linked immunosorbent assays of G-directed mAb binding.

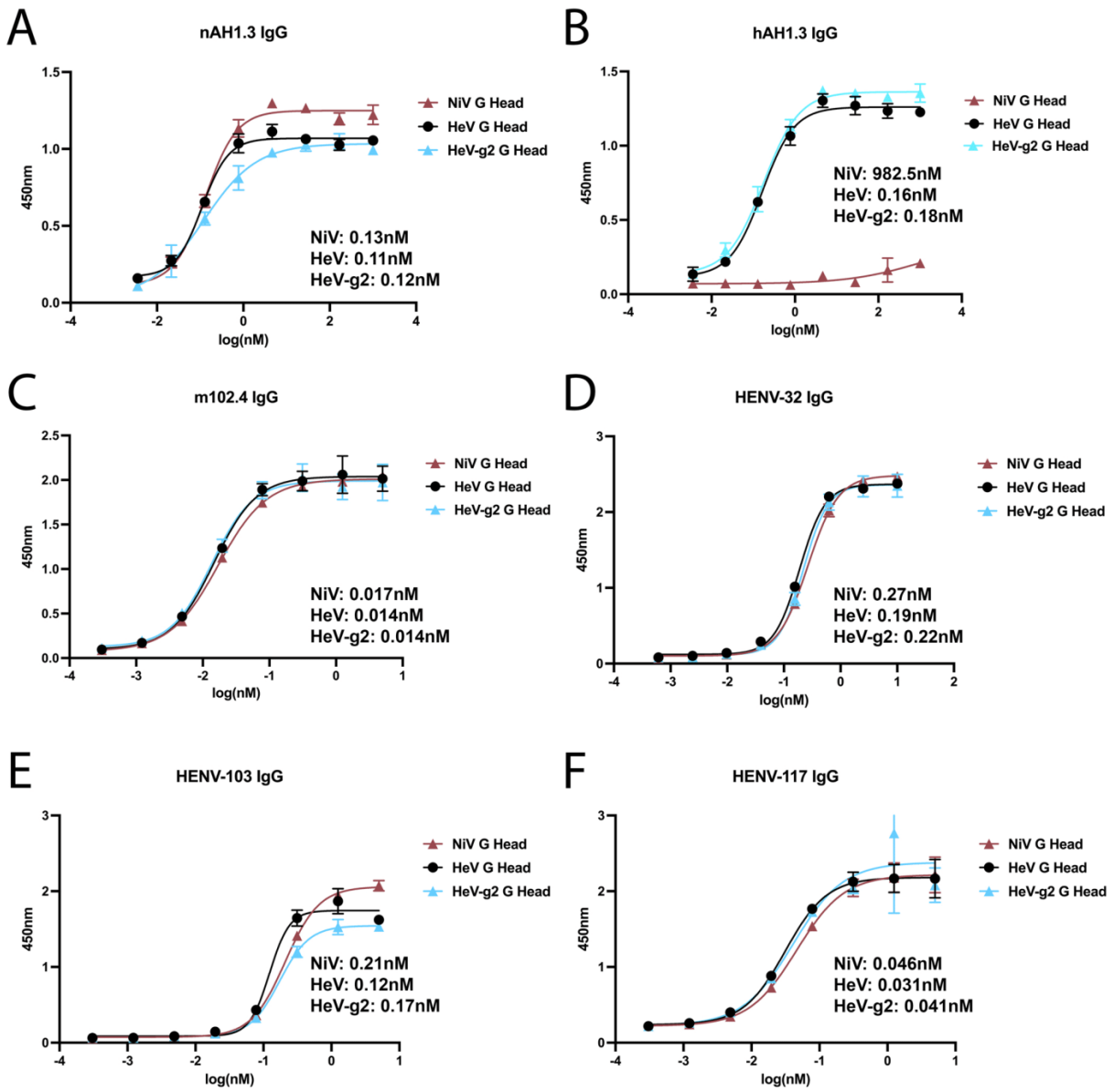

(**A-F**) immobilized nAH1.3 (**A**), hAH1.3 (**B**), m102.4 (**C**), HENV-32 (**D**), HENV-103 (**E**) and HENV-117 (**F**) IgGs binding to various concentrations of NiV G (cyan), HeV G (red) and HeV-g2 G (blue) head domains. The determined EC_{50} values for each G head domain are provided.

Figure 4.7 hAH1.3 cross-reacts with and neutralizes HeV and HeV-g2.

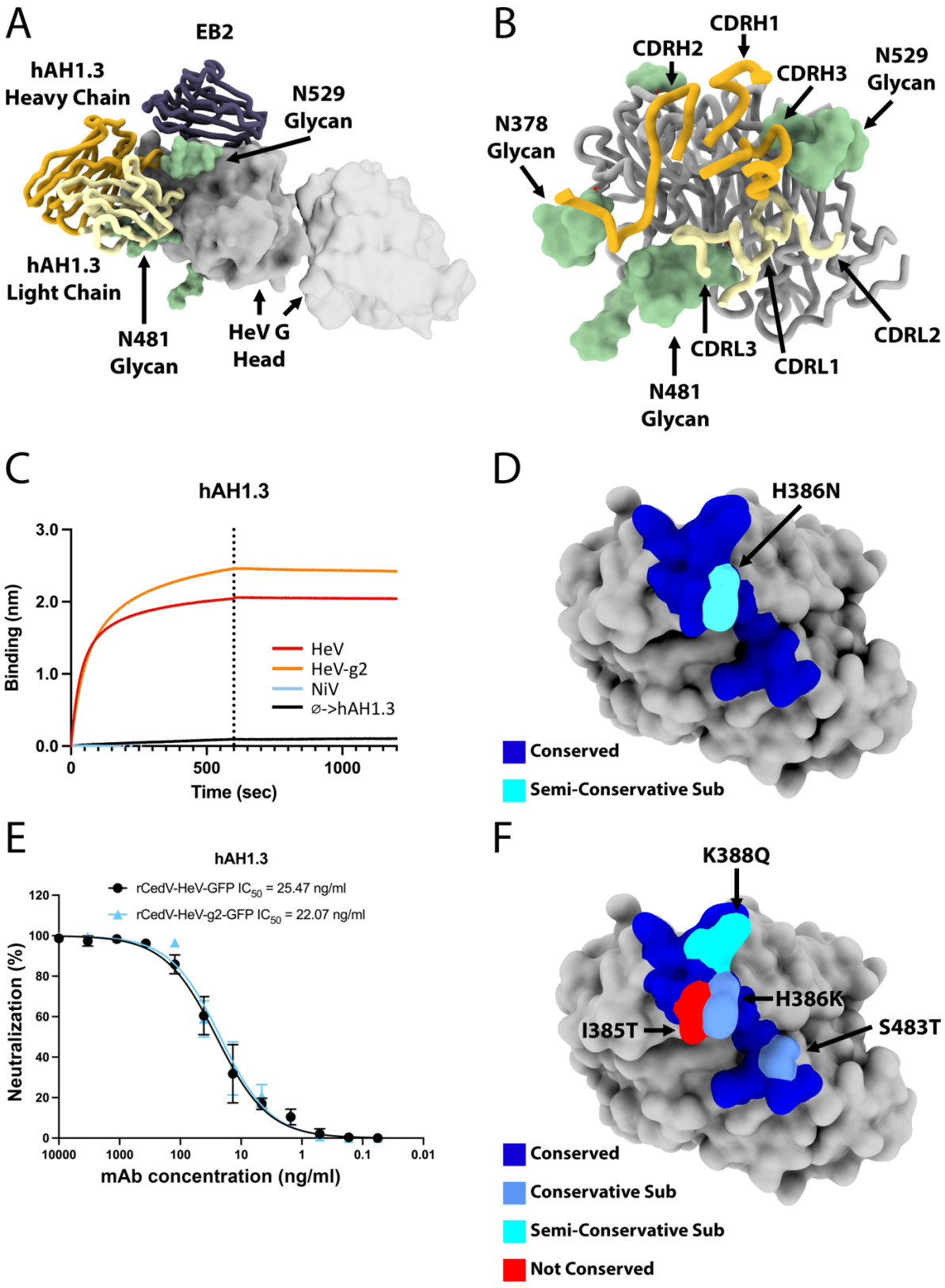

(**A**) Superimposition of the HeV G head domain (gray surface) bound to hAH1.3 (heavy and light chains are colored gold and yellow, respectively) with the EB2-bound NiV G head structure (purple; PDB ID code 2VSM; only EB2 is shown for clarity) showing the epitope does not overlap with the receptor binding site or the dimerization interface (transparent volume indicating the neighboring G head domain in the tetramer; PDB ID code 7TXZ). N-linked glycans are rendered as green surfaces. (**B**) Ribbon diagram of the HeV G head domain (gray) with the interacting hAH1.3 heavy- and lightchain CDRs rendered in gold and yellow, respectively. (**C**) BLI binding analysis of 100 nm hAH1.3 IgG to immobilized HeV G, HeV-g2, or NiV G head domains. (**D**) Molecular surface representation of the HeV G head showing the hAH1.3 footprint colored by residue conservation between HeV G and HeV-g2 G. Semi-Conservative sub, semiconservative substitution. (**E**) hAH1.3- mediated neutralization of rCedV-HeV-GFP (black) or rCedV-HeV-g2-GFP (blue). The limit of detection for the neutralization assay was 50 fluorescent foci. The hAH1.3 IC50 values were not statistically different (Student's t test) between rCedV-HeV-GFP and rCedV-HeV-g2-GFP ($P = 0.736$). Moreover, we observed a Pearson correlation of 0.9974 for the hAH1.3 IC50 values between rCedV-HeV-GFP and rCedV-HeV-g2-GFP with P values smaller than 0.0001. Error bars: SD. (**F**) Molecular surface representation of the HeV G head showing residue differences between HeV and NiV within the hAH1.3 epitope. Conservative sub, conservative substitution. Semi conservative sub, semi-conservative substitution.

Figure 4.8 Competition biolayer interferometry analysis of binding of the hAH1.3 Fab and EB2 to the immobilized HeV G head domain.

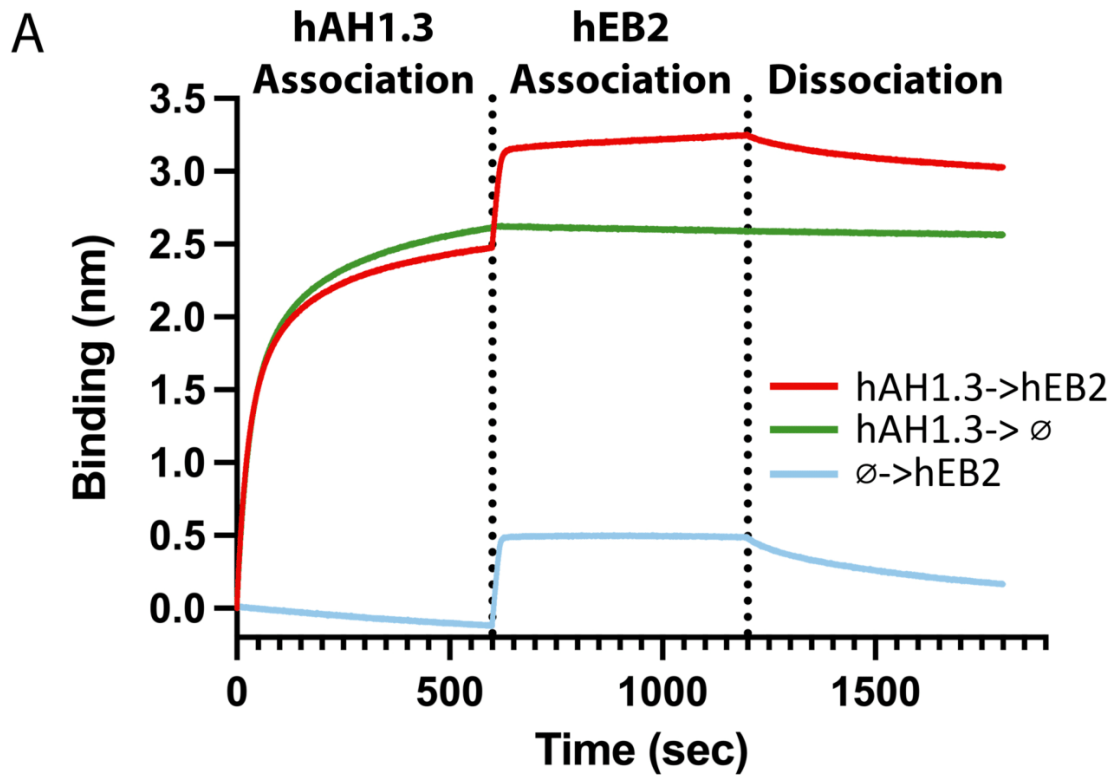

(**A**) Each HeV G head loaded Ni-NTA biosensor probe was sequentially dipped in a solution containing 100 nM hAH1.3 IgG (red) and then 250 nM hEB2 + 100 nM hAH1.3 IgG (red). Controls with only hAH1.3 IgG (green) or hEB2 (blue) are shown for comparison. No competition was observed.

Figure 4.9 Close-up view of the hAH1.3 epitope and representative electron density.

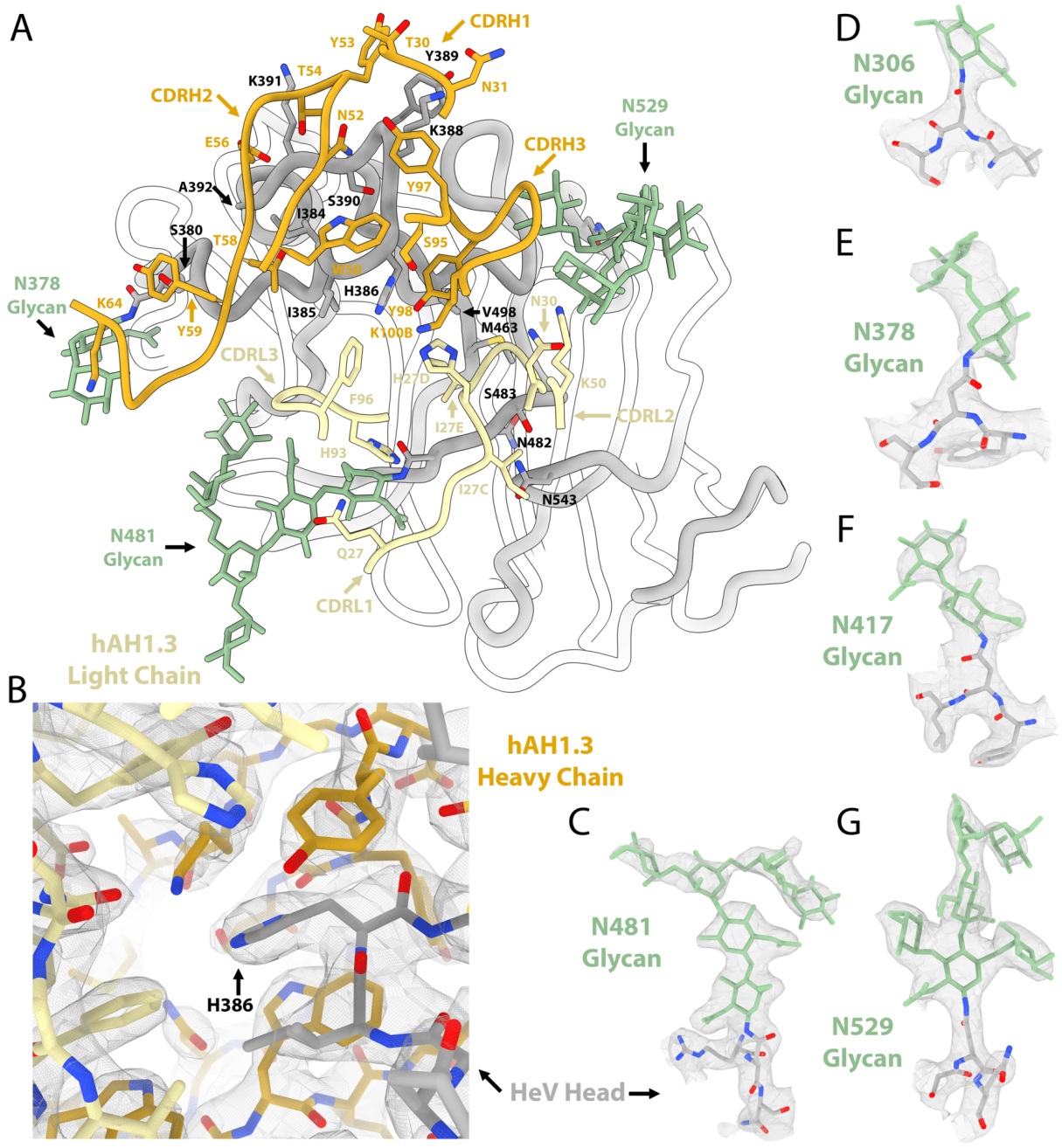

(**A**) Zoomed-in view of the interface between HeV G and hAH1.3 with selected side chains shown as sticks. The HeV G head domain is rendered in gray whereas the hAH1.3 heavy and light chains are colored gold and yellow, respectively. (**B**) Zoomed-in view around HeV G residue H386 with 2Fo-Fc electron density shown as gray mesh

contoured at approximately 2**σ**. (**C-G**) HeV G head N-linked glycans with 2Fo-Fc electron density shown as gray mesh.

Figure 4.10 G-targeted tetravalent mAb mixture and vaccine-elicited antibodies broadly neutralize HeV-g2.

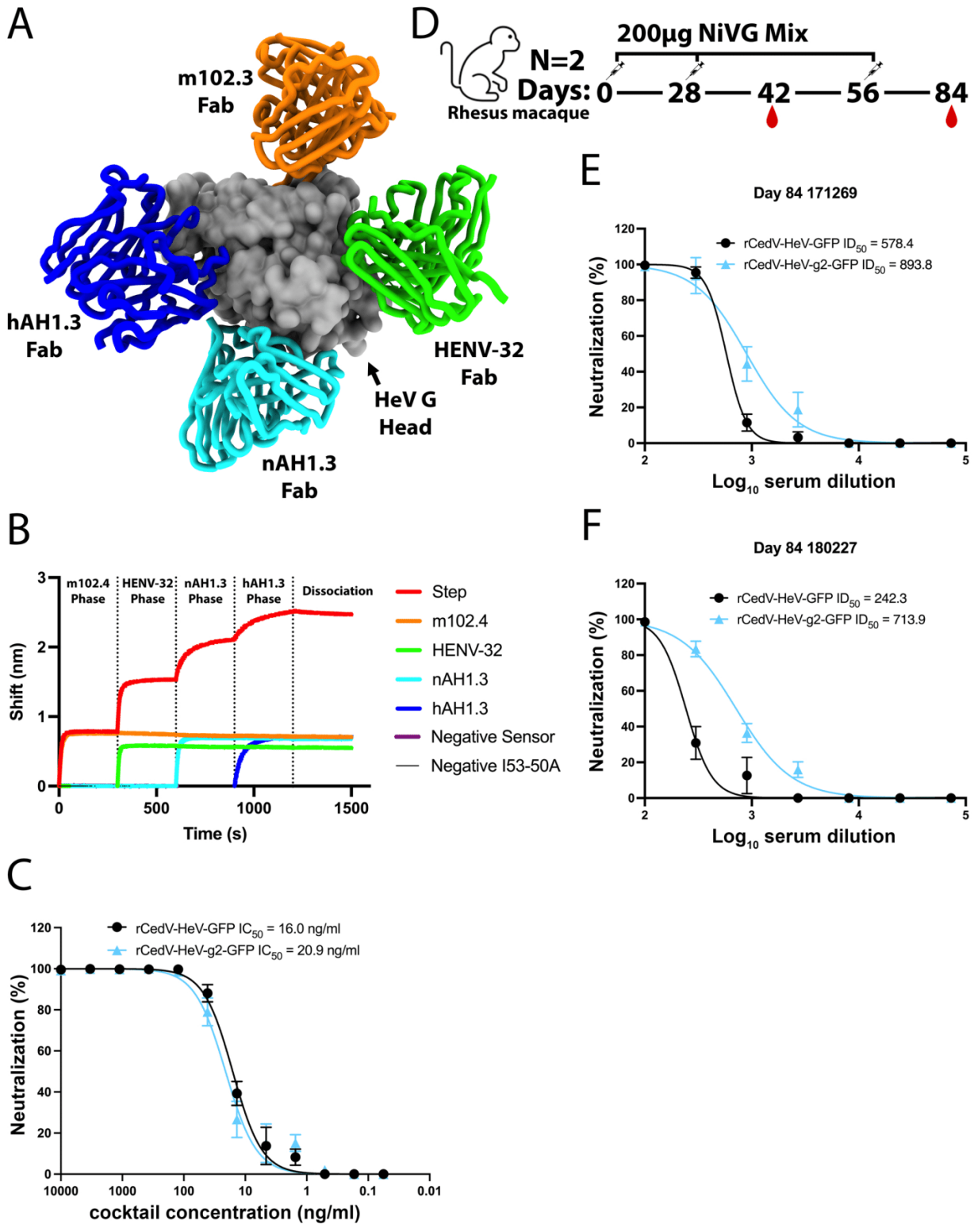

(**A**) hAH1.3 (blue), m102.3/m.102.4 (green), nAH1.3 (pink), and HENV-32 (red) mAbs recognize nonoverlapping epitopes on the HeV G head (gray). The HeV G head is rendered in the same orientation as in Fig. 4A, where the head–head dimerization interface faces to the right and the receptor-binding interface faces to the top. (**B**) BLI analysis of binding of m102.4, HENV-32, nAH1.3, and hAH1.3 IgG to the immobilized HeV G head showing the absence of competition among mAbs. The red trace shows the HeV G head-I53-50A fusion–loaded anti–penta-His biosensor sequentially dipped into a solution containing 100 nm m102.4, followed by 100 nm m102.4 + 100 nm HENV-32, followed by 100 nm m102.4 + 100 nm HENV-32 + 100 nm nAH1.3, followed by 100 nm m102.4 + 100 nm HENV-32 + 100 nm nAH1.3 + 100 nm hAH1.3, and buffer alone. Controls with only m102.4 IgG (orange), HENV-32 IgG (green), nAH1.3 IgG (cyan), and hAH1.3 IgG (blue) are shown for comparison. Negative sensor refers to an uncoated anti–penta-His biosensor dipped into 100 nm m102.4 + 100 nm HENV-32 + 100 nm nAH1.3 + 100 nm hAH1.3, and negative I53-50A refers to the HeV G head-I53-50A fusion–loaded anti–penta-His biosensor dipped into buffer alone. (**C**) Neutralization of rCedV-HeV-GFP (black) or rCedV-HeV-g2-GFP (blue) by the tetravalent m102.4/HENV-32/nAH1.3/hAH1.3 mAb mixture (1:1:1:1 molar ratio). (**D**) Study design for vaccination of rhesus macaques. Two animals were immunized three times (4 wk apart) with 200 μg of an alum-adjuvanted equimolar mixture of the purified NiV-B and NiV-M sG tetramers. Sera were collected on day 42 and day 84 postimmunization. (**E**) Day 84 NHP 171269 serum neutralizing activity against rCedV-HeV-GFP (black) and rCedV-HeV-g2-GFP (blue). (**F**) Day 84 NHP 180227 serum neutralizing activity against rCedV-HeV-GFP (black) and rCedV-HeV-g2-GFP (blue). The limit of detection for the neutralization assay was 50 fluorescent foci. Error bars: SD.

Chapter 5. Core wall structure and organization of Vaccinia virus

This chapter highlights how Cryo-ET and subtomogram average can capture intermediate resolution electron volume maps of organized protein complexes without macroscale symmetry. To validate this idea, here I achieve a medium resolution (~10Å) electron volume map on one component of the Vaccinia virus core wall complexes. With the current advance in structure prediction, preliminary evidence has shown that A10L 1-614 in the form of 213kDa trimer (71kDa each monomer), could be the potential candidate for the spike layer. Unlike non-enveloped viruses whose capsid wall usually has high marcolevel symmetry, Vaccinia virus is an enveloped virus with no symmetry, where its core wall is an organized multi-protein layer with no global symmetry.

On the biological side, this is the first detailed observation of the orthopoxvirus core wall. This is the first time that we observed the core wall complex at near molecular level, and it is also the first time we localized and oriented the previously suggested core wall proteins. This work in progress bears the promise of revealing the detailed organization of the core wall and to not only give us biological information about the Vaccinia virus architecture, but to also give us hints for drug design targeting anti-core wall formation .

5.1 Background

Vaccinia virus (VACV) is the prototype orthopoxvirus in the Poxviridae family, which contains a 190 kbp large DNA genome that replicates and assembles entirely in

the cytoplasm of the host cell. This large genome encodes 263 potential open reading frames leading to the production of more than 100 proteins that are associated with viral assembly in specific cytoplasmic areas named viral factories or virosomes (*19*, *110*–*112*). VACV morphogenesis has always been a good study target for electron microscopy, and quite detailed information about viral assembly has been obtained (*19*, *113*–*118*). Based on this information, a viral life cycle was proposed where the virus assembly starts within virosomes initiated by the formation of crescent-shaped membranes; the membranes then enclose electron-dense material from the virosomes and form initial virions, so-called immature virion (IV); IV will further mature inside the host cytoplasm and transform into soap bar-shaped intracellular mature virion (IMV) where the envelope surrounds a broad bean-like core with viral DNA inside; most IMVs will directly release from host cell as mature virion (MV) while a small amount will be packed with another envelope layer by trans-Golgi network as enveloped virion (EV) (*19*, *119*).

Between IV and IMV, there is one decisive difference that marks the virion phase change. The IMV has two membrane-like layers when observed by both conventional thin sectioning and cryo-EM, where the inner one represents the newly formed core structure (*111*). The core is made by two substructures, the proteinaceous external core wall and an internal DNA-containing nucleocapsid. The core wall further contains two layers, where A10L and A4L are located on the outside and A3 located inside (*120*–*125*). The VACV core is not just structurally important for the virion but dynamically adopting the representing environment where early viral transcription occurs upon entry of VACV in the host cell (*120*). Thus, the VACV core, especially the core wall assembly

and disassembly mechanisms, is crucial for understanding orthopoxvirus packaging and is important for treatment development.

While the core wall morphology has been well studied, the molecular details of this substructure remain largely unknown due to the resolution limitation of both light microscopy as well as electron microscopy. In the 1990s, different groups identified that the outer layer of the Vaccinia core wall formed by continuous spike-like protrusions using TEM (*111*, *123*). Though studies have shown that these protrusions colocalize with A4L and A10L, the structure detail of these spikes has never been revealed. Here, leveraging recent advances in Cryo-ET and subtomogram average, we describe this outer core wall layer in molecular detail and obtain an electron density map of a single spike unit at ~10Å resolution.

5.2 Architecture and organization of Vaccinia MV

To reveal the molecular detail of VACV MV, we performed Cryo-ET to capture the high resolution information in 3D. The MVs have been amplified in mammalian cell line and quality controlled by negative stain EM (Figure 5.1 A). The resulting images revealed the presence of a majority of MVs and a small fraction of EVs. To image this sample by Cyo-ET we used the previously described dose-symmetric tilt method (*26*). The example reconstructed tomograms have been binned into 10Å per pixel followed by deconvolution denoise in order to boost the signal (Figure 5.1 B-F). All observed MVs form a roughly uniformly-sized soap bar-shaped structure with roughly 340 nm in X-axis, 260 nm in Y-axis and 120 nm in Z-axis, which correlates with previous studies.

The high resolution and high signal tomograms allow us to observe an undescribed virion organization. The fusion proteins and related proteins form a dense layer decorating the periphery of the lipid bilayer envelope . From the outside toward the center of the virus, we visualized newly observed thin protein layer, continuous spike layer, inner core wall layer, newly observed thread layer and DNA material in the coronal plane (Figure 5.1 B-C, G). In the median or transverse plane, we have two lateral bodies in between the spike layer and the envelope (Figure 5.1 D-E). Due to this special arrangement, the core wall forms a broad bean like structure, where its “belly” has been pushed inward by the two lateral bodies and detached from the envelope while the spike layer attaches to the membrane through the thin layer around the equator plan (Figure 5.1 G).

5.3 Structure determination of Vaccinia outer core wall layer

Though no symmetry can be applied to any part of the VACV, the spike layer is the only component that has a continuous regular pattern. Thus obtaining higher resolution information on the single repeat unit of the spike layer is feasible through subtomogram averaging. Subtomogram extraction coordinates are determined by subdivision of the manually defined surfaces which are traced on the spike layer, and particles have been extracted from original unprocessed tomograms (Figure 5.2 A). 3D classification has revealed multiple local arrangements of the spike layer due to the local flatness and curvature, which correlates with Cryo-ET observation of the core wall architecture (Figure 5.1 H and 5.2 B). Detailed inner core wall can be observed by C1 reconstruction with unidirectional curvature and shows a repeated square packing

pattern with double sublayers, whose repeat pattern differs from the spike layer (Figure 5.2 C-D). C3 reconstruction gives the best density for the spike layer with no change in the spike structure, which indicates the spike repeat unit likely has C3 symmetry (Figure 5.2 E-F). Details of the thin layer have been partially averaged out but still can be observed in low threshold (Figure 5.2 G). When focused on the center spike unit, the resulting density forms a crown-shaped structure on the bottom and protrusions on the top (Figure 5.2 H). A clear gap can be observed between the spike layer and the inner core wall, which indicates that the spike anchor onto the inner core wall is likely through flexible linkers (Figure 5.2).

Previous studies, putatively assigned the spike identity to either A4L, A10L or A3. The structure prediction has been conducted on each of the candidates as well as their posttranslational modification forms (Figure 5.3). Alphafold2 predictions on A10L and A3 resulted in high confidence structures, whereas the prediction on A4L was highly uncertain possibly due to the high proline content (Figure 5.3). Docking a trimeric AF2 model of A10L 1-614 yielded a reasonable, but imperfect, fitting with the subtomogram spike density and future work will allow to confirm or disprove this assignment (Figure 5.2 I and 5.3 F).

5.4 Discussion

Since the discovery of Vaccinia virus, the curiosity towards its architecture and organization never vanished. Due to the previous technical limitation in both light microscopy as well as the electron microscopy, our understanding about VACV is always limited by the resolution of observation. That is, though the general morphology

of different VACV virions has been described, the molecular detail of any component has never been revealed. Here, benefitting from the recent advance in Cryo-ET together with the subtomogram averaging approach, we described the general architecture of VACV MV and its layer organization with unprecedented details. Recent development in the subtomogram averaging approach, especially in particle extraction coordinates annotation and subtomo 3D classification, gives us the chance to achieve molecular detail of the MV spike layer. Although the term “spike”, also named as “palisade”, has been used for decades, this is the first time we observed and confirmed that this layer is composed of trimeric spikes (*126*). The resulting electron density also provides novel details towards the inner core wall and confirms the existence of the thin layer, while the thread layer has not been visualized due to the size of extracted subtomograms. Medium resolution density map can be acquired when only focusing on the center spike trimeric unit. The resulting map clearly shows the boundary of each monomer within the trimer, which provides preliminary evidence that trimeric A10L 1-614 might be the unit element of the spike layer. Together, with further biochemical and biophysical validation, we hope our study can provide a detailed description of the VACV MV focusing on its core wall, especially with the spike layer. With further functional studies, this work will further our understanding of the ultrastructural organization of orthopoxviruses along with their assembly/disassembly pathways.

5.5 Figures & Tables

Figure 5.1 Architecture and organization of Vaccinia MV revealed by Cryo-ET

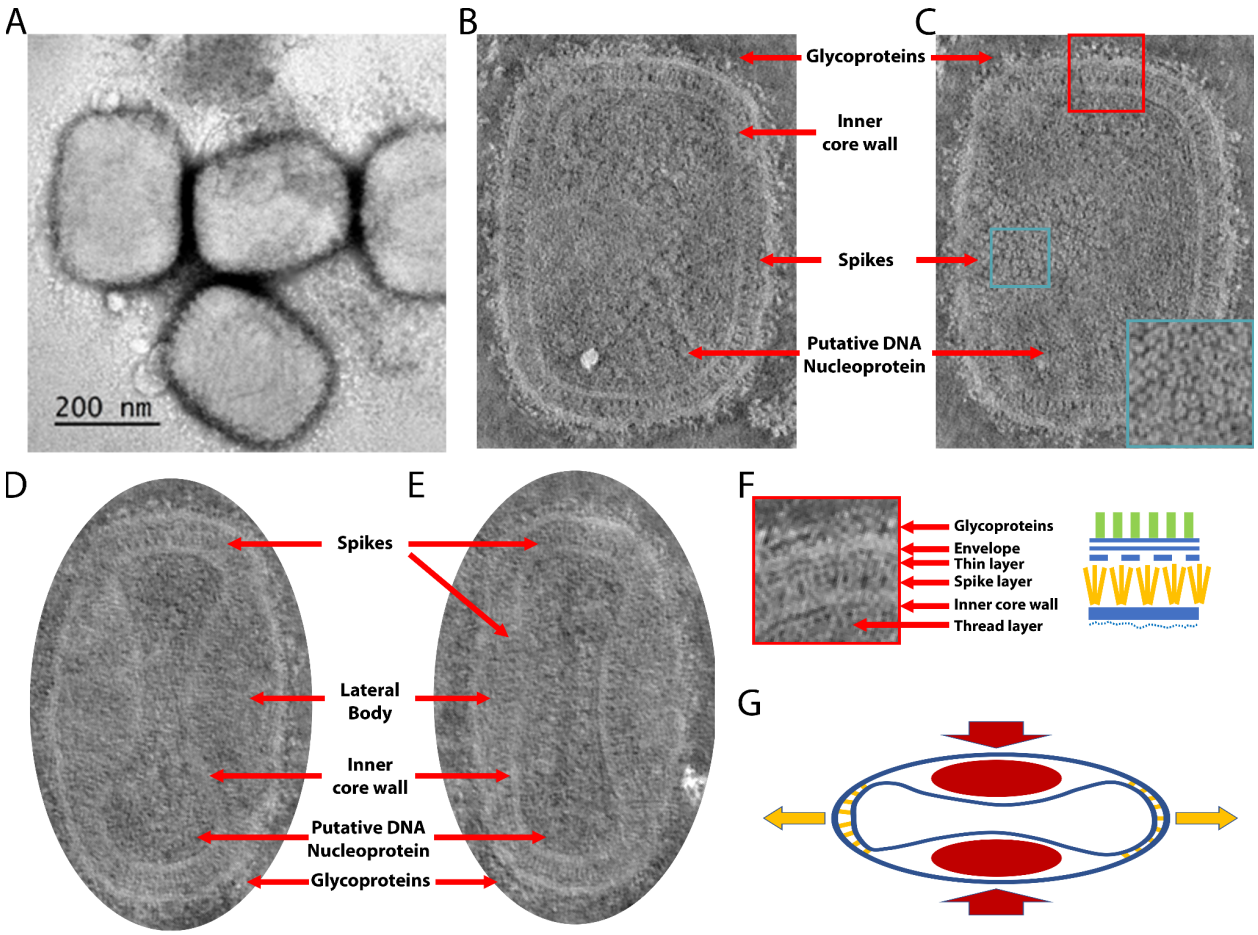

(**A**) Negative stain image of Vaccinia MV. (**B-C**) Cross section of single MV in coronal plane, where **B** is at the center of the Z axis and **C** is at the middle of the bottom half. Corresponding components have been labeled. Blue square refers to the bottom right zoom in view of the near horizontal spike layer. Red square refers to panel **F**, the zoom in view of the MV boundary. (**D-E**) Cross section of single MV in transverse plane, where **D** is at the center of the Z axis and **E** is at the middle of the bottom half. Corresponding components have been labeled. Lateral bodies cannot be directly viewed, the labeled regions refer to the annotated region in previous studies. (**F**) Zoom in view of the MV boundary. Corresponding components have been labeled. Cartoon on the right is a simplified representation. (**G**) Cartoon representation of core wall shape formation, where inner blue line refers to core wall, red solid ellipses refer to lateral

bodies, yellow lines refer to connection between core wall and envelope, outer empty ellipse refers to viral envelope. Arrows refer to the core wall curvature direction, whose color matches the source of the force.

Figure 5.2 Molecular detail of Vaccinia MV core wall determined by subtomogram average

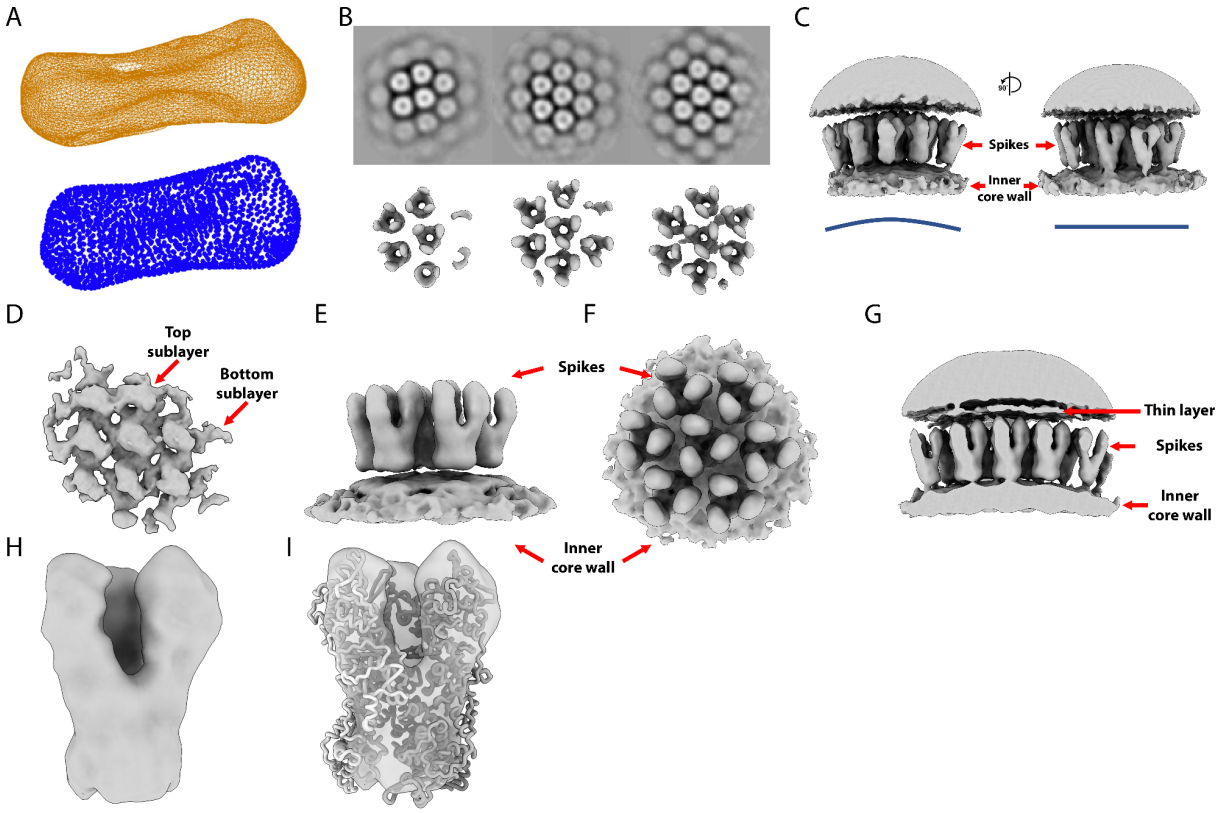

(**A**) Representative mesh (orange) and calculated points (blue) of spike layer extraction coordinates. (**B**) 3D classification shows possible variations of spike layer curvature. (**C**) C1 (asymmetric) refinement of most right class in panel **B** at low threshold, where the right figure is the left one rotated 90 degree along Z-axis. Spike layer and inner core wall layer have been labeled. Bottom blue lines indicate the curvature of the corresponding core wall. (**D**) Inner core wall layer of C1 refinement. Two sublayers can be observed, where the top layer formed by square repeats and bottom layer formed by tube-like densities. (**E-F**) C3 symmetry refinement of panel **C**, where the top density has been removed and only center trimers have been shown. (**G**) Middle cross section of C3 symmetry refinement at low threshold. Corresponding components have been labeled. Thin layer can be observed between the top-most density and the spike layer. (**H**) Electron density for center spike unit. (**I**) Center spike unit density fitted with Alphafold2 predicted A10 1-614 trimer (Figure 5.3 F), where each monomer has been colored in different gray gradients respectively.

Figure 5.3 Structure prediction of key core wall proteins

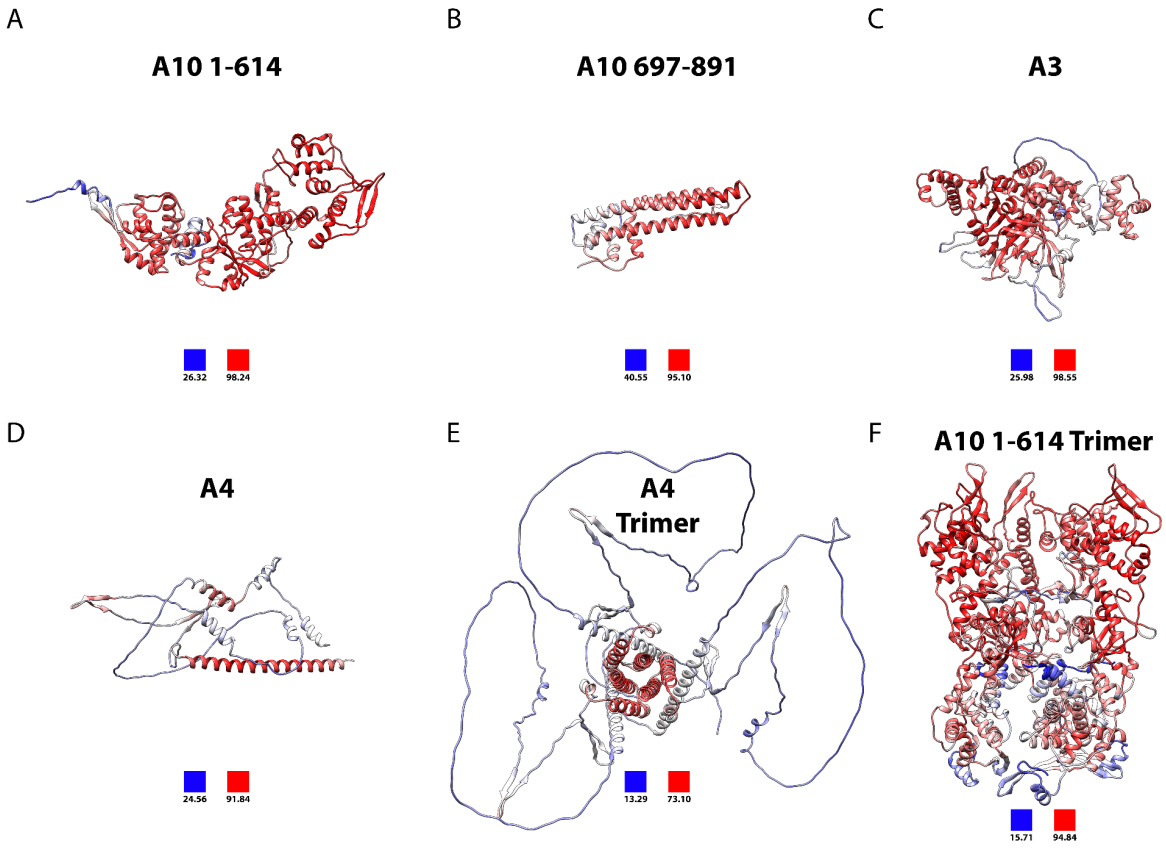

(**A-F**) Alphafold2 predictions of (**A**) A10 residue 1-614, (**B**) A10 residue 697-891, (**C**) A3, (**D**) A4, (**E**) trimeric A4 and (**F**) trimeric A10 residue 1-614. The color represents the prediction confidence calculated by Alphafold2, pLDDT (range from 0 to 100), where blue is the lower boundary and red is the upper boundary.

Chapter 6. Nucleoprotein ultrastructure of the Cedar virus

This chapter highlights how Cryo-ET and subtomogram averages can capture medium resolution electron volume maps of less rigid protein complexes. To prove this idea, here I acquire a medium low resolution (~15-20Å) electron volume map of Cedar virus nucleoprotein. Differ from Vaccinia virus, though Cedar virus is also enveloped virus, it does not have any organized protein layer, where its nucleoprotein protein only forms a very flexible helical filament.

On the biological side, this is the first observation of the henipavirus nucleoprotein filament in situ. Though the single turn nucleoprotein complex has already been described by single particle Cryo-EM in vitro, the in situ structure has the potential to produce a more precise definition on turn and rise as well as the contact site. Such information will be helpful for anti-nucleoprotein antiviral drug design.

6.1 Background

As the two major members of Henipavirus, Nipah virus (NiV) and Hendra virus (HeV) are highly pathogenic bat-borne paramyxoviruses that are classified as biosafety level-4 (BSL-4) select agents. Thus a significant challenge in studying Henipavirus is the requirement for BSL-4 containment suites. Due to this limitation, limited in situ information about Henipavirus morphology has been reported (*127*). Cedar virus, on the other hand, is nonpathogenic to humans, has been isolated from P. alecto and P. poliocephalus in Australia, which provides a powerful tool for studying Henipavirus in a

BSL-2 setup (*103*, *105*, *128*). Here we described Cedar virus ultrastructure and morphology in situ using Cryo-ET, and further demonstrated its nucleocapsid ultrastructure and organization by subtomogram average with very preliminary data. By acquiring larger datasets together with deepening on data analysis, we hope the information gathered from this in situ study could provide hints for future antiviral drug design and vaccine development.

6.2 In situ ultrastructure and morphology of Cedar virus

Wild type Cedar virus has been amplified in mammalian cell line and purified by sucrose gradient. Resulting live virus has been prepared for Cryo-ET imaging using the same strategy described in Chapter 5. As described in other Paramyxoviruses, the size of Cedar virus also varies a lot, where its diameter ranges from a little more than 100 nm to 300 nm and more, i.e. this is a pleomorphic virus (Figure 6.1 A-C). No well defined viral shape has been observed for Cedar virus, where the general organization is simply dense RNA material enclosed by a lipid membrane (Figure 6.1 A-C). Though most virions are either ball-shaped or like a leaked balloon, some of which have a very interesting empty cavity attached to the main viral body (Figure 6.1 B). The function and identity of these cavities are still unclear, as this is the first time it has been observed, but the electron density inside is denser than the outside buffer and seems some of which has membrane proteins loosely distributed, but they may represent artifacts of preparation (Figure 6.1 B). Cryo-ET reveals further details on the Cedar virus organization: the F and G glycoproteins sit outside the envelope with highly packed nucleoprotein filament enclosed inside (Figure 6.1 C-F). The nucleoprotein has clear

density and forms helical repeats (Figure 6.1 E). As observed in respiratory syncytial virus (RSV) studies, no matrix protein has been found in these mature Cedar viruses (*129*).

6.3 Structure and organization of Cedar virus nucleoprotein

Due to the flexibility and low contrast of the glycoproteins together with the local heterogeneity, subtomogram averaging is very challenging on these two targets. On the other hand, the nucleoprotein filament is a more tractable candidate. Due to the high flexibility and complicated twist of these filaments, geometric tracing in 3D is not practical, thus manual picking along the nucleoprotein raise has been performed to generate preliminary data (Figure 6.2 A). The resulting subtomograms can be averaged into 2-turn repeats or 4-turn repeats depending on the the box size but no longer filament can be reconstructed, which may relate to the flexibility of the filament (Figure 6.2 B-C). A single turn Nipah virus nucleoprotein complex has been described by single particle Cryo-EM in vitro (*130*). The reconstructed density maps are able to fit with the corresponding number of single turn nucleoprotein complexes (Figure 6.2 D-G). However, the clam-shaped assembly suggested by the in vitro study cannot be observed and further investigations are needed to reconcile these data (*130*).

6.4 Discussion

From the emergence of the deadly henipaviruses, a model system that can be used for studying this primarily BSL-4 restricted viral family has been needed. The discovery of Cedar virus fulfilled this imperative need. However, after 10 years of its first

detection, there is still no systematic description of the viral morphology. Thus, drawing support from the recent advance in Cryo-ET together with the subtomogram averaging approach, we are beginning to describe the morphology and general architecture of mature Cedar virus. With only a couple thousands nucleoprotein repeats through manual picking, we are able to reconstruct subtomogram averaging densities of the nucleoprotein filament complex up to 4 turns, where the resulting maps can be validated by in vitro structure fitting. With larger dataset, refined particle extraction coordinates and more elaborated data processing, a higher resolution and more detailed electron density map can be guaranteed. We hope this in situ study can prove the concept that any repeated protein complex is able to be reconstructed by subtomogram averaging with present processing pipeline and processing capacity. With further validation, we hope our observations can provide useful information for henipavirus vaccine development as well as anti-nucleoprotein antiviral drug design.

6.5 Figures & Tables

Figure 6.1 Architecture and organization of Cedar virus revealed by Cryo-ET

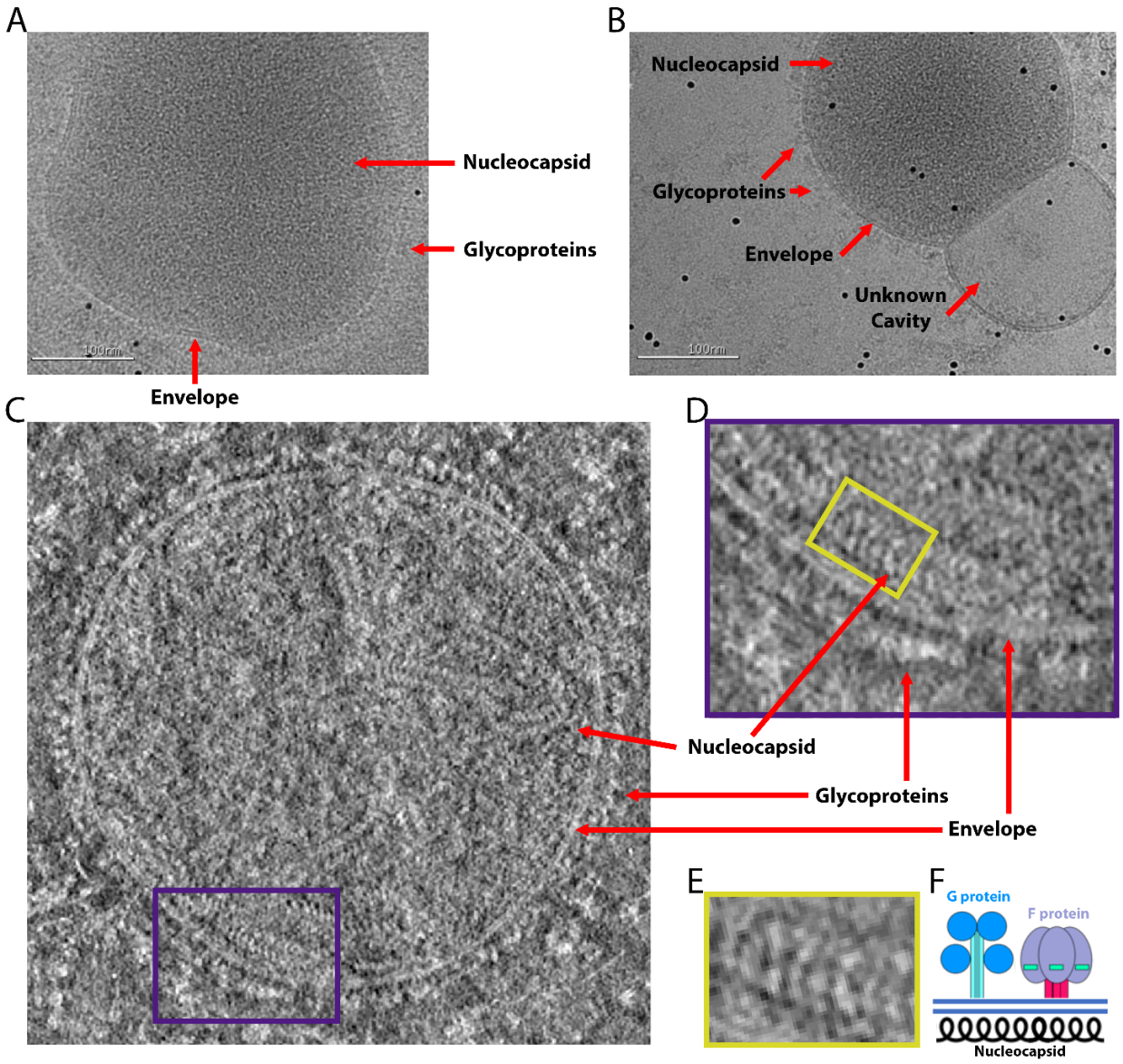

(**A-B**) Cryo-EM images for different wild type Cedar virus particles. Corresponding components have been labeled. (**C**) Cross section of single Cedar virus in the coronal plane at the center of the Z axis. Corresponding components have been labeled. Purple rectangular refers to panel **D**, the zoom in view of viral boundary. (**D**) Zoom in view of the viral boundary. Corresponding components have been labeled. Yellow rectangular refers to panel **E**, the zoom in view of nucleoprotein. (**E**) Zoom in

view of nucleoprotein repeats. (**F**) Cartoon of simplified representation Cedar virus organization. Corresponding components have been labeled and the double blue line refers to the envelope.

Figure 6.2 Molecular detail of Cedar virus nucleoprotein determined by subtomogram average

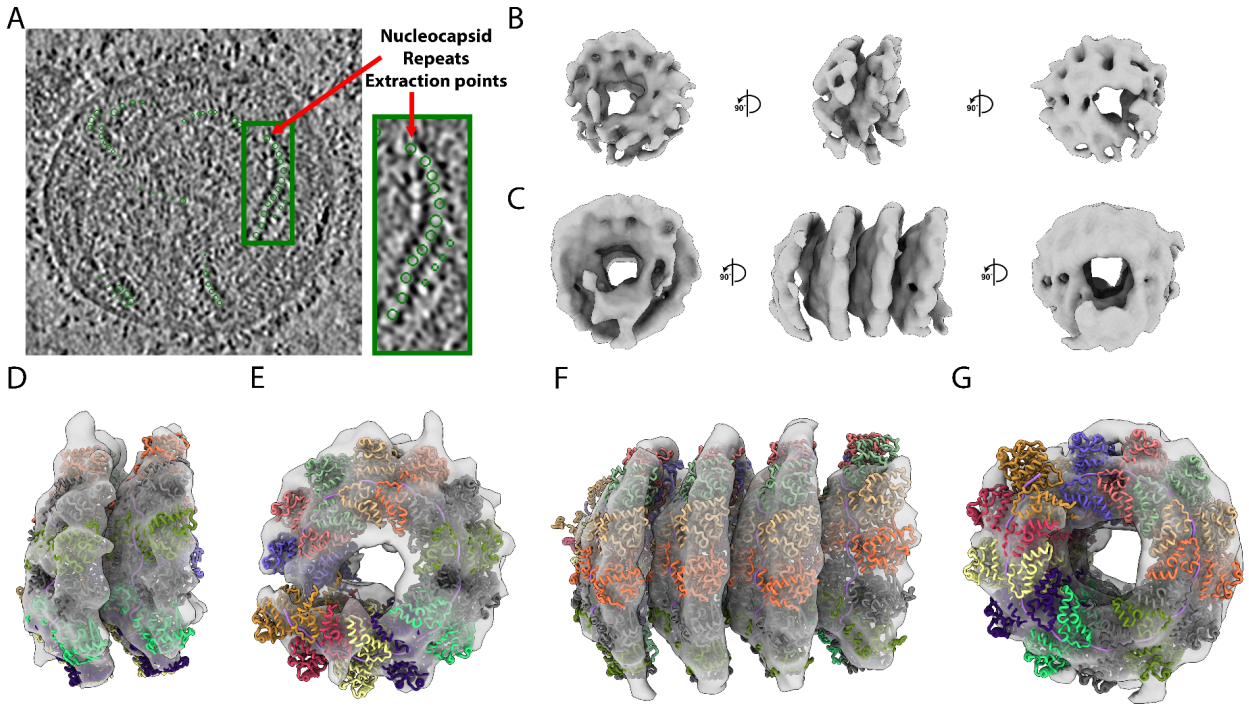

(**A**) Representative tomogram slide for particle extraction coordinates annotation. (**B-C**) Reconstructed electron density maps of 2-turn (at high threshold) and 4-turn (at low threshold) nucleoprotein repeats in back, side and front view respectively. (**D-F**) 2-turn reconstruction fitted with PDB 7NT5 in side, **D**, and front view, **E**. (**F-G**) 4-turn reconstruction fitted with PDB 7NT5 in side, **F**, and front view, **G**.

Chapter 7. Conclusion and future directions

Back in 2016, the first spike protein structure of a coronavirus was determined in the Veesler lab by Lexi Walls at 4Å using single particle Cryo-EM (*40*). In order to achieve the near-atomic resolution electron density map used for building such molecular model, the whole lab has put 1 year of incredible efforts. Only 3 years later in early 2019, still using single particle Cryo-EM, we solved the MERS-CoV spike protein at 2.7Å within less than 3 months, as described in ***chapter 2***. We were not only able to achieve well resolved electron density for the protein itself but also for the small molecules as well as organized water networks. Another 3 years passed, at this moment, 3 weeks is long enough to obtain a 2.5Å spike protein structure. And with reasonable efforts, we can even push the resolution to 2.2Å, which has already reached the nyquist limitation for that particular dataset (*131*). These successes are not only contributed by the “resolution revolution” in the Cryo-EM field, but more importantly is due to the current ongoing “efficiency revolution”, both in data collection speed as well as in data processing capacity. As a result, during the current pandemic we can keep up our antigenic knowledge of the spike protein when new variants emerge incessantly.

While the spike protein obeys C3 symmetry most of the time and has a MW of over 400 kDa, we demonstrated that cryoEM also has the ability to solve much smaller, heterogeneous and non-symmetric protein complexes at near-atomic resolution, as described in ***chapter 3***. We also illustrated that the current single particle data analysis pipeline can sort out not just heterogeneous proteins but also heterogeneous datasets where multiple macromolecular species present at the same time. Such competence is

critical for solving systematic problems, such as antigenicity potency distribution of certain antigen.

With all these advances in EM, the resolution, the variety and the number of protein structures being solved all ameliorated enormously. But achieving beautiful structures is never the end of structure biology, it is only the end of the beginning. In ***chapter 4***, we described how the structure information we acquired in ***chapter 3*** can be used for building up new strategies for antiviral antibody cocktail development. The architecture and antigenicity of Nipah virus G protein expedited the identification of orthogonal mAb pairs for possible future cocktail development.

As we can see how powerful and useful single particle Cryo-EM can be, Cryo-ET and subtomogram averaging, the single particle approach in Cryo-ET, have also progressed dramatically. Only a few years ago, Cryo-ET was only used for microscale observation but not at molecular level. However, recently multiple groups have shown that Cryo-ET can give us reasonable high resolution information, where subtomogram reconstruction can achieve near-atomic resolution. ***Chapter 5*** and ***6*** are examples of how Cryo-ET and subtomogram averaging yield structural information within an in situ environment. The most important fact about these two stories is that the time spent on each of the projects to achieve the results at the current stage only took around two months, instead of years as most previously published Cryo-ET work could sometimes take.

Nonetheless, as we can see from these two Cryo-ET studies, to fully achieve an atomic or near-atomic structure by subtomogram averaging still needs a lot of effort. But the limitations on high resolution Cryo-ET structures are nothing different from the

limitations for single particle Cryo-EM 6 years ago, which are just particle picking and computational power. Looking at the path of single particle approach development, it will not be a big surprise that within countable years that solving high resolution Cryo-ET structures will transform from “insurmountable” to “routine”.

In all, I hope this dissertation draws an outline of how structure biology can be adopted for application approaches, and how it can change our perspective in various ways.

Reference

1. T. G. Ksiazek, D. Erdman, C. S. Goldsmith, S. R. Zaki, T. Peret, S. Emery, S. Tong, C. Urbani, J. A. Comer, W. Lim, P. E. Rollin, S. F. Dowell, A.-E. Ling, C. D. Humphrey, W.-J. Shieh, J. Guarner, C. D. Paddock, P. Rota, B. Fields, J. DeRisi, J.-Y. Yang, N. Cox, J. M. Hughes, J. W. LeDuc, W. J. Bellini, L. J. Anderson, SARS Working Group, A novel coronavirus associated with severe acute respiratory syndrome. *N. Engl. J. Med.* **348**, 1953–1966 (2003).

2. C. Drosten, S. Günther, W. Preiser, S. van der Werf, H.-R. Brodt, S. Becker, H. Rabenau, M. Panning, L. Kolesnikova, R. A. M. Fouchier, A. Berger, A.-M. Burguière, J. Cinatl, M. Eickmann, N. Escriou, K. Grywna, S. Kramme, J.-C. Manuguerra, S. Müller, V. Rickerts, M. Stürmer, S. Vieth, H.-D. Klenk, A. D. M. E. Osterhaus, H. Schmitz, H. W. Doerr, Identification of a novel coronavirus in patients with severe acute respiratory syndrome. *N. Engl. J. Med.* **348**, 1967–1976 (2003).

3. A. M. Zaki, S. van Boheemen, T. M. Bestebroer, A. D. M. E. Osterhaus, R. A. M. Fouchier, Isolation of a novel coronavirus from a man with pneumonia in Saudi Arabia. *N. Engl. J. Med.* **367**, 1814–1820 (2012).

4. M. A. Tortorici, D. Veesler, Structural insights into coronavirus entry. *Adv. Virus Res.* **105**, 93–116 (2019).

5. A. C. Walls, Y.-J. Park, M. A. Tortorici, A. Wall, A. T. McGuire, D. Veesler, Structure, Function, and Antigenicity of the SARS-CoV-2 Spike Glycoprotein. *Cell*. **183**, 1735 (2020).

6. W. Song, M. Gui, X. Wang, Y. Xiang, Cryo-EM structure of the SARS coronavirus spike glycoprotein in complex with its host cell receptor ACE2. *PLoS Pathog.* **14**, e1007236 (2018).

7. N. Wang, X. Shi, L. Jiang, S. Zhang, D. Wang, P. Tong, D. Guo, L. Fu, Y. Cui, X. Liu, K. C. Arledge, Y.-H. Chen, L. Zhang, X. Wang, Structure of MERS-CoV spike receptor-binding domain complexed with human receptor DPP4. *Cell Res.* **23**, 986–993 (2013).

8. Z. Wang, M. Amaya, A. Addetia, H. V. Dang, G. Reggiano, L. Yan, A. C. Hickey, F. DiMaio, C. C. Broder, D. Veesler, Architecture and antigenicity of the Nipah virus attachment glycoprotein. *Science*, eabm5561 (2022).

9. Z. Wang, H. V. Dang, M. Amaya, Y. Xu, R. Yin, L. Yan, A. C. Hickey, E. J. Annand, B. A. Horsburgh, P. A. Reid, I. Smith, J.-S. Eden, K. Xu, C. C. Broder, D. Veesler, Potent monoclonal antibody–mediated neutralization of a divergent Hendra virus variant. *Proceedings of the National Academy of Sciences*. **119**, e2122769119 (2022).

10. E. G. Playford, T. Munro, S. M. Mahler, S. Elliott, M. Gerometta, K. L. Hoger, M. L. Jones, P. Griffin, K. D. Lynch, H. Carroll, Others, Safety, tolerability, pharmacokinetics, and immunogenicity of a human monoclonal antibody targeting the G glycoprotein of henipaviruses in healthy adults: a first-in-human, randomised, controlled, phase 1 study. *Lancet Infect. Dis.* **20**, 445–454 (2020).

11. K. N. Bossart, B. Rockx, F. Feldmann, D. Brining, D. Scott, R. LaCasse, J. B. Geisbert, Y.-R. Feng, Y.-P. Chan, A. C. Hickey, C. C. Broder, H. Feldmann, T. W. Geisbert, A Hendra virus G glycoprotein subunit vaccine protects African green monkeys from Nipah virus challenge. *Sci. Transl. Med.* **4**, 146ra107 (2012).

12. K. N. Bossart, G. Crameri, A. S. Dimitrov, B. A. Mungall, Y.-R. Feng, J. R. Patch, A. Choudhary, L.-F. Wang, B. T. Eaton, C. C. Broder, Receptor binding, fusion inhibition, and induction of cross-reactive neutralizing antibodies by a soluble G glycoprotein of Hendra virus. *J. Virol.* **79**, 6690–6702 (2005).

13. B. A. Mungall, D. Middleton, G. Crameri, J. Bingham, K. Halpin, G. Russell, D. Green, J. McEachern, L. Ian Pritchard, B. T. Eaton, L.-F. Wang, K. N. Bossart, C. C. Broder, Feline Model of Acute Nipah Virus Infection and Protection with a Soluble Glycoprotein-Based Subunit Vaccine. *Journal of Virology*. **80** (2006), pp. 12293–12302.

14. J. A. McEachern, J. Bingham, G. Crameri, D. J. Green, T. J. Hancock, D. Middleton, Y.-R. Feng, C. C. Broder, L.-F. Wang, K. N. Bossart, A recombinant subunit vaccine formulation protects against lethal Nipah virus challenge in cats. *Vaccine*. **26**, 3842–3852 (2008).

15. J. Pallister, D. Middleton, L.-F. Wang, R. Klein, J. Haining, R. Robinson, M. Yamada, J. White, J. Payne, Y.-R. Feng, Y.-P. Chan, C. C. Broder, A recombinant Hendra virus G glycoprotein-based subunit vaccine protects ferrets from lethal Hendra virus challenge. *Vaccine*. **29**, 5623–5630 (2011).

16. C. E. Mire, J. B. Geisbert, K. N. Agans, Y.-R. Feng, K. A. Fenton, K. N. Bossart, L. Yan, Y.-P. Chan, C. C. Broder, T. W. Geisbert, A recombinant Hendra virus G glycoprotein subunit vaccine protects nonhuman primates against Hendra virus challenge. *J. Virol.* **88**, 4624–4631 (2014).

17. D. Middleton, J. Pallister, R. Klein, Y.-R. Feng, J. Haining, R. Arkinstall, L. Frazer, J.-A. Huang, N. Edwards, M. Wareing, M. Elhay, Z. Hashmi, J. Bingham, M. Yamada, D. Johnson, J. White, A. Foord, H. G. Heine, G. A. Marsh, C. C. Broder, L.-F. Wang, Hendra virus vaccine, a one health approach to protecting horse, human, and environmental health. *Emerg. Infect. Dis.* **20**, 372–379 (2014).

18. G. P. Johnson, S. J. Goebel, E. Paoletti, An update on the vaccinia virus genome. *Virology*. **196**, 381–401 (1993).

19. R. Heljasvaara, D. Rodríguez, C. Risco, J. L. Carrascosa, M. Esteban, J. R. Rodríguez, The major core protein P4a (A10L gene) of vaccinia virus is essential for correct assembly of viral DNA into the nucleoprotein complex to form immature viral particles. *J. Virol.* **75**, 5778–5795 (2001).

20. P. Le Mercier Chantal Hulo Patrick Masson (content), Edouard de Castro (software), Orthopoxvirus replication ~ ViralZone, (available at https://viralzone.expasy.org/4399).

21. A. Grifoni, Y. Zhang, A. Tarke, J. Sidney, P. Rubiro, M. Reina-Campos, G. Filaci, J. M. Dan, R. H. Scheuermann, A. Sette, Defining antigen targets to dissect vaccinia virus and mpox virus-specific T cell responses in humans. *Cell Host Microbe* (2022), doi:10.1016/j.chom.2022.11.003.

22. R. Henderson, P. N. Unwin, Three-dimensional model of purple membrane obtained by

electron microscopy. *Nature*. **257**, 28–32 (1975).

23. P. Brüggeller, E. Mayer, Complete vitrification in pure liquid water and dilute aqueous solutions. *Nature*. **288**, 569–571 (1980).

24. K. P. Ryan, D. H. Purse, S. G. Robinson, J. W. Wood, The relative efficiency of cryogens used for plunge-cooling biological specimens. *J. Microsc.* **145**, 89–96 (1987).

25. D. Tegunov, L. Xue, C. Dienemann, P. Cramer, J. Mahamid, Multi-particle cryo-EM refinement with M visualizes ribosome-antibiotic complex at 3.5 Å in cells. *Nat. Methods*. **18**, 186–193 (2021).

26. F. K. M. Schur, M. Obr, W. J. H. Hagen, W. Wan, A. J. Jakobi, J. M. Kirkpatrick, C. Sachse, H.-G. Kräusslich, J. A. G. Briggs, An atomic model of HIV-1 capsid-SP1 reveals structures regulating assembly and maturation. *Science*. **353**, 506–508 (2016).

27. Cryo EM 101 – Cryo EM 101, (available at https://cryoem101.org/).

28. D.-N. Le, H. T. Nguyen-Truong, Analytical Formula for the Electron Inelastic Mean Free Path. *J. Phys. Chem. C*. **125**, 18946–18951 (2021).

29. D. R. Penn, Electron mean-free-path calculations using a model dielectric function. *Phys. Rev. B Condens. Matter*. **35**, 482–486 (1987).

30. B. L. Haagmans, S. H. S. Al Dhahiry, C. B. E. M. Reusken, V. S. Raj, M. Galiano, R. Myers, G.-J. Godeke, M. Jonges, E. Farag, A. Diab, H. Ghobashy, F. Alhajri, M. Al-Thani, S. A. Al-Marri, H. E. Al Romaihi, A. Al Khal, A. Bermingham, A. D. M. E. Osterhaus, M. M. AlHajri, M. P. G. Koopmans, Middle East respiratory syndrome coronavirus in dromedary camels: an outbreak investigation. *Lancet Infect. Dis.* **14**, 140–145 (2014).

31. J. S. M. Sabir, T. T.-Y. Lam, M. M. M. Ahmed, L. Li, Y. Shen, S. E. M. Abo-Aba, M. I. Qureshi, M. Abu-Zeid, Y. Zhang, M. A. Khiyami, N. S. Alharbi, N. H. Hajrah, M. J. Sabir, M. H. Z. Mutwakil, S. A. Kabli, F. A. S. Alsulaimany, A. Y. Obaid, B. Zhou, D. K. Smith, E. C. Holmes, H. Zhu, Y. Guan, Co-circulation of three camel coronavirus species and recombination of MERS-CoVs in Saudi Arabia. *Science*. **351**, 81–84 (2016).

32. P. C. Y. Woo, S. K. P. Lau, K. S. M. Li, R. W. S. Poon, B. H. L. Wong, H.-W. Tsoi, B. C. K. Yip, Y. Huang, K.-H. Chan, K.-Y. Yuen, Molecular diversity of coronaviruses in bats. *Virology*. **351**, 180–187 (2006).

33. V. D. Menachery, B. L. Yount Jr, K. Debbink, S. Agnihothram, L. E. Gralinski, J. A. Plante, R. L. Graham, T. Scobey, X.-Y. Ge, E. F. Donaldson, S. H. Randell, A. Lanzavecchia, W. A. Marasco, Z.-L. Shi, R. S. Baric, Corrigendum: A SARS-like cluster of circulating bat coronaviruses shows potential for human emergence. *Nat. Med.* **22**, 446 (2016).

34. V. D. Menachery, B. L. Yount Jr, A. C. Sims, K. Debbink, S. S. Agnihothram, L. E. Gralinski, R. L. Graham, T. Scobey, J. A. Plante, S. R. Royal, J. Swanstrom, T. P. Sheahan, R. J. Pickles, D. Corti, S. H. Randell, A. Lanzavecchia, W. A. Marasco, R. S. Baric, SARS-like WIV1-CoV poised for human emergence. *Proc. Natl. Acad. Sci. U. S. A.* **113**, 3048–3053 (2016).

35. B. Hu, L.-P. Zeng, X.-L. Yang, X.-Y. Ge, W. Zhang, B. Li, J.-Z. Xie, X.-R. Shen, Y.-Z. Zhang,

N. Wang, D.-S. Luo, X.-S. Zheng, M.-N. Wang, P. Daszak, L.-F. Wang, J. Cui, Z.-L. Shi, Discovery of a rich gene pool of bat SARS-related coronaviruses provides new insights into the origin of SARS coronavirus. *PLoS Pathog.* **13**, e1006698 (2017).

36. M. Gui, W. Song, H. Zhou, J. Xu, S. Chen, Y. Xiang, X. Wang, Cryo-electron microscopy structures of the SARS-CoV spike glycoprotein reveal a prerequisite conformational state for receptor binding. *Cell Res.* **27**, 119–129 (2017).

37. R. N. Kirchdoerfer, C. A. Cottrell, N. Wang, J. Pallesen, H. M. Yassine, H. L. Turner, K. S. Corbett, B. S. Graham, J. S. McLellan, A. B. Ward, Pre-fusion structure of a human coronavirus spike protein. *Nature*. **531**, 118–121 (2016).

38. J. Shang, Y. Zheng, Y. Yang, C. Liu, Q. Geng, C. Luo, W. Zhang, F. Li, Cryo-EM structure of infectious bronchitis coronavirus spike protein reveals structural and functional evolution of coronavirus spike proteins. *PLoS Pathog.* **14**, e1007009 (2018).

39. J. Shang, Y. Zheng, Y. Yang, C. Liu, Q. Geng, W. Tai, L. Du, Y. Zhou, W. Zhang, F. Li, Cryo-Electron Microscopy Structure of Porcine Deltacoronavirus Spike Protein in the Prefusion State. *J. Virol.* **92** (2018), doi:10.1128/JVI.01556-17.

40. A. C. Walls, M. A. Tortorici, B.-J. Bosch, B. Frenz, P. J. M. Rottier, F. DiMaio, F. A. Rey, D. Veesler, Cryo-electron microscopy structure of a coronavirus spike glycoprotein trimer. *Nature*. **531**, 114–117 (2016).

41. A. C. Walls, M. A. Tortorici, B. Frenz, J. Snijder, W. Li, F. A. Rey, F. DiMaio, B.-J. Bosch, D. Veesler, Glycan shield and epitope masking of a coronavirus spike protein observed by cryo-electron microscopy. *Nat. Struct. Mol. Biol.* **23**, 899–905 (2016).

42. X. Xiong, M. A. Tortorici, J. Snijder, C. Yoshioka, A. C. Walls, W. Li, A. T. McGuire, F. A. Rey, B.-J. Bosch, D. Veesler, Glycan Shield and Fusion Activation of a Deltacoronavirus Spike Glycoprotein Fine-Tuned for Enteric Infections. *J. Virol.* **92** (2018), doi:10.1128/JVI.01628-17.

43. Yuan, Y. Yuan, D. Cao, Y. Zhang, J. Ma, J. Qi, Q. Wang, G. Lu, Y. Wu, J. Yan, Y. Shi, X. Zhang, G. F. Gao, Cryo-EM structures of MERS-CoV and SARS-CoV spike glycoproteins reveal the dynamic receptor binding domains. *Nature Communications*. **8** (2017), , doi:10.1038/ncomms15092.

44. A. C. Walls, M. A. Tortorici, J. Snijder, X. Xiong, B.-J. Bosch, F. A. Rey, D. Veesler, Tectonic conformational changes of a coronavirus spike glycoprotein promote membrane fusion. *Proc. Natl. Acad. Sci. U. S. A.* **114**, 11157–11162 (2017).

45. R. N. Kirchdoerfer, N. Wang, J. Pallesen, D. Wrapp, H. L. Turner, C. A. Cottrell, K. S. Corbett, B. S. Graham, J. S. McLellan, A. B. Ward, Publisher Correction: Stabilized coronavirus spikes are resistant to conformational changes induced by receptor recognition or proteolysis. *Sci. Rep.* **8**, 17823 (2018).

46. M. A. Tortorici, A. C. Walls, Y. Lang, C. Wang, Z. Li, D. Koerhuis, G.-J. Boons, B.-J. Bosch, F. A. Rey, R. J. de Groot, D. Veesler, Structural basis for human coronavirus attachment to sialic acid receptors. *Nat. Struct. Mol. Biol.* **26**, 481–489 (2019).

47. A. C. Walls, X. Xiong, Y.-J. Park, M. Alejandra Tortorici, J. Snijder, J. Quispe, E. Cameroni,

R. Gopal, M. Dai, A. Lanzavecchia, M. Zambon, F. A. Rey, D. Corti, D. Veesler, Unexpected Receptor Functional Mimicry Elucidates Activation of Coronavirus Fusion. *Cell*. **183** (2020), p. 1732.

48. J. Pallesen, N. Wang, K. S. Corbett, D. Wrapp, R. N. Kirchdoerfer, H. L. Turner, C. A. Cottrell, M. M. Becker, L. Wang, W. Shi, W.-P. Kong, E. L. Andres, A. N. Kettenbach, M. R. Denison, J. D. Chappell, B. S. Graham, A. B. Ward, J. S. McLellan, Immunogenicity and structures of a rationally designed prefusion MERS-CoV spike antigen. *Proc. Natl. Acad. Sci. U. S. A.* **114**, E7348–E7357 (2017).

49. V. S. Raj, H. Mou, S. L. Smits, D. H. W. Dekkers, M. A. Müller, R. Dijkman, D. Muth, J. A. A. Demmers, A. Zaki, R. A. M. Fouchier, V. Thiel, C. Drosten, P. J. M. Rottier, A. D. M. E. Osterhaus, B. J. Bosch, B. L. Haagmans, Dipeptidyl peptidase 4 is a functional receptor for the emerging human coronavirus-EMC. *Nature*. **495**, 251–254 (2013).

50. J.-E. Park, K. Li, A. Barlan, A. R. Fehr, S. Perlman, P. B. McCray Jr, T. Gallagher, Proteolytic processing of Middle East respiratory syndrome coronavirus spikes expands virus tropism. *Proc. Natl. Acad. Sci. U. S. A.* **113**, 12262–12267 (2016).

51. J. K. Millet, G. R. Whittaker, Host cell entry of Middle East respiratory syndrome coronavirus after two-step, furin-mediated activation of the spike protein. *Proc. Natl. Acad. Sci. U. S. A.* **111**, 15214–15219 (2014).

52. J. T. Earnest, M. P. Hantak, K. Li, P. B. McCray Jr, S. Perlman, T. Gallagher, The tetraspanin CD9 facilitates MERS-coronavirus entry by scaffolding host cell receptors and proteases. *PLoS Pathog.* **13**, e1006546 (2017).

53. J. T. Earnest, M. P. Hantak, J.-E. Park, T. Gallagher, Coronavirus and influenza virus proteolytic priming takes place in tetraspanin-enriched membrane microdomains. *J. Virol.* **89**, 6093–6104 (2015).

54. Y. Yang, C. Liu, L. Du, S. Jiang, Z. Shi, R. S. Baric, F. Li, Two Mutations Were Critical for Bat-to-Human Transmission of Middle East Respiratory Syndrome Coronavirus. *J. Virol.* **89**, 9119–9123 (2015).

55. J. E. Stencel-Baerenwald, K. Reiss, D. M. Reiter, T. Stehle, T. S. Dermody, The sweet spot: defining virus–sialic acid interactions. *Nat. Rev. Microbiol.* **12**, 739–749 (2014).

56. X. Xiong, P. J. Coombs, S. R. Martin, J. Liu, H. Xiao, J. W. McCauley, K. Locher, P. A. Walker, P. J. Collins, Y. Kawaoka, J. J. Skehel, S. J. Gamblin, Receptor binding by a ferret-transmissible H5 avian influenza virus. *Nature*. **497**, 392–396 (2013).

57. X. Xiong, S. R. Martin, L. F. Haire, S. A. Wharton, R. S. Daniels, M. S. Bennett, J. W. McCauley, P. J. Collins, P. A. Walker, J. J. Skehel, S. J. Gamblin, Receptor binding by an H7N9 influenza virus from humans. *Nature*. **499**, 496–499 (2013).

58. J. Liu, D. J. Stevens, L. F. Haire, P. A. Walker, P. J. Coombs, R. J. Russell, S. J. Gamblin, J. J. Skehel, Structures of receptor complexes formed by hemagglutinins from the Asian Influenza pandemic of 1957. *Proc. Natl. Acad. Sci. U. S. A.* **106**, 17175–17180 (2009).

59. G. Lu, Y. Hu, Q. Wang, J. Qi, F. Gao, Y. Li, Y. Zhang, W. Zhang, Y. Yuan, J. Bao, B. Zhang, Y. Shi, J. Yan, G. F. Gao, Molecular basis of binding between novel human coronavirus

MERS-CoV and its receptor CD26. *Nature*. **500**, 227–231 (2013).

60. W. Li, R. J. G. Hulswit, I. Widjaja, V. S. Raj, R. McBride, W. Peng, W. Widagdo, M. A. Tortorici, B. van Dieren, Y. Lang, J. W. M. van Lent, J. C. Paulson, C. A. M. de Haan, R. J. de Groot, F. J. M. van Kuppeveld, B. L. Haagmans, B.-J. Bosch, Identification of sialic acid-binding function for the Middle East respiratory syndrome coronavirus spike glycoprotein. *Proc. Natl. Acad. Sci. U. S. A.* **114**, E8508–E8517 (2017).

61. W. Widagdo, V. S. Raj, D. Schipper, K. Kolijn, G. J. L. H. van Leenders, B. J. Bosch, A. Bensaid, J. Segalés, W. Baumgärtner, A. D. M. E. Osterhaus, M. P. Koopmans, J. M. A. van den Brand, B. L. Haagmans, Differential Expression of the Middle East Respiratory Syndrome Coronavirus Receptor in the Upper Respiratory Tracts of Humans and Dromedary Camels. *J. Virol.* **90**, 4838–4842 (2016).

62. J. Vergara-Alert, J. M. A. van den Brand, W. Widagdo, M. Muñoz 5th, S. Raj, D. Schipper, D. Solanes, I. Cordón, A. Bensaid, B. L. Haagmans, J. Segalés, Livestock Susceptibility to Infection with Middle East Respiratory Syndrome Coronavirus. *Emerg. Infect. Dis.* **23**, 232–240 (2017).

63. A. Barlan, J. Zhao, M. K. Sarkar, K. Li, P. B. McCray Jr, S. Perlman, T. Gallagher, Receptor variation and susceptibility to Middle East respiratory syndrome coronavirus infection. *J. Virol.* **88**, 4953–4961 (2014).

64. B. Meyer, I. García-Bocanegra, U. Wernery, R. Wernery, A. Sieberg, M. A. Müller, J. F. Drexler, C. Drosten, I. Eckerle, Serologic assessment of possibility for MERS-CoV infection in equids. *Emerg. Infect. Dis.* **21**, 181–182 (2015).

65. R. J. G. Hulswit, Y. Lang, M. J. G. Bakkers, W. Li, Z. Li, A. Schouten, B. Ophorst, F. J. M. van Kuppeveld, G.-J. Boons, B.-J. Bosch, E. G. Huizinga, R. J. de Groot, Human coronaviruses OC43 and HKU1 bind to 9-O-acetylated sialic acids via a conserved receptor-binding site in spike protein domain A. *Proc. Natl. Acad. Sci. U. S. A.* **116**, 2681–2690 (2019).

66. M. G. Campbell, D. Veesler, A. Cheng, C. S. Potter, B. Carragher, 2.8 Å resolution reconstruction of the Thermoplasma acidophilum 20S proteasome using cryo-electron microscopy. *Elife*. **4** (2015), doi:10.7554/eLife.06380.

67. J. K. Millet, G. R. Whittaker, Murine Leukemia Virus (MLV)-based Coronavirus Spike-pseudotyped Particle Production and Infection. *Bio Protoc*. **6** (2016), doi:10.21769/BioProtoc.2035.

68. I. N. A. Wickramasinghe, R. P. de Vries, A. Gröne, C. A. M. de Haan, M. H. Verheije, Binding of avian coronavirus spike proteins to host factors reflects virus tropism and pathogenicity. *J. Virol.* **85**, 8903–8912 (2011).

69. M. J. G. Bakkers, Y. Lang, L. J. Feitsma, R. J. G. Hulswit, S. A. H. de Poot, A. L. W. van Vliet, I. Margine, J. D. F. de Groot-Mijnes, F. J. M. van Kuppeveld, M. A. Langereis, E. G. Huizinga, R. J. de Groot, Betacoronavirus Adaptation to Humans Involved Progressive Loss of Hemagglutinin-Esterase Lectin Activity. *Cell Host Microbe*. **21**, 356–366 (2017).

70. C.-M. Chan, H. Chu, Y. Wang, B. H.-Y. Wong, X. Zhao, J. Zhou, D. Yang, S. P. Leung, J. F.-W. Chan, M.-L. Yeung, J. Yan, G. Lu, G. F. Gao, K.-Y. Yuen, Carcinoembryonic

Antigen-Related Cell Adhesion Molecule 5 Is an Important Surface Attachment Factor That Facilitates Entry of Middle East Respiratory Syndrome Coronavirus. *J. Virol.* **90**, 9114–9127 (2016).

71. H. Chu, C.-M. Chan, X. Zhang, Y. Wang, S. Yuan, J. Zhou, R. K.-H. Au-Yeung, K.-H. Sze, D. Yang, H. Shuai, Y. Hou, C. Li, X. Zhao, V. K.-M. Poon, S. P. Leung, M.-L. Yeung, J. Yan, G. Lu, D.-Y. Jin, G. F. Gao, J. F.-W. Chan, K.-Y. Yuen, Middle East respiratory syndrome coronavirus and bat coronavirus HKU9 both can utilize GRP78 for attachment onto host cells. *Journal of Biological Chemistry*. **293** (2018), pp. 11709–11726.

72. I. Widjaja, C. Wang, R. van Haperen, J. Gutiérrez-Álvarez, B. van Dieren, N. M. A. Okba, V. Stalin Raj, W. Li, R. Fernandez-Delgado, F. Grosveld, F. J. M. van Kuppeveld, B. L. Haagmans, L. Enjuanes, D. Drabek, B.-J. Bosch, Towards a solution to MERS: protective human monoclonal antibodies targeting different domains and functions of the MERS-coronavirus spike glycoprotein. *Emerging Microbes & Infections*. **8** (2019), pp. 516–530.

73. V. Borisevich, B. Lee, A. Hickey, B. DeBuysscher, C. C. Broder, H. Feldmann, B. Rockx, Escape From Monoclonal Antibody Neutralization Affects Henipavirus Fitness In Vitro and In Vivo. *J. Infect. Dis.* **213**, 448–455 (2016).

74. K. N. Bossart, G. Crameri, A. S. Dimitrov, B. A. Mungall, Y.-R. Feng, J. R. Patch, A. Choudhary, L.-F. Wang, B. T. Eaton, C. C. Broder, Receptor Binding, Fusion Inhibition, and Induction of Cross-Reactive Neutralizing Antibodies by a Soluble G Glycoprotein of *Hendra Virus*. *Journal of Virology*. **79** (2005), pp. 6690–6702.

75. D. Maar, B. Harmon, D. Chu, B. Schulz, H. C. Aguilar, B. Lee, O. A. Negrete, Cysteines in the Stalk of the Nipah Virus G Glycoprotein Are Located in a Distinct Subdomain Critical for Fusion Activation. *Journal of Virology*. **86** (2012), pp. 6632–6642.

76. B. D. Welch, P. Yuan, S. Bose, C. A. Kors, R. A. Lamb, T. S. Jardetzky, Structure of the parainfluenza virus 5 (PIV5) hemagglutinin-neuraminidase (HN) ectodomain (2013), , doi:10.2210/pdb4jf7/pdb.

77. P. Yuan, K. A. Swanson, G. P. Leser, R. G. Paterson, R. A. Lamb, T. S. Jardetzky, Structure of the Newcastle disease virus hemagglutinin-neuraminidase (HN) ectodomain reveals a four-helix bundle stalk. *Proceedings of the National Academy of Sciences*. **108** (2011), pp. 14920–14925.

78. M. P. Doyle, N. Kose, V. Borisevich, E. Binshtein, M. Amaya, M. Nagel, E. J. Annand, E. Armstrong, R. Bombardi, J. Dong, K. L. Schey, C. C. Broder, L. Zeitlin, E. A. Kuang, Z. A. Bornholdt, B. R. West, T. W. Geisbert, R. W. Cross, J. E. Crowe Jr, Cooperativity mediated by rationally selected combinations of human monoclonal antibodies targeting the henipavirus receptor binding protein. *Cell Rep.* **36**, 109628 (2021).

79. K. Xu, B. Rockx, Y. Xie, B. L. DeBuysscher, D. L. Fusco, Z. Zhu, Y.-P. Chan, Y. Xu, T. Luu, R. Z. Cer, H. Feldmann, V. Mokashi, D. S. Dimitrov, K. A. Bishop-Lilly, C. C. Broder, D. B. Nikolov, Crystal structure of the Hendra virus attachment G glycoprotein bound to a potent cross-reactive neutralizing human monoclonal antibody. *PLoS Pathog.* **9**, e1003684 (2013).

80. J. J. W. Wong, T. A. Young, J. Zhang, S. Liu, G. P. Leser, E. A. Komives, R. A. Lamb, Z. Hong Zhou, J. Salafsky, T. S. Jardetzky, Monomeric ephrinB2 binding induces allosteric

changes in Nipah virus G that precede its full activation. *Nature Communications*. **8** (2017), , doi:10.1038/s41467-017-00863-3.

81. A. Patel, D. B. Weiner, It Takes a Matured mAb to Treat Ebolavirus Infection. *Cell Host & Microbe*. **25** (2019), pp. 10–12.

82. A. Baum, B. O. Fulton, E. Wloga, R. Copin, K. E. Pascal, V. Russo, S. Giordano, K. Lanza, N. Negron, M. Ni, Y. Wei, G. S. Atwal, A. J. Murphy, N. Stahl, G. D. Yancopoulos, C. A. Kyratsous, Antibody cocktail to SARS-CoV-2 spike protein prevents rapid mutational escape seen with individual antibodies. *Science*. **369**, 1014–1018 (2020).

83. J. Hansen, A. Baum, K. E. Pascal, V. Russo, S. Giordano, E. Wloga, B. O. Fulton, Y. Yan, K. Koon, K. Patel, K. M. Chung, A. Hermann, E. Ullman, J. Cruz, A. Rafique, T. Huang, J. Fairhurst, C. Libertiny, M. Malbec, W.-Y. Lee, R. Welsh, G. Farr, S. Pennington, D. Deshpande, J. Cheng, A. Watty, P. Bouffard, R. Babb, N. Levenkova, C. Chen, B. Zhang, A. R. Hernandez, K. Saotome, Y. Zhou, M. Franklin, S. Sivapalasingam, D. C. Lye, S. Weston, J. Logue, R. Haupt, M. Frieman, G. Chen, W. Olson, A. J. Murphy, N. Stahl, G. D. Yancopoulos, C. A. Kyratsous, Studies in humanized mice and convalescent humans yield a SARS-CoV-2 antibody cocktail. *Science*. **369** (2020), pp. 1010–1014.

84. Z. Zhu, A. S. Dimitrov, K. N. Bossart, G. Crameri, K. A. Bishop, V. Choudhry, B. A. Mungall, Y.-R. Feng, A. Choudhary, M.-Y. Zhang, Y. Feng, L.-F. Wang, X. Xiao, B. T. Eaton, C. C. Broder, D. S. Dimitrov, Potent neutralization of Hendra and Nipah viruses by human monoclonal antibodies. *J. Virol.* **80**, 891–899 (2006).

85. J. Dong, R. W. Cross, M. P. Doyle, N. Kose, J. J. Mousa, E. J. Annand, V. Borisevich, K. N. Agans, R. Sutton, R. Nargi, M. Majedi, K. A. Fenton, W. Reichard, R. G. Bombardi, T. W. Geisbert, J. E. Crowe Jr, Potent Henipavirus Neutralization by Antibodies Recognizing Diverse Sites on Hendra and Nipah Virus Receptor Binding Protein. *Cell*. **183**, 1536–1550.e17 (2020).

86. M. Bianchi, H. L. Turner, B. Nogal, C. A. Cottrell, D. Oyen, M. Pauthner, R. Bastidas, R. Nedellec, L. E. McCoy, I. A. Wilson, D. R. Burton, A. B. Ward, L. Hangartner, Electron-Microscopy-Based Epitope Mapping Defines Specificities of Polyclonal Antibodies Elicited during HIV-1 BG505 Envelope Trimer Immunization. *Immunity*. **49** (2018), pp. 288–300.e8.

87. S. Boyoglu-Barnum, D. Ellis, R. A. Gillespie, G. B. Hutchinson, Y.-J. Park, S. M. Moin, O. J. Acton, R. Ravichandran, M. Murphy, D. Pettie, N. Matheson, L. Carter, A. Creanga, M. J. Watson, S. Kephart, S. Ataca, J. R. Vaile, G. Ueda, M. C. Crank, L. Stewart, K. K. Lee, M. Guttman, D. Baker, J. R. Mascola, D. Veesler, B. S. Graham, N. P. King, M. Kanekiyo, Quadrivalent influenza nanoparticle vaccines induce broad protection. *Nature*. **592** (2021), pp. 623–628.

88. C. O. Barnes, A. P. West Jr, K. E. Huey-Tubman, M. A. G. Hoffmann, N. G. Sharaf, P. R. Hoffman, N. Koranda, H. B. Gristick, C. Gaebler, F. Muecksch, J. C. C. Lorenzi, S. Finkin, T. Hägglöf, A. Hurley, K. G. Millard, Y. Weisblum, F. Schmidt, T. Hatziioannou, P. D. Bieniasz, M. Caskey, D. F. Robbiani, M. C. Nussenzweig, P. J. Bjorkman, Structures of Human Antibodies Bound to SARS-CoV-2 Spike Reveal Common Epitopes and Recurrent Features of Antibodies. *Cell*. **182**, 828–842.e16 (2020).

89. J. S. McLellan, M. Chen, M. G. Joyce, M. Sastry, G. B. E. Stewart-Jones, Y. Yang, B.

Zhang, L. Chen, S. Srivatsan, A. Zheng, T. Zhou, K. W. Graepel, A. Kumar, S. Moin, J. C. Boyington, G.-Y. Chuang, C. Soto, U. Baxa, A. Q. Bakker, H. Spits, T. Beaumont, Z. Zheng, N. Xia, S.-Y. Ko, J.-P. Todd, S. Rao, B. S. Graham, P. D. Kwong, Structure-based design of a fusion glycoprotein vaccine for respiratory syncytial virus. *Science*. **342**, 592–598 (2013).

90. J. Marcandalli, B. Fiala, S. Ols, M. Perotti, W. de van der Schueren, J. Snijder, E. Hodge, M. Benhaim, R. Ravichandran, L. Carter, W. Sheffler, L. Brunner, M. Lawrenz, P. Dubois, A. Lanzavecchia, F. Sallusto, K. K. Lee, D. Veesler, C. E. Correnti, L. J. Stewart, D. Baker, K. Loré, L. Perez, N. P. King, Induction of Potent Neutralizing Antibody Responses by a Designed Protein Nanoparticle Vaccine for Respiratory Syncytial Virus. *Cell*. **176** (2019), pp. 1420–1431.e17.

91. C.-L. Hsieh, J. A. Goldsmith, J. M. Schaub, A. M. DiVenere, H.-C. Kuo, K. Javanmardi, K. C. Le, D. Wrapp, A. G. Lee, Y. Liu, C.-W. Chou, P. O. Byrne, C. K. Hjorth, N. V. Johnson, J. Ludes-Meyers, A. W. Nguyen, J. Park, N. Wang, D. Amengor, J. J. Lavinder, G. C. Ippolito, J. A. Maynard, I. J. Finkelstein, J. S. McLellan, Structure-based design of prefusion-stabilized SARS-CoV-2 spikes. *Science*. **369**, 1501–1505 (2020).

92. P. S. Arunachalam, A. C. Walls, N. Golden, C. Atyeo, S. Fischinger, C. Li, P. Aye, M. J. Navarro, L. Lai, V. V. Edara, K. Röltgen, K. Rogers, L. Shirreff, D. E. Ferrell, S. Wrenn, D. Pettie, J. C. Kraft, M. C. Miranda, E. Kepl, C. Sydeman, N. Brunette, M. Murphy, B. Fiala, L. Carter, A. G. White, M. Trisal, C.-L. Hsieh, K. Russell-Lodrigue, C. Monjure, J. Dufour, S. Spencer, L. Doyle-Meyers, R. P. Bohm, N. J. Maness, C. Roy, J. A. Plante, K. S. Plante, A. Zhu, M. J. Gorman, S. Shin, X. Shen, J. Fontenot, S. Gupta, D. T. O'Hagan, R. Van Der Most, R. Rappuoli, R. L. Coffman, D. Novack, J. S. McLellan, S. Subramaniam, D. Montefiori, S. D. Boyd, J. L. Flynn, G. Alter, F. Villinger, H. Kleanthous, J. Rappaport, M. S. Suthar, N. P. King, D. Veesler, B. Pulendran, Adjuvanting a subunit COVID-19 vaccine to induce protective immunity. *Nature*. **594**, 253–258 (2021).

93. D. Wrapp, N. Wang, K. S. Corbett, J. A. Goldsmith, C.-L. Hsieh, O. Abiona, B. S. Graham, J. S. McLellan, Cryo-EM structure of the 2019-nCoV spike in the prefusion conformation. *Science*. **367**, 1260–1263 (2020).

94. M. McCallum, A. C. Walls, J. E. Bowen, D. Corti, D. Veesler, Structure-guided covalent stabilization of coronavirus spike glycoprotein trimers in the closed conformation. *Nat. Struct. Mol. Biol.* **27**, 942–949 (2020).

95. K. S. Corbett, D. K. Edwards, S. R. Leist, O. M. Abiona, S. Boyoglu-Barnum, R. A. Gillespie, S. Himansu, A. Schäfer, C. T. Ziwawo, A. T. DiPiazza, K. H. Dinnon, S. M. Elbashir, C. A. Shaw, A. Woods, E. J. Fritch, D. R. Martinez, K. W. Bock, M. Minai, B. M. Nagata, G. B. Hutchinson, K. Wu, C. Henry, K. Bahl, D. Garcia-Dominguez, L. Ma, I. Renzi, W.-P. Kong, S. D. Schmidt, L. Wang, Y. Zhang, E. Phung, L. A. Chang, R. J. Loomis, N. E. Altaras, E. Narayanan, M. Metkar, V. Presnyak, C. Liu, M. K. Louder, W. Shi, K. Leung, E. S. Yang, A. West, K. L. Gully, L. J. Stevens, N. Wang, D. Wrapp, N. A. Doria-Rose, G. Stewart-Jones, H. Bennett, G. S. Alvarado, M. C. Nason, T. J. Ruckwardt, J. S. McLellan, M. R. Denison, J. D. Chappell, I. N. Moore, K. M. Morabito, J. R. Mascola, R. S. Baric, A. Carfi, B. S. Graham, SARS-CoV-2 mRNA vaccine design enabled by prototype pathogen preparedness. *Nature*. **586**, 567–571 (2020).

96. A. C. Walls, B. Fiala, A. Schäfer, S. Wrenn, M. N. Pham, M. Murphy, L. V. Tse, L. Shehata, M. A. O'Connor, C. Chen, M. J. Navarro, M. C. Miranda, D. Pettie, R. Ravichandran, J. C. Kraft, C. Ogohara, A. Palser, S. Chalk, E.-C. Lee, K. Guerriero, E. Kepl, C. M. Chow, C.

Sydeman, E. A. Hodge, B. Brown, J. T. Fuller, K. H. Dinnon 3rd, L. E. Gralinski, S. R. Leist, K. L. Gully, T. B. Lewis, M. Guttman, H. Y. Chu, K. K. Lee, D. H. Fuller, R. S. Baric, P. Kellam, L. Carter, M. Pepper, T. P. Sheahan, D. Veesler, N. P. King, Elicitation of Potent Neutralizing Antibody Responses by Designed Protein Nanoparticle Vaccines for SARS-CoV-2. *Cell*. **183**, 1367–1382.e17 (2020).

97. A. C. Walls, M. C. Miranda, M. N. Pham, A. Schäfer, A. Greaney, P. S. Arunachalam, M.-J. Navarro, M. Alejandra Tortorici, K. Rogers, M. A. O'Connor, L. Shireff, D. E. Ferrell, N. Brunette, E. Kepl, J. Bowen, S. K. Zepeda, T. Starr, C.-L. Hsieh, B. Fiala, S. Wrenn, D. Pettie, C. Sydeman, M. Johnson, A. Blackstone, R. Ravichandran, C. Ogohara, L. Carter, S. W. Tilles, R. Rappuoli, D. T. O'Hagan, R. Van Der Most, W. C. Van Voorhis, J. S. McLellan, H. Kleanthous, T. P. Sheahan, D. H. Fuller, F. Villinger, J. Bloom, B. Pulendran, R. Baric, N. King, D. Veesler, Elicitation of broadly protective sarbecovirus immunity by receptor-binding domain nanoparticle vaccines, , doi:10.1101/2021.03.15.435528.

98. A. A. Cohen, P. N. P. Gnanapragasam, Y. E. Lee, P. R. Hoffman, S. Ou, L. M. Kakutani, J. R. Keeffe, H.-J. Wu, M. Howarth, A. P. West, C. O. Barnes, M. C. Nussenzweig, P. J. Bjorkman, Mosaic nanoparticles elicit cross-reactive immune responses to zoonotic coronaviruses in mice, , doi:10.1101/2020.11.17.387092.

99. M. Kanekiyo, M. Gordon Joyce, R. A. Gillespie, J. R. Gallagher, S. F. Andrews, H. M. Yassine, A. K. Wheatley, B. E. Fisher, D. R. Ambrozak, A. Creanga, K. Leung, E. S. Yang, S. Boyoglu-Barnum, I. S. Georgiev, Y. Tsybovsky, M. S. Prabhakaran, H. Andersen, W.-P. Kong, U. Baxa, K. L. Zephir, J. E. Ledgerwood, R. A. Koup, P. D. Kwong, A. K. Harris, A. B. McDermott, J. R. Mascola, B. S. Graham, Mosaic nanoparticle display of diverse influenza virus hemagglutinins elicits broad B cell responses. *Nature Immunology*. **20** (2019), pp. 362–372.

100. J. Wang, D. E. Anderson, K. Halpin, X. Hong, H. Chen, S. Walker, S. Valdeter, B. van der Heide, M. J. Neave, J. Bingham, D. O'Brien, D. Eagles, L.-F. Wang, D. T. Williams, A New Hendra Virus Genotype Found in Australian Flying Foxes, , doi:10.21203/rs.3.rs-616496/v1.

101. E. J. Annand, B. A. Horsburgh, K. Xu, P. A. Reid, B. Poole, M. C. de Kantzow, N. Brown, A. Tweedie, M. Michie, J. D. Grewar, A. E. Jackson, N. B. Singanallur, K. M. Plain, K. Kim, M. Tachedjian, B. van der Heide, S. Crameri, D. T. Williams, C. Secombe, E. D. Laing, S. Sterling, L. Yan, L. Jackson, C. Jones, R. K. Plowright, A. J. Peel, A. C. Breed, I. Diallo, N. K. Dhand, P. N. Britton, C. C. Broder, I. Smith, J.-S. Eden, Novel Hendra Virus Variant Detected by Sentinel Surveillance of Horses in Australia. *Emerging Infectious Diseases*. **28** (2022), pp. 693–704.

102. M. I. Bonaparte, A. S. Dimitrov, K. N. Bossart, G. Crameri, B. A. Mungall, K. A. Bishop, V. Choudhry, D. S. Dimitrov, L.-F. Wang, B. T. Eaton, C. C. Broder, Ephrin-B2 ligand is a functional receptor for Hendra virus and Nipah virus. *Proc. Natl. Acad. Sci. U. S. A.* **102**, 10652–10657 (2005).

103. E. D. Laing, M. Amaya, C. K. Navaratnarajah, Y.-R. Feng, R. Cattaneo, L.-F. Wang, C. C. Broder, Rescue and characterization of recombinant cedar virus, a non-pathogenic Henipavirus species. *Virol. J.* **15**, 56 (2018).

104. K. N. Bossart, M. Tachedjian, J. A. McEachern, G. Crameri, Z. Zhu, D. S. Dimitrov, C. C. Broder, L.-F. Wang, Functional studies of host-specific ephrin-B ligands as Henipavirus receptors. *Virology*. **372**, 357–371 (2008).

105. G. A. Marsh, C. de Jong, J. A. Barr, M. Tachedjian, C. Smith, D. Middleton, M. Yu, S. Todd, A. J. Foord, V. Haring, J. Payne, R. Robinson, I. Broz, G. Crameri, H. E. Field, L.-F. Wang, Cedar virus: a novel Henipavirus isolated from Australian bats. *PLoS Pathog.* **8**, e1002836 (2012).

106. K. N. Bossart, Z. Zhu, D. Middleton, J. Klippel, G. Crameri, J. Bingham, J. A. McEachern, D. Green, T. J. Hancock, Y.-P. Chan, A. C. Hickey, D. S. Dimitrov, L.-F. Wang, C. C. Broder, A neutralizing human monoclonal antibody protects against lethal disease in a new ferret model of acute nipah virus infection. *PLoS Pathog.* **5**, e1000642 (2009).

107. T. W. Geisbert, C. E. Mire, J. B. Geisbert, Y.-P. Chan, K. N. Agans, F. Feldmann, K. A. Fenton, Z. Zhu, D. S. Dimitrov, D. P. Scott, K. N. Bossart, H. Feldmann, C. C. Broder, Therapeutic Treatment of Nipah Virus Infection in Nonhuman Primates with a Neutralizing Human Monoclonal Antibody. *Science Translational Medicine*. **6** (2014), , doi:10.1126/scitranslmed.3008929.

108. K. Xu, K. R. Rajashankar, Y.-P. Chan, J. P. Himanen, C. C. Broder, D. B. Nikolov, Host cell recognition by the henipaviruses: Crystal structures of the Nipah G attachment glycoprotein and its complex with ephrin-B3. *Proceedings of the National Academy of Sciences*. **105** (2008), pp. 9953–9958.

109. T. A. Bowden, A. R. Aricescu, R. J. C. Gilbert, J. M. Grimes, E. Y. Jones, D. I. Stuart, Structural basis of Nipah and Hendra virus attachment to their cell-surface receptor ephrin-B2. *Nat. Struct. Mol. Biol.* **15**, 567–572 (2008).

110. B. Moss, Poxviridae : the viruses and thier replication. *Fields virology*, 2637–2671 (1996).

111. S. Cudmore, R. Blasco, R. Vincentelli, M. Esteban, B. Sodeik, G. Griffiths, J. Krijnse Locker, A vaccinia virus core protein, p39, is membrane associated. *J. Virol.* **70**, 6909–6921 (1996).

112. K. Essani, S. Dales, Biogenesis of vaccinia: evidence for more than 100 polypeptides in the virion. *Virology*. **95**, 385–394 (1979).

113. S. Dales, L. Siminovitch, The development of vaccinia virus in Earle's L strain cells as examined by electron microscopy. *J. Biophys. Biochem. Cytol.* **10**, 475–503 (1961).

114. S. Dales, E. H. Mosbach, Vaccinia as a model for membrane biogenesis. *Virology*. **35**, 564–583 (1968).

115. S. Dales, B. G. T. Pogo, *Biology of Poxviruses* (Springer Science & Business Media, 2013).

116. Y. Ichihashi, S. Matsumoto, S. Dales, Biogenesis of poxviruses: role of A-type inclusions and host cell membranes in virus dissemination. *Virology*. **46**, 507–532 (1971).

117. C. Morgan, The insertion of DNA into vaccinia virus. *Science*. **193**, 591–592 (1976).

118. C. Morgan, Vaccinia virus reexamined: development and release. *Virology*. **73**, 43–58 (1976).

119. M. Schmelz, B. Sodeik, M. Ericsson, E. J. Wolffe, H. Shida, G. Hiller, G. Griffiths,

Assembly of vaccinia virus: the second wrapping cisterna is derived from the trans Golgi network. *J. Virol.* **68**, 130–147 (1994).

120. D. M. Jesus, N. Moussatche, B. B. D. McFadden, C. P. Nielsen, S. M. D'Costa, R. C. Condit, Vaccinia virus protein A3 is required for the production of normal immature virions and for the encapsidation of the nucleocapsid protein L4. *Virology*. **481**, 1–12 (2015).

121. N. Moussatche, R. C. Condit, Fine structure of the vaccinia virion determined by controlled degradation and immunolocalization. *Virology*. **475**, 204–218 (2015).

122. Y. Ichihashi, M. Oie, T. Tsuruhara, Location of DNA-binding proteins and disulfide-linked proteins in vaccinia virus structural elements. *J. Virol.* **50**, 929–938 (1984).

123. N. Roos, M. Cyrklaff, S. Cudmore, R. Blasco, J. Krijnse-Locker, G. Griffiths, A novel immunogold cryoelectron microscopic approach to investigate the structure of the intracellular and extracellular forms of vaccinia virus. *EMBO J.* **15**, 2343–2355 (1996).

124. K. Pedersen, E. J. Snijder, S. Schleich, N. Roos, G. Griffiths, J. K. Locker, Characterization of vaccinia virus intracellular cores: implications for viral uncoating and core structure. *J. Virol.* **74**, 3525–3536 (2000).

125. S. Wilton, A. R. Mohandas, S. Dales, Organization of the vaccinia envelope and relationship to the structure of intracellular mature virions. *Virology*. **214**, 503–511 (1995).

126. M. Hernandez-Gonzalez, T. Calcraft, A. Nans, P. B. Rosenthal, M. Way, Cryo-ET of infected cells reveals that a succession of two lattices drives vaccinia virus assembly. *bioRxiv* (2022), p. 2022.08.11.503617.

127. K. B. Chua, W. J. Bellini, P. A. Rota, B. H. Harcourt, A. Tamin, S. K. Lam, T. G. Ksiazek, P. E. Rollin, S. R. Zaki, W. Shieh, C. S. Goldsmith, D. J. Gubler, J. T. Roehrig, B. Eaton, A. R. Gould, J. Olson, H. Field, P. Daniels, A. E. Ling, C. J. Peters, L. J. Anderson, B. W. Mahy, Nipah virus: a recently emergent deadly paramyxovirus. *Science*. **288**, 1432–1435 (2000).

128. M. Amaya, H. Cheng, V. Borisevich, C. K. Navaratnarajah, R. Cattaneo, L. Cooper, T. W. Moore, I. N. Gaisina, T. W. Geisbert, L. Rong, C. C. Broder, A recombinant Cedar virus based high-throughput screening assay for henipavirus antiviral discovery. *Antiviral Res.* **193**, 105084 (2021).

129. G. Kiss, J. M. Holl, G. M. Williams, E. Alonas, D. Vanover, A. W. Lifland, M. Gudheti, R. C. Guerrero-Ferreira, V. Nair, H. Yi, B. S. Graham, P. J. Santangelo, E. R. Wright, Structural analysis of respiratory syncytial virus reveals the position of M2-1 between the matrix protein and the ribonucleoprotein complex. *J. Virol.* **88**, 7602–7617 (2014).

130. D. S. Ker, H. T. Jenkins, S. J. Greive, A. A. Antson, CryoEM structure of the Nipah virus nucleocapsid single helical turn assembly (2021), , doi:10.2210/pdb7nt5/pdb.

131. M. McCallum, A. De Marco, F. A. Lempp, M. A. Tortorici, D. Pinto, A. C. Walls, M. Beltramello, A. Chen, Z. Liu, F. Zatta, S. Zepeda, J. di Iulio, J. E. Bowen, M. Montiel-Ruiz, J. Zhou, L. E. Rosen, S. Bianchi, B. Guarino, C. S. Fregni, R. Abdelnabi, S.-Y. C. Foo, P. W. Rothlauf, L.-M. Bloyet, F. Benigni, E. Cameroni, J. Neyts, A. Riva, G. Snell, A. Telenti, S. P. J. Whelan, H. W. Virgin, D. Corti, M. S. Pizzuto, D. Veesler, N-terminal domain antigenic

mapping reveals a site of vulnerability for SARS-CoV-2. *Cell*. **184**, 2332–2347.e16 (2021).